THE CALCULATION OF THEORETICAL CHROMOSPHERIC MODELS AND THE INTERPRETATION OF SOLAR SPECTRA FROM ROCKETS AND SPACECRAFT

NASA Grant NSG-7054

Semiannual Report No. 18 and 19

For the period 1 January 1984 to 30 June 1984
and the period 1 July 1984 to 31 December 1984

Principal Investigator
Eugene H. Avrett

January 1985

Prepared for
National Aeronautics and Space Administration
Washington, D.C. 20546

Smithsonian Institution
Astrophysical Observatory
Cambridge, Massachusetts 02138

The Smithsonian Astrophysical Observatory
is a member of the
Harvard-Smithsonian Center for Astrophysics

The NASA Technical Officer for this grant is Dr. J. David Bohlin, Code EZ-7, Headquarters, National Aeronautics and Space Administration, Washington, D.C. 20546.

THE CALCULATION OF THEORETICAL CHROMOSPHERIC MODELS AND THE INTERPRETATION OF SOLAR SPECTRA FROM ROCKETS AND SPACECRAFT

NASA Grant NSG-7054

Semiannual Report No. 18 and 19

For the period 1 January 1984 to 30 June 1984
and the period 1 July 1984 to 31 December 1984

Principal Investigator
Eugene H. Avrett

January 1985

Prepared for
National Aeronautics and Space Administration
Washington, D.C. 20546

Smithsonian Institution
Astrophysical Observatory
Cambridge, Massachusetts 02138

The Smithsonian Astrophysical Observatory
is a member of the
Harvard-Smithsonian Center for Astrophysics

The NASA Technical Officer for this grant is Dr. J. David Bohlin, Code EZ-7, Headquarters, National Aeronautics and Space Administration, Washington, D.C. 20546.

THE CALCULATION OF
THEORETICAL CHROMOSPHERIC MODELS AND
THE INTERPRETATION OF
SOLAR SPECTRA FROM ROCKETS AND SPACECRAFT

NASA Grant NSG-7054
Semiannual Report No. 18 and No. 19

Our most significant advance in 1984 was the computation of improved versions of the multi-component VAL solar models that include opacities for 17 million atomic and molecular lines computed by Kurucz the year before. These models now produce a consistant match to observations in the ultraviolet and far infrared and to the Ca H and K lines. A short paper was presented at the AAS meeting in Baltimore by Avrett, Kurucz, and Loeser, "New models of the solar temperature minimum and low chromosphere" (Bull. Amer. Astron. Soc., 16, 450, 1984), and Avrett gave a review talk at the "Chromospheric Diagnostics and Modeling Workshop" at Sac Peak in August. A copy of that paper is attached as the description of the new models for this report. We are preparing a large paper for the Astrophysical Journal.

This year we have continued to work on models and spectra of sunspots in collaboration with Per Maltby and Olav Kjeldseth Moe of the Institute for Theoretical Astrophysics in Oslo. Kjeldseth Moe is analyzing the sunspot observations in the ultraviolet region 140-168 nm obtained by the NRL High Resolution Telescope and Spectrograph, while Maltby has made extensive photometric observations of sunspot umbrae and penumbrae in 10 channels covering the wavelength region 387-3800 nm. Maltby visited Cambridge in August to work on the models. We are just completing a paper, "A new sunspot umbral model and its variation with the solar cycle" by Maltby, Avrett, Carlsson, Kjeldseth-Moe, Kurucz, and Loeser. We are continuing to work on detailed calculation of the spectrum and comparison with observations. The Oslo group is also reducing HRTS data for other solar features and they will make those data available to us.

Kurucz spent July through December at Los Alamos and was allowed to use substantial amounts of time on their Crays, CDC 7600s, and VAXes in a collaborative arrangement for computing atomic and molecular opacities for cool stars and the earth's atmosphere and for doing atmospheric modelling. The sun is the first test case, both to check the opacity calculations against the observed solar spectrum, which for ground-based spectra includes the terrestrial line absorption, and to check the purely theoretical model calculation against the observed solar energy distribution. We hope these arrangements will continue through 1985, but we cannot plan into the future because Los Alamos computers are becoming more saturated. Kurucz has not been been able to get access to large computers at any other laboratory. It would be very helpful if there were some way that NASA could provide us with computer time, perhaps at Ames.

Last year we discovered that the 1972 Kurucz-Peytremann atomic line data were not able to account for the solar ultraviolet opacity because of missing excited configurations of iron group elements.

Generally, laboratory analyses of atomic spectra are not sufficiently complete to predict all the lines that can be significant in the solar spectrum or in computing opacity. In fact, such analyses are often quite inadequate. In order to predict configurations that have not been observed, or that have been only partially observed, and to estimate the configuration interaction among those configurations and the known configurations, it is necessary to make a theoretical calculation. During Kurucz's visits to Los Alamos he has used Robert Cowan's Hartree-Fock program to build up a library of predicted Slater and transition integrals for 50 low configurations of the first 10 ionization stages of the elements up through zinc, and of the first 5 ionization stages for all the heavier elements. During 1984 Kurucz used these data in making new calculations for the atomic lines, but the work has been very difficult and has gone much more slowly than anticipated; Fe II is finished, Fe I is almost complete, Cr I and II and Ni I and II are still in the least squares fitting phase. Other less abundant elements have not yet been started but they should play only a secondary role in the opacity, in any case, and will be easier to compute because most of them have simpler spectra. We can give some idea of the complexity by citing the statistics for Fe II:

	even	odd
number of configurations	22	16
number of levels	5723	5198
largest Hamiltonian matrix	1102	1049
number of least squares parameters (many fixed at Hartree-Fock)	729	541
total number of lines saved	1,112,322	

Each least-squares iteration took a significant amount of time on a Cray and many iterations were required. In these calculations radiative, Stark, and van der Waals damping constants and Lande g values are automatically produced for each line. As soon as Fe I is completed we plan to compute sample spectra using both the old and new Fe line lists to show the improvement in the ultraviolet wavelength regions that are most discrepant with observation.

We made very little progress on molecules in 1984 because of the time needed to complete the atomic calculations. We obtained Brault's FTS CN spectra but have not yet reduced them. They will provide a tremendous advance in our knowledge of CN and should account for many weak features in the solar spectrum. We got the Air Force atmospheric line list working. There are many weak atmospheric lines that are clearly present in our high quality solar spectra but that are not in the line list. We are also trying to get all the old Los Alamos molecular line data into shape for use in our opacity calculations.

We also did the following work in 1984.

Peter Ulmschneider asked Kurucz to produce CO infrared opacities for use in acoustic wave chromospheric heating calculations. We have computed the absorption coefficient spectra per CO molecule for a range of temperatures and pressures and from these we can produce any sort of mean or distribution function opacity required.

Kurucz, Furenlid, Brault, and Testerman have produced a high-resolution, high-signal-to-noise FTS solar flux atlas for the wavelength range 296 to 1300 nm. The atlas is plotted as pseudo-residual flux, and a table is given with conversion factors to the Neckel and Labs (Solar Physics, 74, 231-249, 1981) absolute calibration. The atlas is being published with help from the National Solar Observatory and is being sold to recover the cost of printing. A few introductory pages from the atlas are attached, but we are able to send only one complete bindery sample to NASA headquarters at this time. This atlas has been invaluable in testing our line data.

Larry Petro, Warren Rosen, and Peter Foukal have been searching for solar limb-darkening variations that presumably would reflect changes in the structure of the solar atmosphere from changes in convective efficiency (Petro, Foukal, Rosen, Kurucz, and Pierce, Ap.J., 283, 426-438, 1984). Kurucz computes the theoretical derivatives for such variations for various treatments of convection. Unfortunately our old models do not reproduce the solar limb-darkening and do not include the molecular opacity that would be the most sensitive component to the variation. Our new model does have the molecules but it still does not predict the correct limb-darkening. We hope that our next try with the improved atomic opacity will finally do the job.

RECENT THERMAL MODELS OF THE CHROMOSPHERE

Eugene H. Avrett

Harvard-Smithsonian Center for Astrophysics
Cambridge, MA 02138

ABSTRACT

This paper describes recent research on the calculation of solar chromospheric models. The models included here are based on the observed spectrum, and on the assumption of hydrostatic equilibrium. The calculations depend on realistic solutions of the radiative transfer and statistical equilibrium equations for optically thick lines and continua, and on including the effects of large numbers of lines throughout the spectrum. Although spectroheliograms show that the structure of the chromosphere is highly complex, one-dimensional models of particular features are reasonably successful in matching observed spectra. There has been considerable recent progress in applying such models to the interpretation of chromospheric observations.

This paper is organized as follows:

I. The Ca II Resonance Lines
II. The 40-140 nm Continuum
III. Model Calculations
IV. The Temperature Minimum Region
V. Energy Balance
VI. Questions and Problems

The final section lists a number of unanswered questions and unsolved problems that need further study.

I. The Ca II Resonance Lines

In the visible part of the solar spectrum a few prominent lines, such as the resonance lines of Ca II, have such a high opacity near their central wavelengths that the line cores are formed at chromospheric heights where the temperature increases in the outward direction. As a consequence, these lines show emission near their central wavelengths. Figure 1 shows the observed flux profile of the Ca II K and H lines centered at 393.37 nm and 396.85 nm, respectively. Two emission peaks close to each central wavelength are barely discernible in these plots of the entire line profiles. The central portion of the K line is shown on an enlarged scale in Figure 2, from White and Livingston (1981).

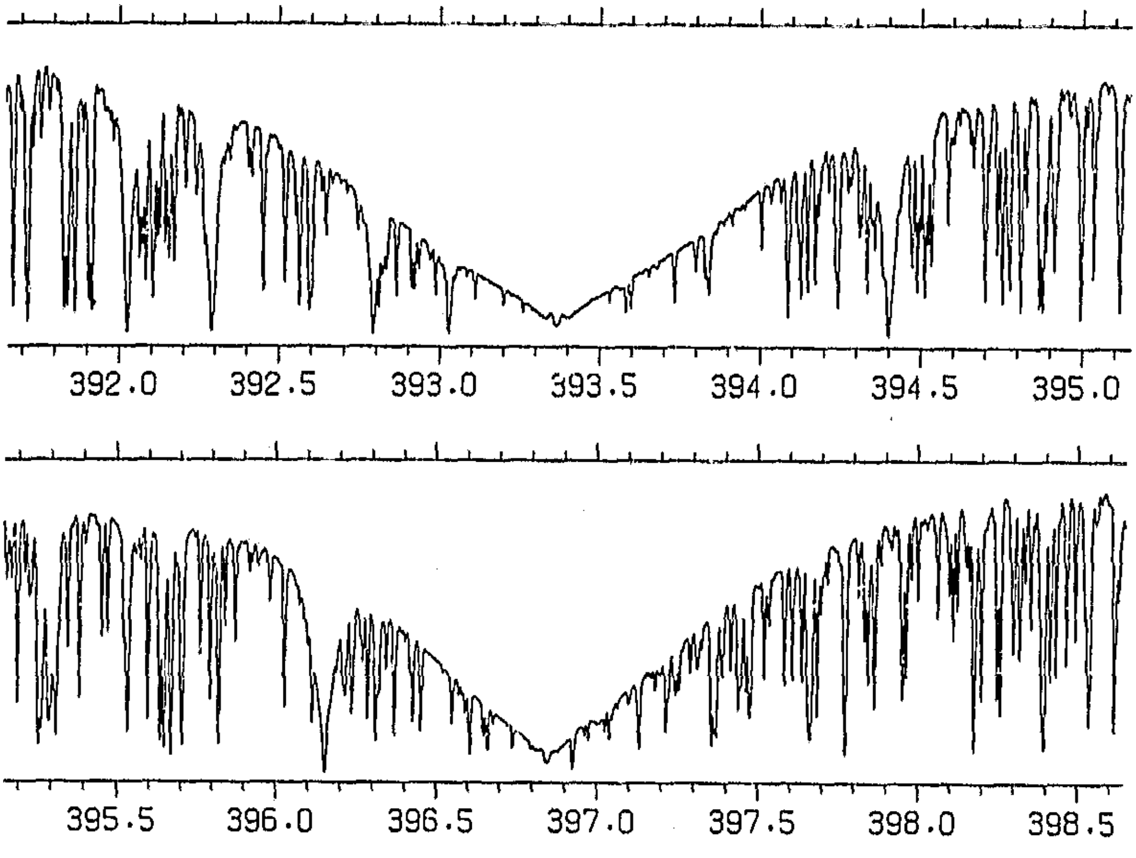

Fig. 1. — Ca II K and H flux profiles, obtained with the Kitt Peak Fourier Transform Spectrograph (Kurucz *et al.* 1984). The flux is plotted (vs. wavelength in nm) on a linear scale between zero and a pseudo-continuum level fitted to the observed flux maxima at 378 and 402 nm.

The lower profile in Figure 2 corresponds to the quiet-Sun intensity at disk center, rather than to the flux from the entire disk. The intensity profile from a bright plage region also appears for comparison.

Solar plages are much brighter than the quiet Sun, but quiet areas have brightness variations as well. Figure 3 shows the distribution of intensity profiles of the Ca II H line observed by Cram and Damé (1983). Ten profiles are plotted; the lowest corresponds to the faintest 10% and the highest to the brightest 10% of the observed quiet region.

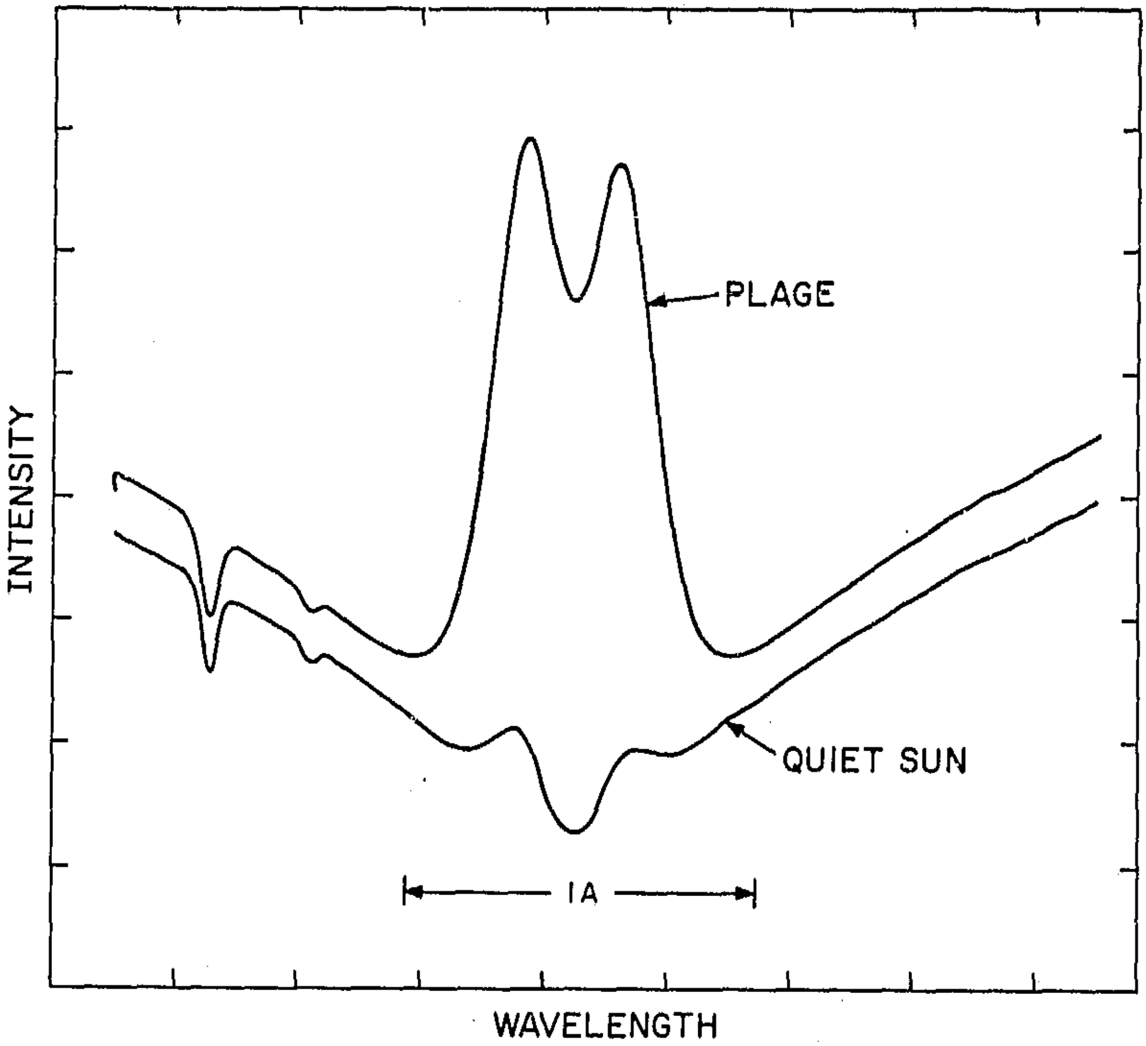

Fig. 2. — The Ca II K intensity profile near the line center, from the quiet Sun and from plage regions (White and Livingston 1981).

These results are given in residual intensity units, specifically, the intensity relative to the local continuum level, defined by White and Suemoto (1968) as a smooth curve passing through the estimated continuum values in the far wings of the H and K lines. Pasachoff (1971) studied the relationship between these residual units and the measured absolute intensities, and concluded that the White and Suemoto continuum intensity is $(4.5\pm0.1) \times 10^6$ ergs $\mathrm{cm}^{-2}\ \mathrm{s}^{-1}\ \mathrm{sr}^{-1}\ \mathrm{\AA}^{-1}$. This value is used to convert the residual intensity scale in Figure 3 to absolute units.

In order to compare with symmetric profiles from static atmosphere calculations, the red and violet halves of the line within ±0.7Å of the line center have been averaged (without including the absorption feature at $\Delta\lambda = 0.65$Å, $\lambda = 396.80$ nm, in the violet wing). Figure 4 shows the highest, the median, and the lowest profiles from Figure 3, averaged in this way, on an absolute intensity scale. The corresponding brightness temperatures are shown on the right side of Figure 4.

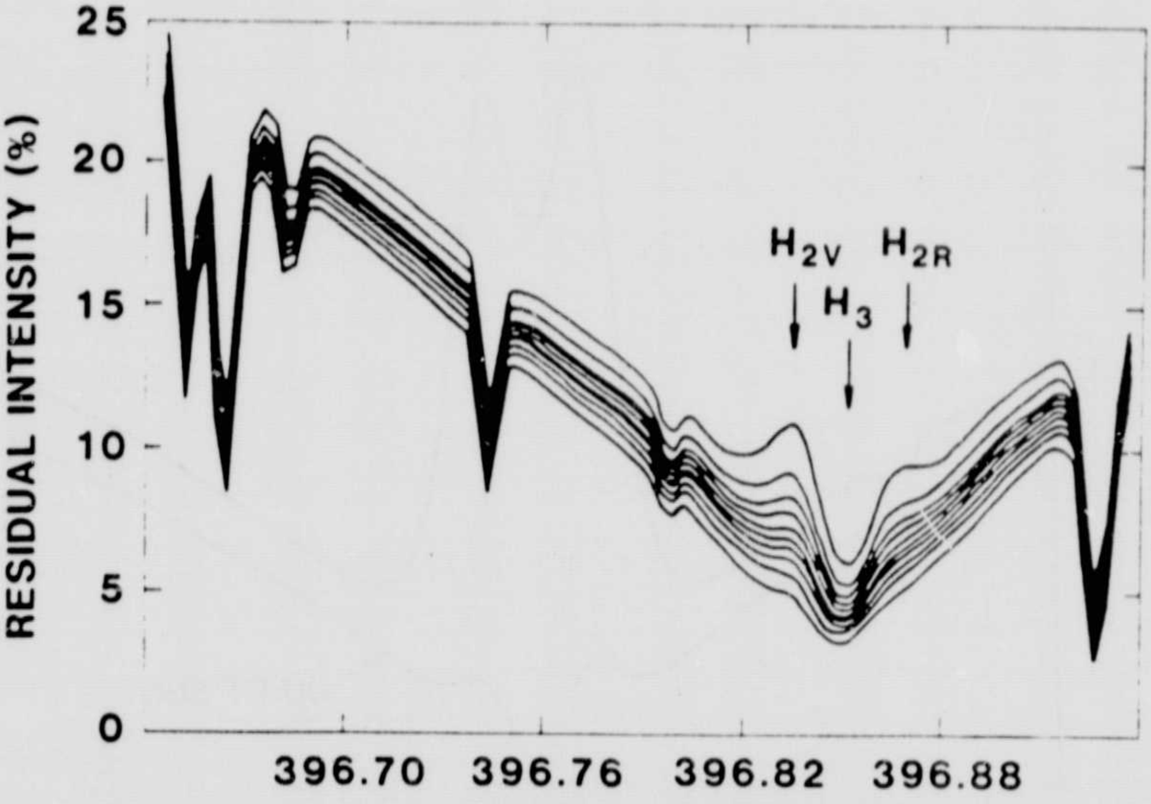

Fig. 3. — Quiet-Sun H-line profiles observed with high spatial resolution, grouped in 10 equal-area bins, from the sequence of profiles ordered according to brightness.

The intensity as a function of $\Delta\lambda$ in the line wing beyond the H_2 emission peak (at $\Delta\lambda \sim 0.16$Å) provides direct information about the temperature as a function of optical or geometrical depth, since the intensity successively further from the line center is formed at successively greater depths. The H_1 intensity minimum is formed at the temperature minimum in the atmosphere; the intensity rises between H_1 and H_2 (at least in the brighter components) because of the temperature rise in the low chromosphere. The central reversal occurs because the line center is formed high in the chromosphere where the electron density is too small to maintain local thermodynamic equilibrium (LTE), and photon scattering causes the line-center excitation temperature to be much smaller than the local kinetic temperature.

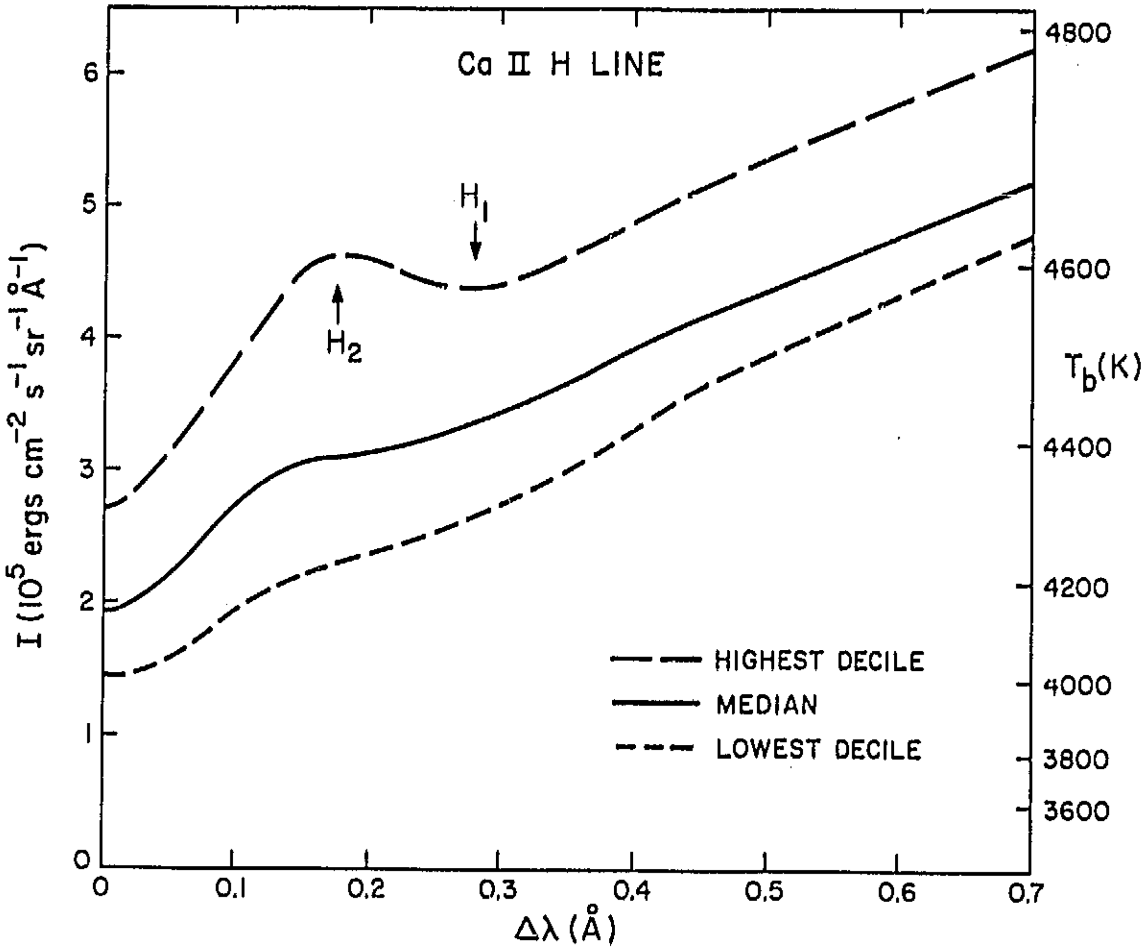

Fig. 4. — Smoothed and symmetrized profiles from Figure 3 plotted on an absolute intensity scale, with corresponding brightness temperatures shown on the the right.

The brightness temperature at the H_1 minimum, or inflection, corresponds approximately to the minimum temperature in the atmosphere along the line of sight. From Figure 4 this implies that the average quiet Sun has a minimum temperature of about 4400K, and that the faintest 10% and the brightest 10% of quiet areas have temperature minima of about 4200K and 4600K, respectively. A more precise interpretation of the H and K intensity minima must account for the effects of partial frequency redistribution. See Linsky (1985) for a review of this topic.

These observations provide information about the temperature minimum and low chromosphere because of the high opacity values near the Ca II line center. Continuous opacities of the same magnitude occur in the far infrared and in the ultraviolet.

In the far infrared near 150 μm the observed continuum brightness temperature passes through a minimum value of about 4400K and becomes larger at larger wavelengths. Approximately the same minimum value is observed near 160 nm in the ultraviolet, and the observed continuum brightness temperature becomes larger at smaller wavelengths. The continuum observations in the 150 μm and 160 nm regions, as of 1980, have been compiled by Vernazza, Avrett, and Loeser (1976, 1981; hereafter VAL-II and VAL-III). More recent observations are shown in Figure 22 of the present paper.

II. The 40-140 nm Continuum

The lower part of Figure 5 shows the increase in chromospheric brightness temperature for extreme ultraviolet wavelengths $\lambda < 140$ nm. The upper part of this figure shows the corresponding disk-center intensities. Here we see the broad wings and central emission of the hydrogen Lα line, centered at 121.57 nm. The far wings of the H and K lines in Figure 1 decrease toward the line center because of the outwardly decreasing photospheric temperature, while the Lα wings increase toward the line center because of the outwardly increasing chromospheric temperature. The three abrupt intensity increases in Figure 5 near 110, 91, and 50 nm are caused by the onset of photoionization from the ground levels of carbon, hydrogen, and helium, respectively.

Apart from the prominent Lα line, the observations in Figure 5 refer only to the continuum values between the many emission lines in the spectrum. The complete spectrum, with the lines labeled, appears in Figure 6. These observations contain a wealth of information, both about the structure of the solar atmosphere and about the detailed radiative and atomic interactions that take place.

Figure 6 shows the spectrum from average quiet regions, from localized active regions, and from "coronal holes" where the high-temperature coronal lines are weak or absent. An off-limb spectrum showing strong coronal lines is also included. The count rate at any given wavelength in Figure 6 is propor-

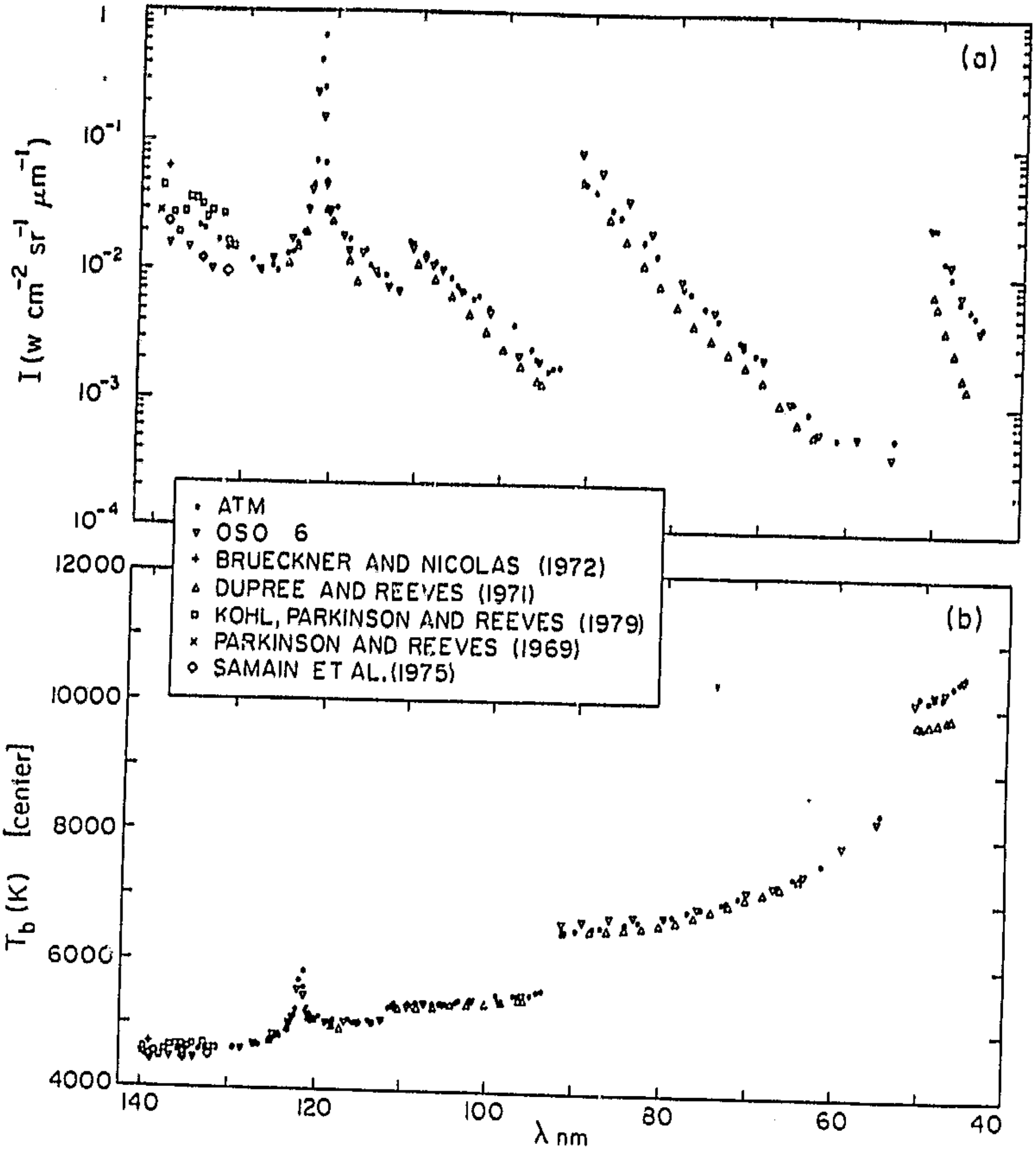

Fig. 5. — Observed values of the disk-center continuum intensity (upper) and the corresponding central brightness temperature (lower) in the 40-140 nm wavelength range. References in the figure are given by VAL-III.

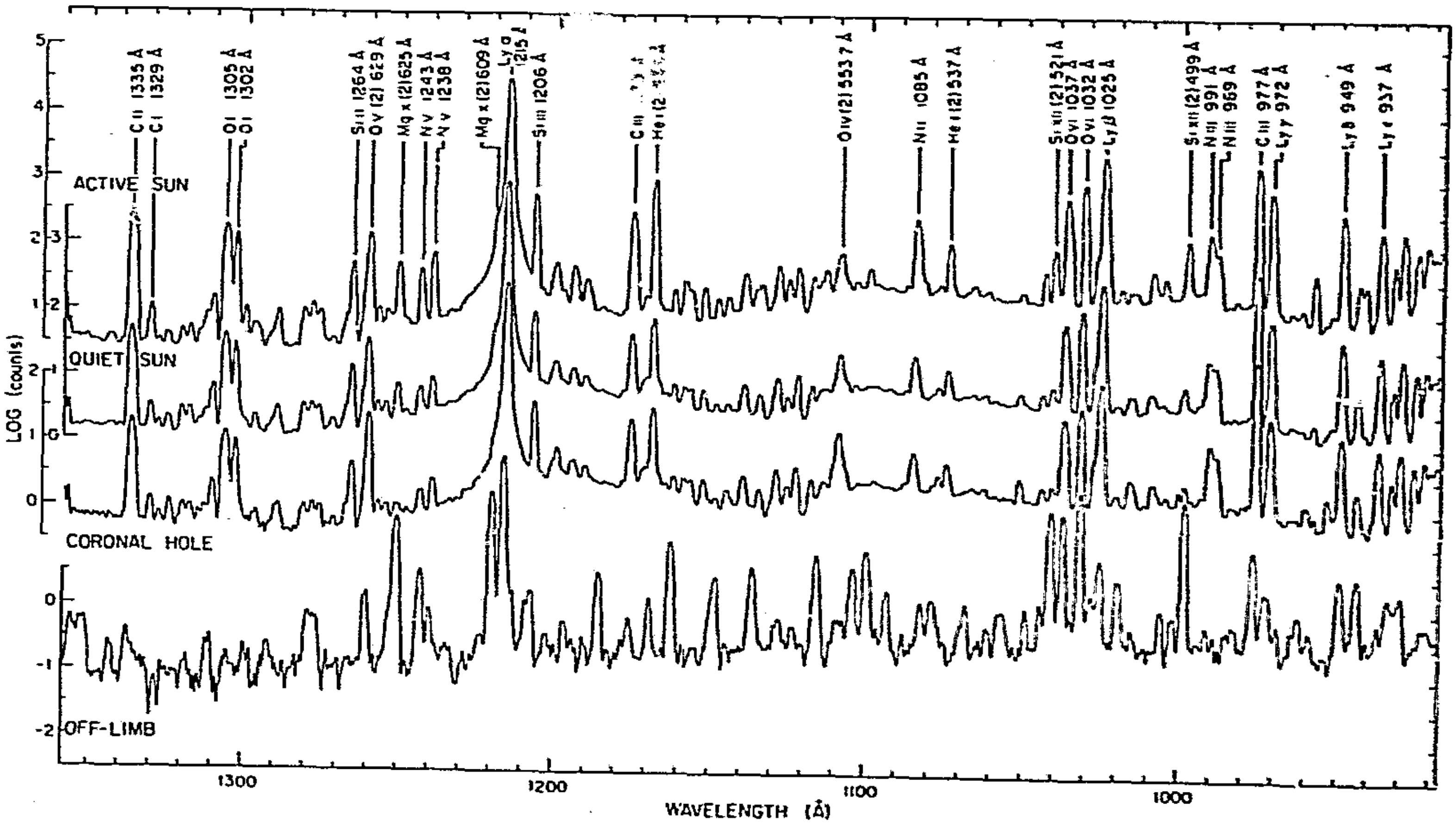

Fig. 6. (above and on the following page) — Average solar spectra between 135 and 49 nm from a quiet region, a coronal hole, an active region, and a quiet area off the limb. The individual spectra are displaced from each other for clarity. From Vernazza and Reeves (1978).

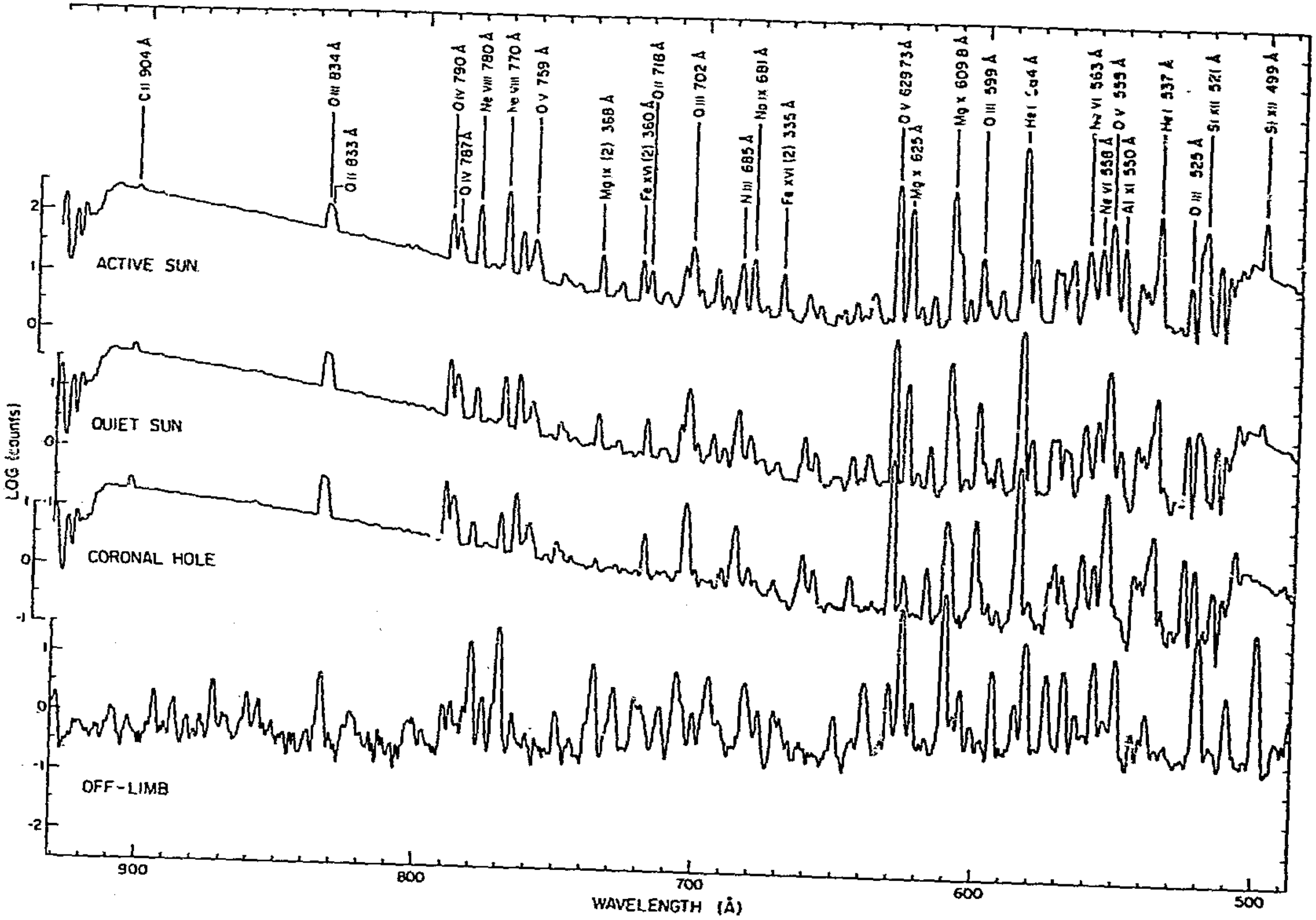
C II 904 Å
O III 834 Å
O II 833 Å
O IV 790 Å
O IV 787 Å
Ne VIII 780 Å
Ne VIII 770 Å
O V 759 Å
Mg IX (2) 368 Å
Fe XVI (2) 360 Å
O II 718 Å
O III 702 Å
N III 685 Å
Na IX 681 Å
Fe XVI (2) 335 Å
O V 629.73 Å
Mg X 625 Å
Mg X 609.8 Å
O III 599 Å
He I 584 Å
Ne VI 563 Å
Ne VI 558 Å
O V 559 Å
Al XI 550 Å
He I 537 Å
O III 525 Å
Si XII 521 Å
Si XII 499 Å
ACTIVE SUN
QUIET SUN
CORONAL HOLE
OFF-LIMB
LOG (counts)
2
1
0
-1
-2
900
800
700
600
500
WAVELENGTH (Å)

tional to intensity. At 90 nm the coronal-hole intensity is about a factor of 2 less than the quiet-Sun intensity, but active regions are 5 to 6 times brighter than quiet regions at this wavelength.

Different components such as quiet and active regions and coronal holes clearly have different intensities. As in the case of the Ca II lines, substantial brightness variations also occur within quiet regions. Figure 7 shows the pattern of brightness variations over 5′x5′ quiet areas seen at extreme ultraviolet wavelengths. The pattern is a "network" of bright chromospheric emission enclosing darker areas often called "cells".

From histograms of the brightness distribution of such patterns, six components A through F have been selected, ranging from a dark point within a cell (component A, the darkest 8%) to a very bright network element (component F, the brightest 4%). At 90.7 nm the darkest 8% of the observed quiet area has an intensity about 0.4 times the average, while the intensity of the brightest 4% is almost 3 times the average. See VAL-III for details.

Figure 8 shows the intensity distribution for components A through F at those wavelengths in the 40-140 nm range where continuum intensities can be easily identified. The component C distribution represents the average quiet Sun and is essentially the same as the spatial-average intensity distribution in Figure 5.

III. Model Calculations

Now consider the determination of the temperature and density variation along the line of sight from these and other observations. The observed brightness temperatures at various wavelengths indicate the approximate kinetic temperatures that occur at unit optical depth for these wavelengths, apart from the differences between brightness and kinetic temperatures caused by departures from LTE.

The optical depth at any wavelength depends on the wavelength-dependent properties of the absorbing atoms and on the atomic number densities along the line of sight. The number densities depend on a balance between the solar surface gravity, which compresses the atmosphere, and the gas pressure, including kinetic and magnetic effects, which expands it.

In the static case with only gas pressure opposing gravity, the pressure varies with geometrical depth x according to the hydrostatic equilibrium solution

$$p(x) = p(x_0) \exp\left[\int_{x_0}^{x} \frac{dx'}{H(x')}\right]. \qquad (1)$$

ORIGINAL PAGE IS
OF POOR QUALITY

1973 JULY 8

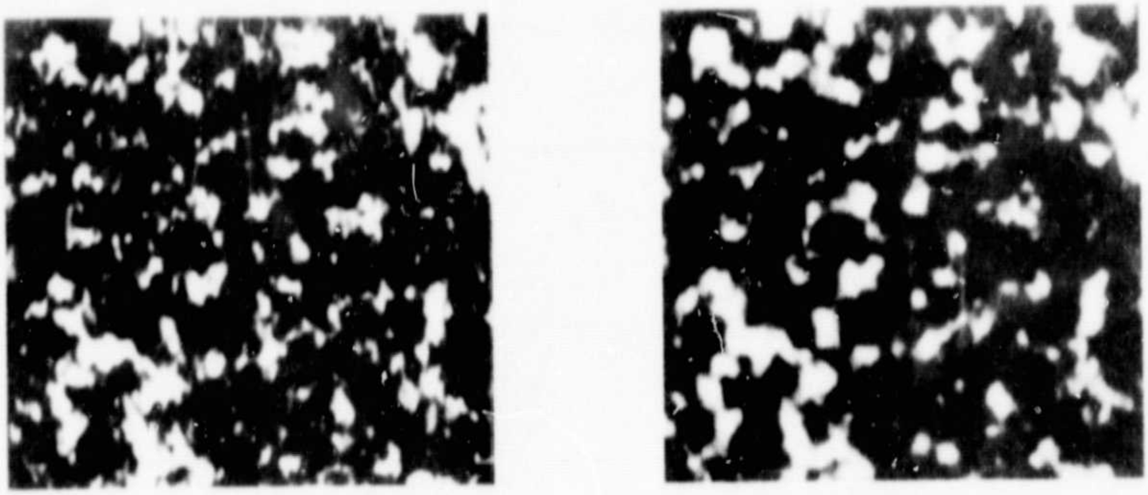

C I Continuum (λ=104.4nm) Lyman Continuum (λ=74.0nm)

1973 JULY 9

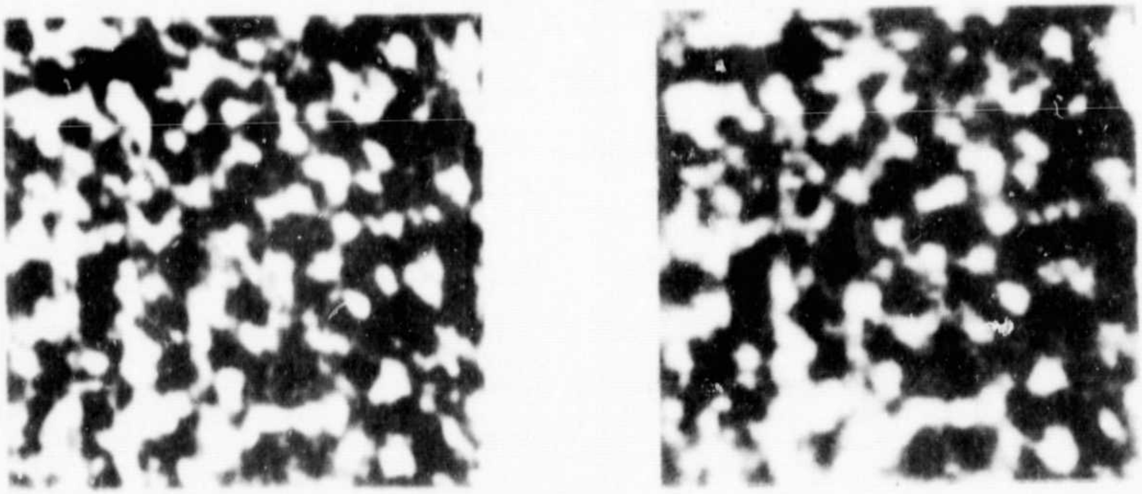

Lyman Alpha Wing (λ=121.1nm) Lyman Continuum (λ=90.7nm)

Fig. 7. — *Skylab* spectroheliograms of two $5'$ by $5'$ areas of the quiet Sun. From VAL-III.

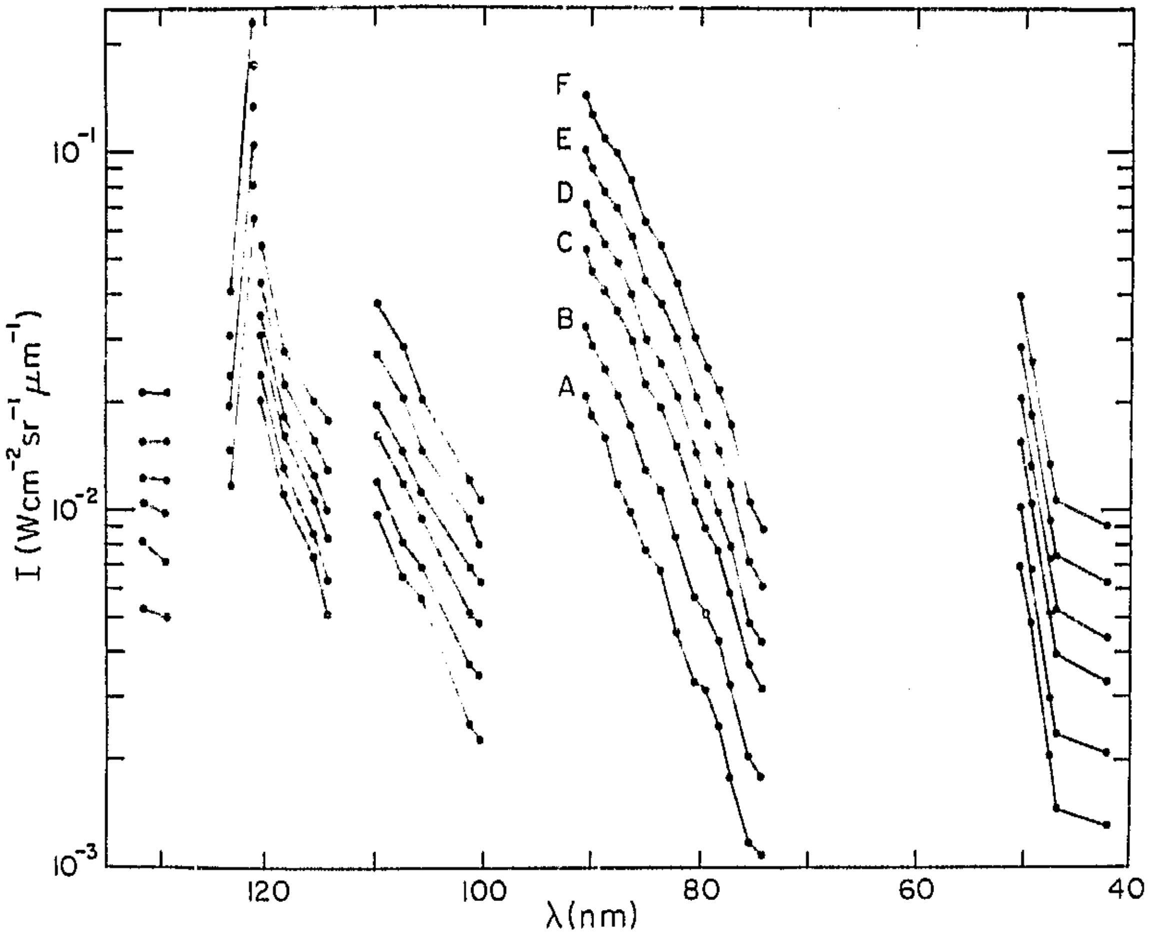

Fig. 8. — Observed quiet-Sun continuum intensities in the 40-140 nm range for brightness components A through F.

In this case, H is the static pressure scale height H_s given by

$$H_s = \frac{(1+r_{He}+r_e)kT}{gm_H(1+4r_{He})}, \tag{2}$$

where r_{He} is the helium fraction (assumed to be 0.1) and $r_e = n_e/n_H$ is the calculated electron number density relative to hydrogen. If there are turbulent motions, the total pressure p is the sum of the gas pressure and the turbulent pressure

$$p_{turb} = (1/2)\rho v_{turb}^2, \tag{3}$$

where ρ is the gas density and v_{turb} is an assumed turbulent velocity parameter. Then the pressure scale height is

$$H = H_s+(1/2g)v_{turb}^2. \tag{4}$$

Values of v_{turb} can be obtained from the nonthermal line broadening velocities that must be introduced to account for the observed Doppler widths of various lines. These are the only velocities considered here. Magnetic-field effects are not considered.

Given T, v_{turb}, and r_e as functions of x, one can determine p(x) from equation (1), apart from a normalizing constant. The electron fraction r_e depends on T and p and other calculated parameters; the pressure equation is normalized so that continuum optical depth unity at 500 nm occurs at a fixed photospheric reference depth, namely at the zero point of the adopted geometrical height scale. Thus p(h) can be obtained given T(h) and $v_{turb}(h)$, where h is the height above $\tau_{500} = 1$.

Given p and T, one can compute the number densities, opacities, and monochromatic optical depths. The various atomic number densities are obtained by excitation and ionization calculations that depend not only on p and T but also on the radiation intensity as a function of depth and wavelength. The radiation intensity at each depth depends, in turn, on the number densities at surrounding depths. These interactions are determined by solving the equations of statistical equilibrium and radiative transfer. Thus, given T(h) and v_{turb}, one can then calculate all needed atmospheric parameters and, finally, the emergent intensity as a function of wavelength.

The computed chromospheric spectrum is relatively insensitive to the chosen values of v_{turb}, even though the geometrical thickness of the atmosphere increases substantially as v_{turb} is increased. Figure 9 shows the adopted $v_{turb}(h)$ distribution (from VAL-III), based on Doppler line widths that are observed to exceed thermal widths. For simplicity this distribution is used for all brightness components A through F. The atmospheric model then depends only on T(h).

Figure 10 shows the temperature distribution obtained by trial and error so that the computed emergent intensity agrees with various observations of the average quiet Sun. The temperature is shown as a function of both h(km) and the column mass m(g cm^{-2}), which equals p/g from the hydrostatic equilibrium equation. Figure 10 also shows the approximate depth regions where the various continua and line components originate.

The ultraviolet continuum near 160 nm, the far infrared continuum near 150 μm, and the minima in the wings of the Ca II and Mg II resonance lines all are formed in the temperature minimum region near h = 500km. The Ca II and Mg II emission peaks, the hydrogen Hα line center, the millimeter continuum and carbon 110 nm continuum, and the wing of Lα at 1Å and 5Å from line center all are formed in a broad 5500-7000K temperature plateau that characterizes most of the chromosphere. The Ca II and Mg II resonance line

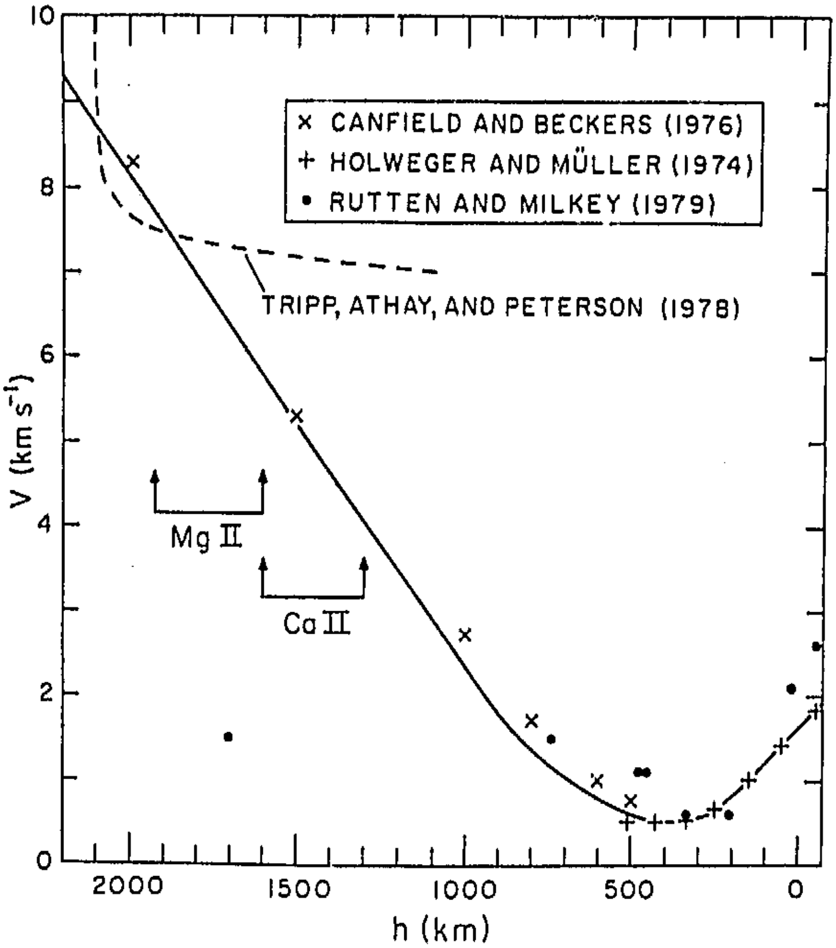

Fig. 9. — The adopted turbulent velocity distribution compared with values given by various authors.

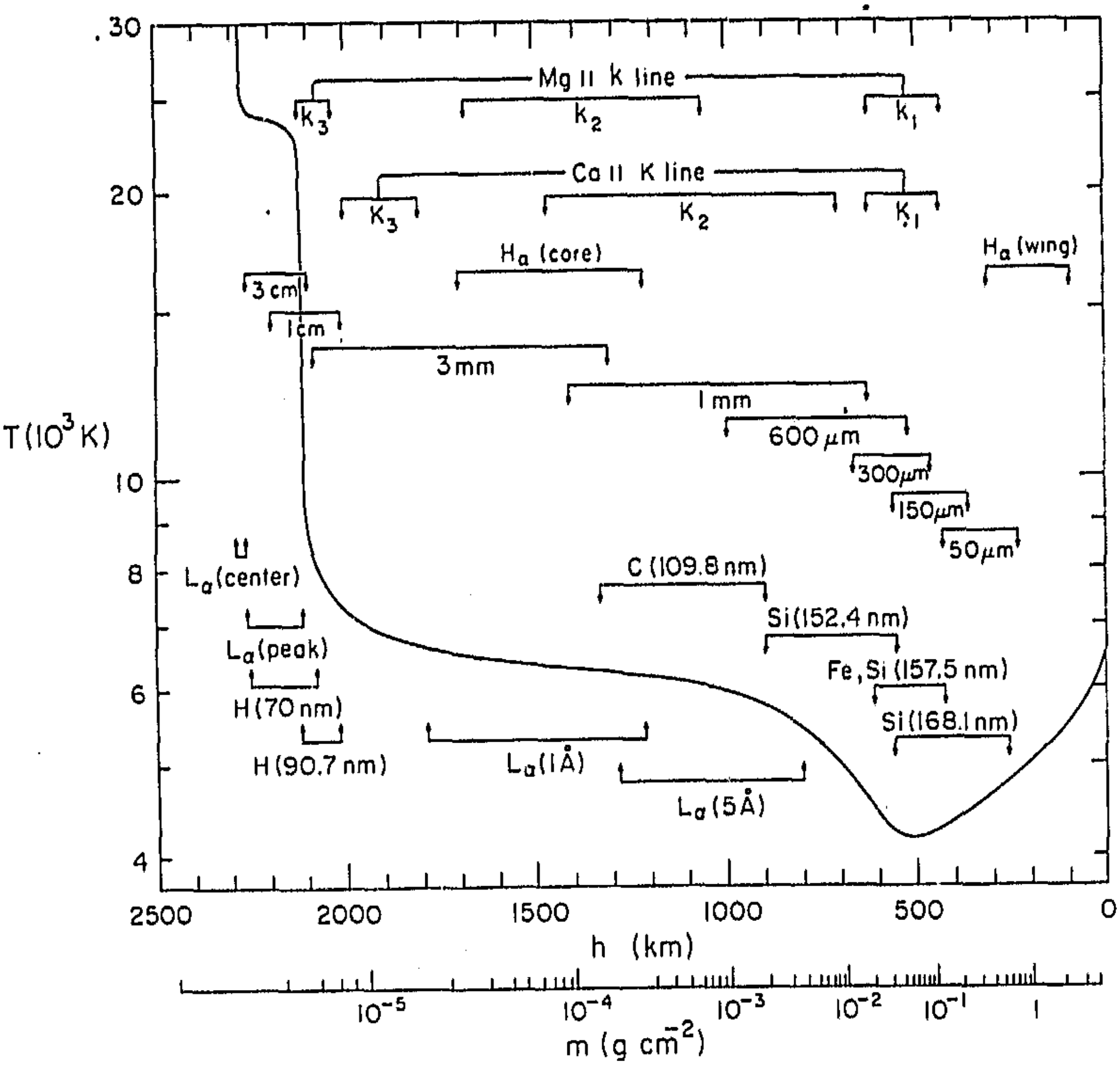

Fig. 10. — The Model C temperature distribution, from VAL-III.

centers, the centimeter continuum, and the hydrogen Lyman continuum all are formed at the base of the chromosphere-corona transition region where the temperature increases abruptly. The central part of the Lα line and the 3 cm continuum are formed at 20,000-30,000K temperatures.

The plateau near 25,000K has been introduced to account for 1) the Lα and Lβ integrated intensities, 2) the central absorption observed in these lines, and 3) the short-wavelength intensity in the Lyman continuum. The plateau could be replaced by a more gradual temperature rise between 10,000 and 30,000K, adjusted to give the observed values of the integrated Lyman line intensities, but the calculated Lβ line would not have the central absorption that is observed, and Lα would have less central absorption than observed. As discussed later, no physical mechanism has been identified to explain such a plateau. A one-dimensional model may not properly characterize the real three-dimensional atmosphere in this respect; the plateau may signify only that the line of sight passes through material of the indicated thickness at the indicated temperatures.

Figure 10 also shows the depths at which the Hα line core and wing are formed. The reason for the separation of the core and wing depths is that the hydrogen $n = 2$ level population is negligible throughout the temperature minimum region. Spectroheliograms taken in a narrow wavelength band centered on Hα therefore show chromospheric structure and behavior with little photospheric contamination. Displacing the band slightly from the line center enhances the relative brightness of different chromospheric features having different velocities along the line of sight. Spectacular photographs of chromospheric inhomogeneities are obtained in this way.

The temperature distribution in Figure 10 corresponds to the component C observations in Figure 8. The temperature distributions found in the same way for components A through F are shown in Figure 11. Note that the six curves all resemble each other in showing a gradual increase in the 6000-7000K temperature range and a very rapid increase above 8000K. Brighter components have higher temperatures at all depths and have chromosphere-corona transition regions located closer to the photosphere, at higher pressures. Note, however, that the same $v_{turb}(h)$ is used for all six components.

Active-region models based on the same $v_{turb}(h)$ have temperature enhancements relative to Model F that are comparable to the temperature differences between Models A and F, and have transition regions located even closer to the photosphere. See Basri *et al.* (1979). However, increasing the values of $v_{turb}(h)$ would move the transition region to greater heights.

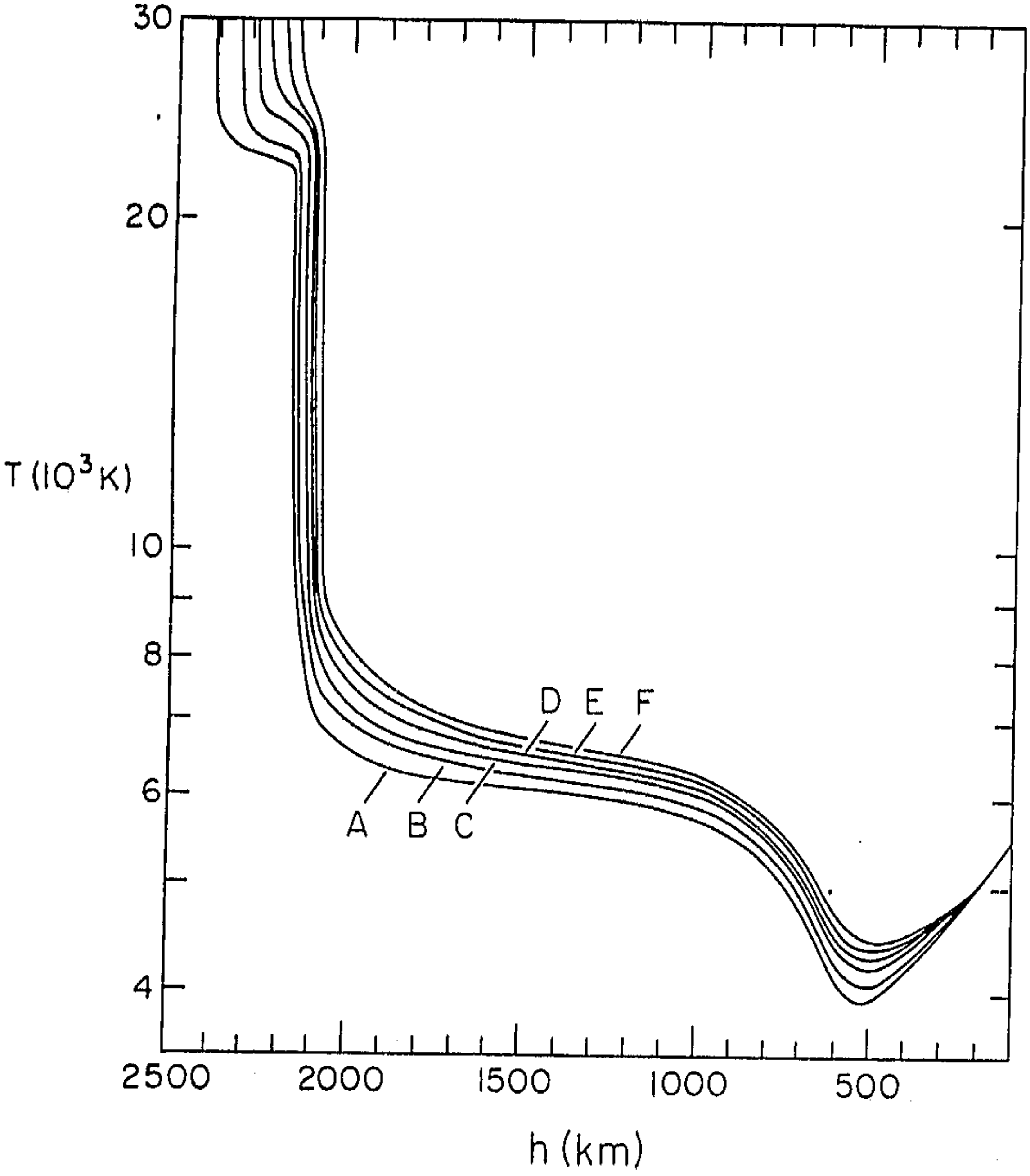

Fig. 11. — The temperature as a function of height for Models A through F.

IV. The Temperature Minimum Region

The VAL-III temperature-minimum values were based on the 135-168 nm ultraviolet continuum observations shown in Figure 12. The temperature distributions for Models A through F in the minimum region are shown in Figure 13. Model C is similar to the Harvard-Smithsonian Reference Atmosphere, HSRA, of Gingerich *et al.* (1971), which was based on similar ultraviolet continuum observations. Figure 13 also shows the higher temperature-minimum values of Ayres and Linsky (1976), determined from a fit to the Ca II and Mg II lines. They obtain a quiet-Sun minimum temperature of 4450K compared with the Model C value of 4170K.

As discussed in the VAL-III paper, the 4170K minimum temperature appears to be too low for the following reasons. 1) The observed Ca II K_1 minimum intensity is larger than that calculated from Model C by a factor of about 1.6. 2) Rast, Kneubühl, and Müller (1978) found that the minimum observed brightness temperature in the far infrared is 4530(+100,-150)K near 130 μm, which is larger than the value computed from Model C by about 200K. (This is a higher observed minimum than suggested by the data compiled in 1976 by VAL-II). 3) Comparisons with the ultraviolet center-to-limb observations of Samain (1978, 1980) show that the Model C temperature decreases too rapidly with height on the photospheric side of the minimum and then increases too rapidly on the chromospheric side. Thus the calculated models of the temperature minimum region based on the 135-168 nm continuum intensities in Figure 12 appear to be incorrect.

A major uncertainty in the calculations is how to deal properly with the many lines throughout the spectrum. The lines are important 1) in calculating the photoionization-rate integrals that effect the ionization equilibrium of Si, Mg, Fe, C, Al, and other atoms, and 2) in calculating the spectrum for direct comparison with observations.

R. Kurucz has computed new opacity tables based on more than 1.7×10^7 atomic and molecular lines. These tables can be used to compute a detailed spectrum for comparison with observations, as shown in Figure 14 (from Avrett and Kurucz 1983). The darker curve in this figure represents the observed, uncalibrated, intensity from the Preliminary Kitt Peak Photoelectric Atlas (Brault and Testerman 1972) while the calculated intensity is shown as the lighter curve. (See Kurucz and Avrett 1981 for an explanation of the printed atomic and molecular identifications.) In the wavelength interval shown in Figure 14 the line list appears to give an adequate representation of the observed spectrum. Comparisons in other wavelength regions show that many lines in the observed spectrum are not included in the current opacity tables, but these new opacities give much better results than the approximations used previously.

ORIGINAL PAGE IS
OF POOR QUALITY

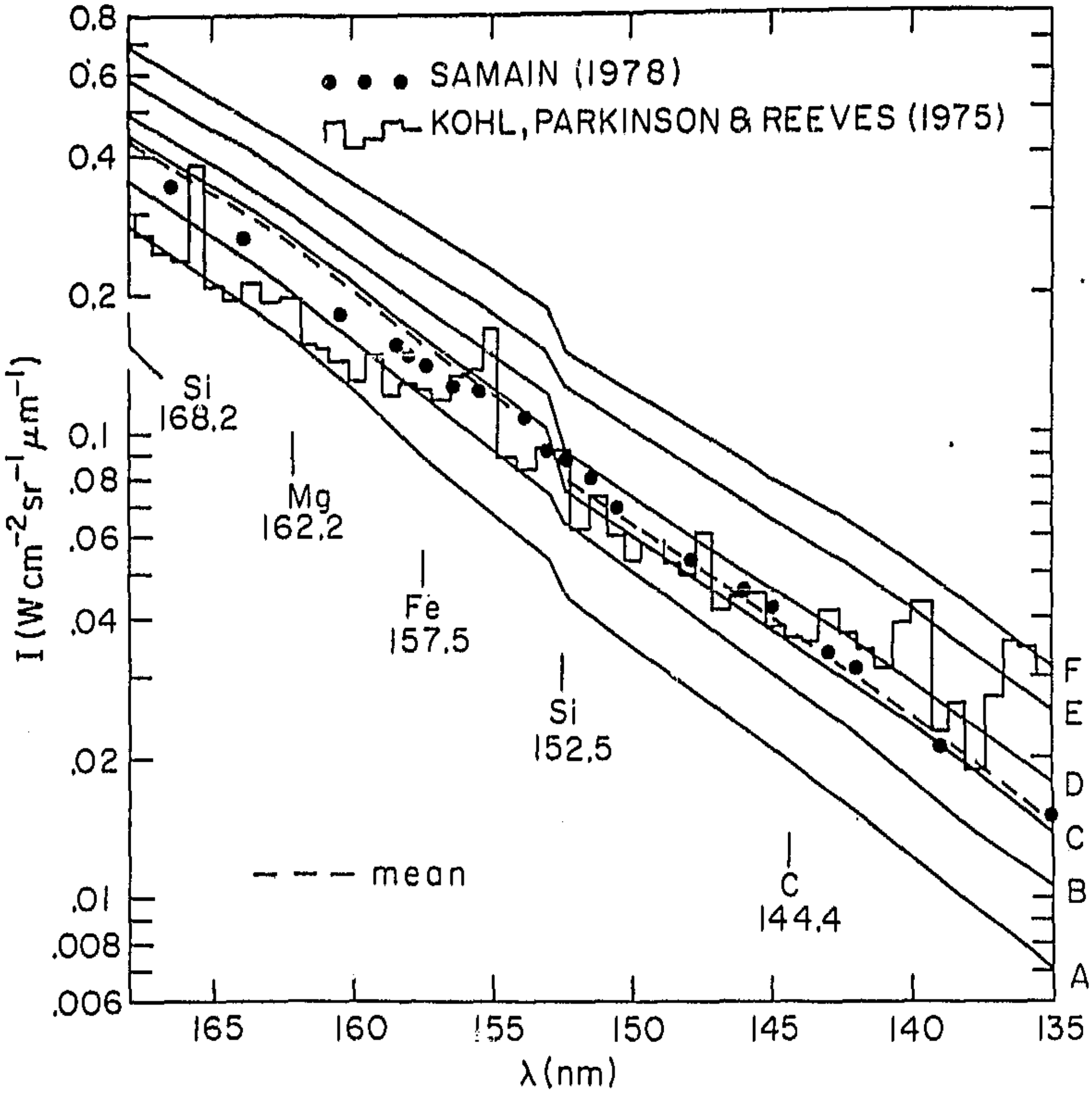

Fig. 12. — Observed and calculated intensities in the 160 nm wavelength range. From VAL-III.

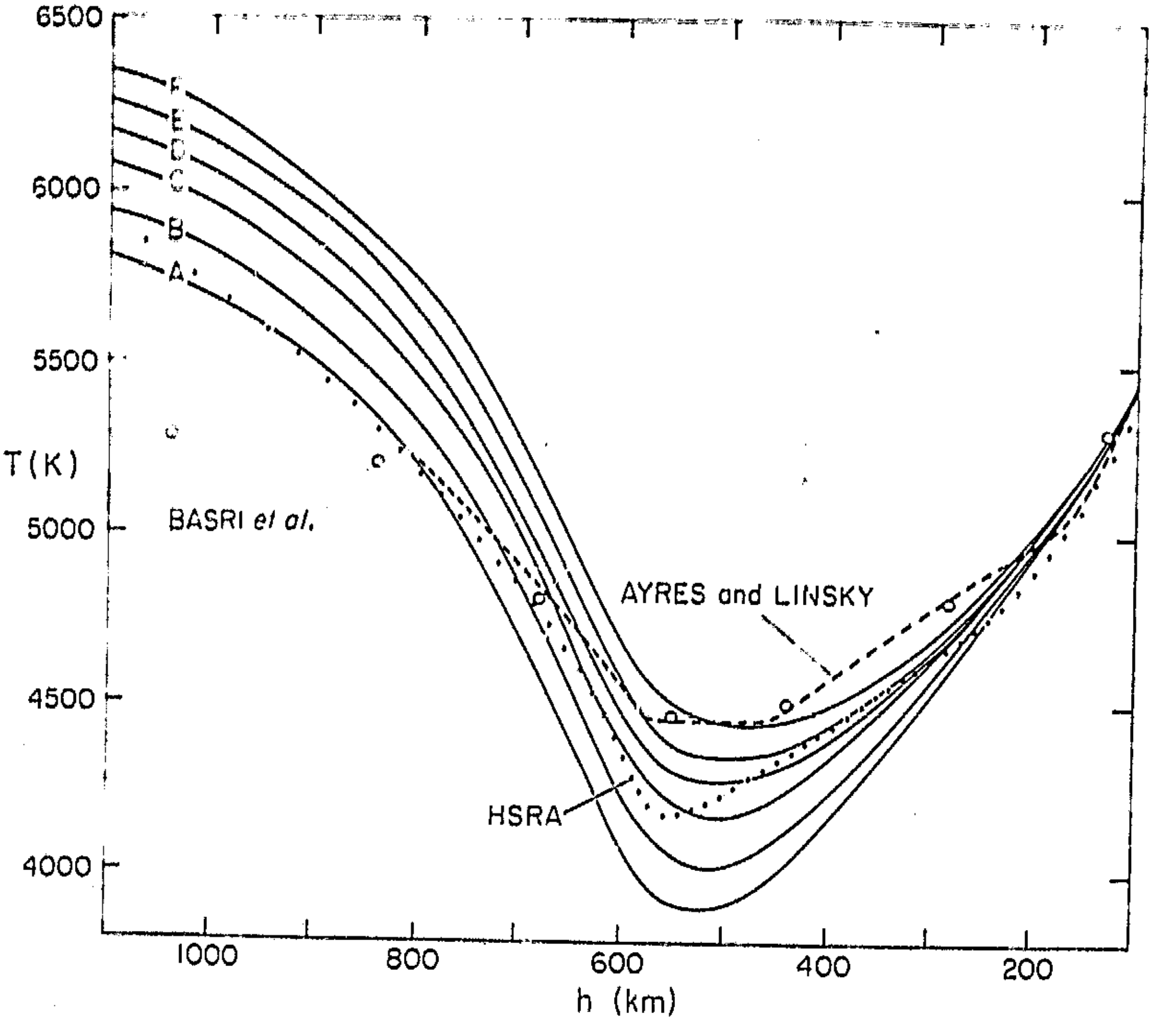

Fig. 13. — Comparison between Models A—F and other models in the temperature minimum region.

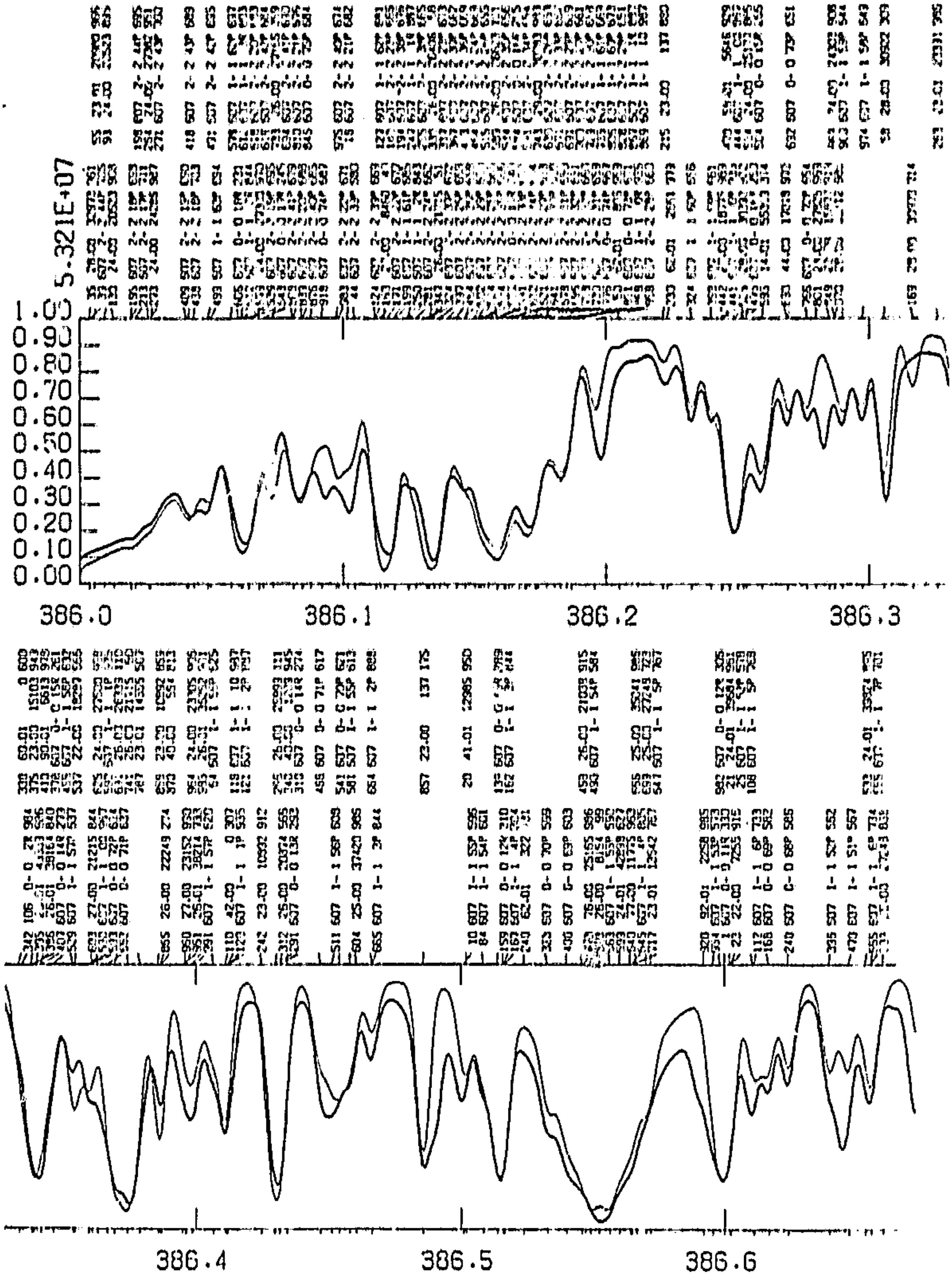

Fig. 14. — Calculated spectrum (lighter curve) in the 386 nm wavelength range compared with the spectrum observed by Brault and Testerman (1972). From Avrett and Kurucz (1983).

As reported by Avrett, Kurucz, and Loeser (1984), the VAL-III calculations were repeated using the total line opacity (as a function of temperature and pressure) sampled at 7,000 wavelengths between 140 and 605 nm. The more realistic line opacities imply higher minimum temperatures than before, because 1) the ionization equilibrium of Si, Mg, and Fe in the temperature-minimum region is closer to LTE than in the earlier calculations, and 2) weak lines affect the interpretation of the apparent continuum in the 140-168 nm region.

Figures 15 and 16 show a compilation of observed disk-center intensities, and corresponding brightness temperatures, between 1 μm in the infrared and 125 nm in the ultraviolet. Figure 15 includes two sets of observations, the broad-band intensity distribution and the maximum intensities at selected wavelengths between absorption lines.

The crosses in Figures 15 and 16 are the newly- calculated broad-band intensities; each cross (70 in all) represents the average of 100 individual intensities. To compensate for missing lines, all opacities for $\lambda < 386$ nm have been multiplied by the factor 1.2, but there are still some discrepancies in the 210-230 nm region.

These calculations were made with a new Model C′ having a minimum temperature distribution close to that of Ayres and Linsky (1976), as shown in Figure 17. This figure also shows the temperature as a function of height for new Models A′ and F′. The three new models have the same temperature-height distributions as Models A, C, and F in the chromosphere above the minimum region.

Figure 18 shows a comparison of the H line profiles from Models A′, C′, and F′ with the three observed profiles shown earlier. We attempted to adjust each T(h) to fit these observations but, in view of numerous uncertainties, did not feel justified in choosing a minimum temperature for Model C′ any higher than that of Ayres and Linsky, since they obtained good agreement with the observed K line profile.

These calculated H_1 minima generally agree with the corresponding observed features to within about 20%, much better than the disagreement by the factor 1.6 noted earlier for Model C. Part of the remaining discrepancy may be due to uncertainties in the theory of partial frequency redistribution applied to the formation of these lines. (See VAL-III and Linsky 1985.)

The new results are compared with the 160 nm observations in Figure 19, which gives the Model C′ intensities that should correspond to Samain's observed values between various strong lines (mostly emission lines) in this wavelength range. This figure also shows the corresponding intensity distributions calculated from Models A′ and F′. The new higher-temperature average model fits the spatial-average observations as well as before, because the more accurate treatment of line opacities forces the ionization equilibrium of silicon

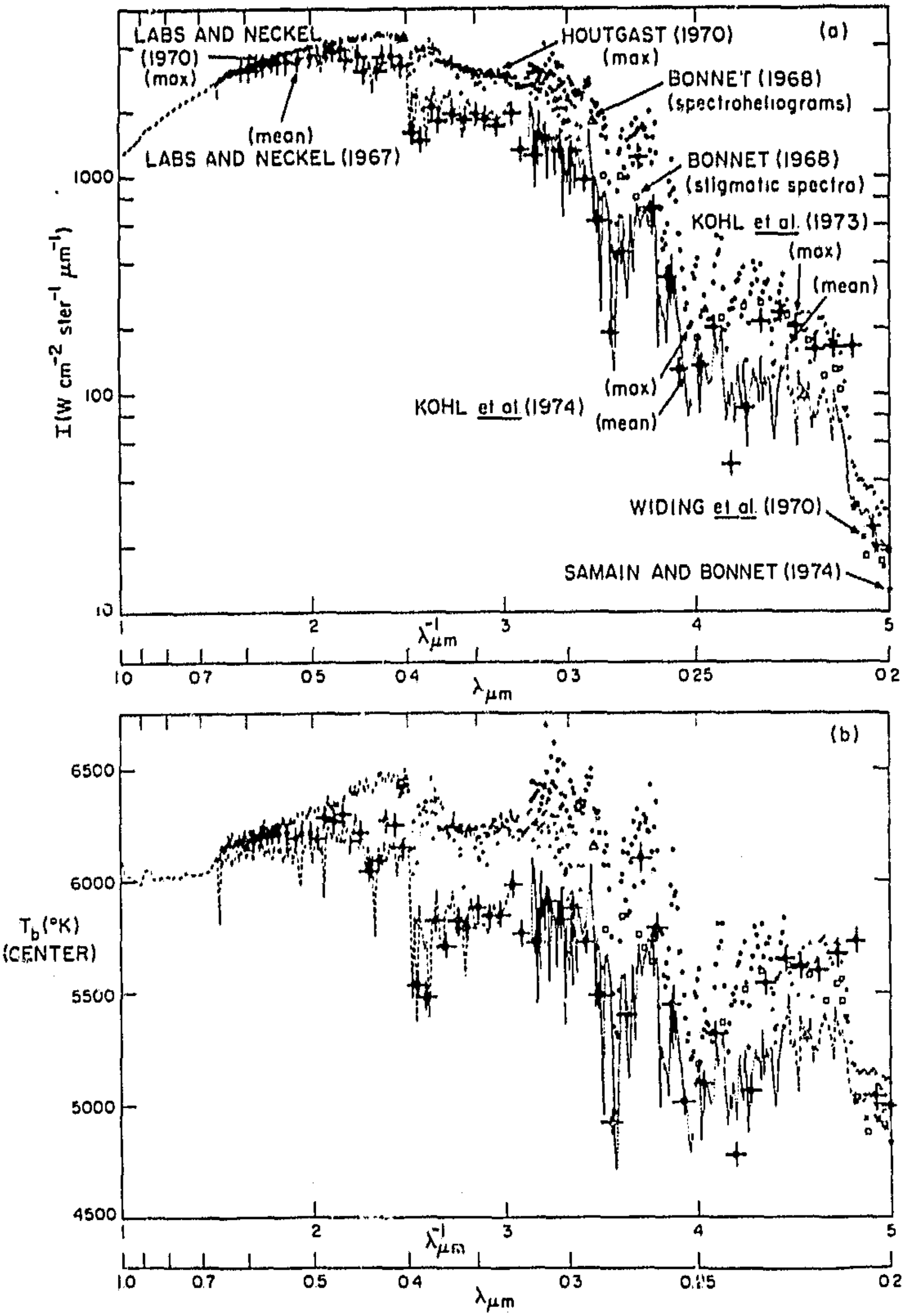

Fig. 15. — Observed central intensities and the corresponding brightness temperatures between 200 nm and 1 μm. Crosses represent the broad-band calculated intensities described in the text. Original figure and references from VAL-II.

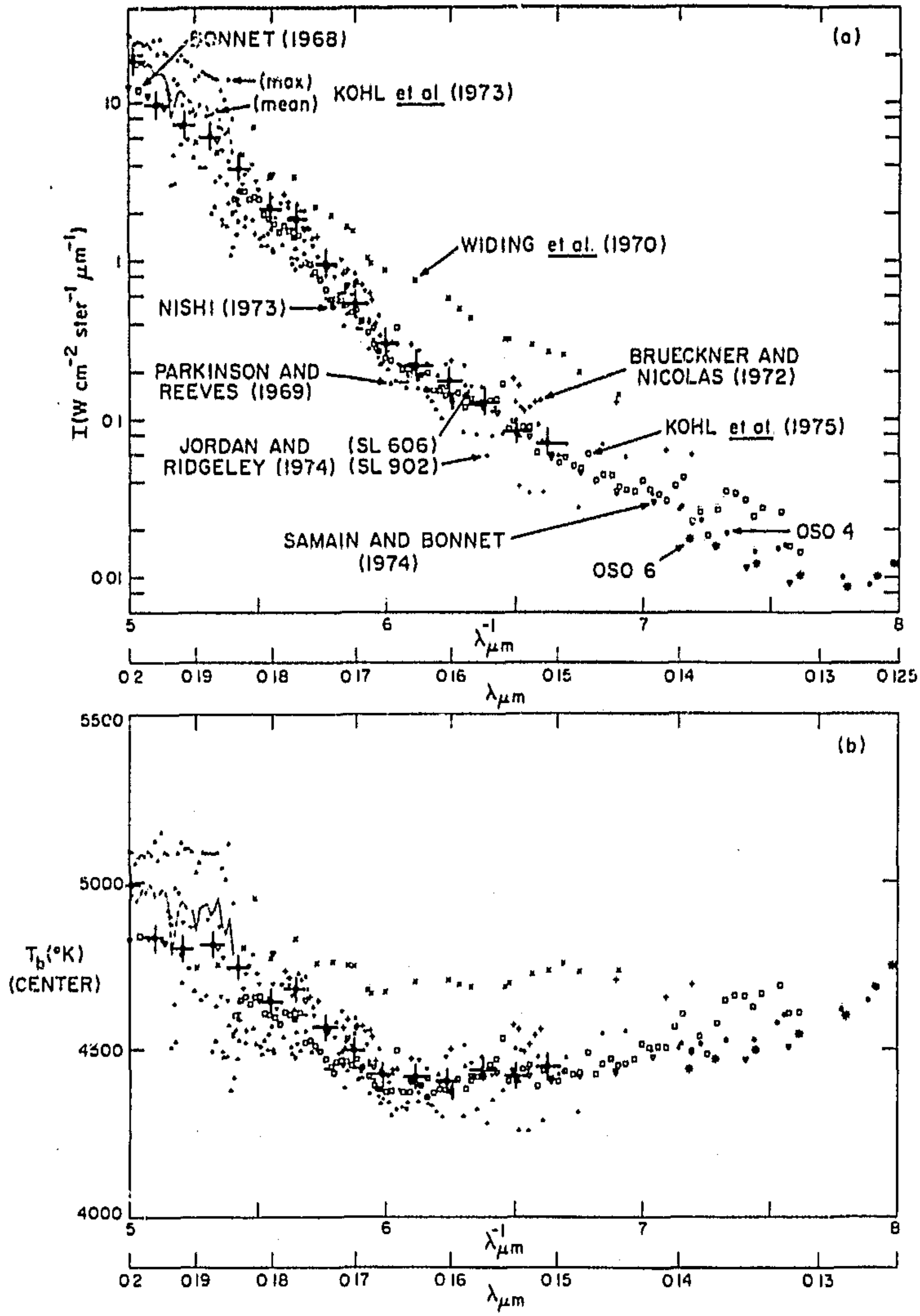

Fig. 16. — Observed central intensities and the corresponding brightness temperatures in the 125-200 nm range. Crosses represent the broad-band calculated intensities. Original figure and references fom VAL-II.

and other atoms to be closer to LTE. In the new calculations, the silicon continuum source function at h = 500 km in this ultraviolet wavelength range is only about 30% larger than the Planck function, vs. 3 to 4 times larger in the VAL-II and -III calculations, and in similar calculations by Cuny (1971).

The A′ and F′ ultraviolet intensities in this figure are those corresponding to the lowest- and highest-decile calcium line profiles in Figure 18. At 168 nm the F′ intensity is about 3.5 times larger than the A′ intensity. Such a differ-

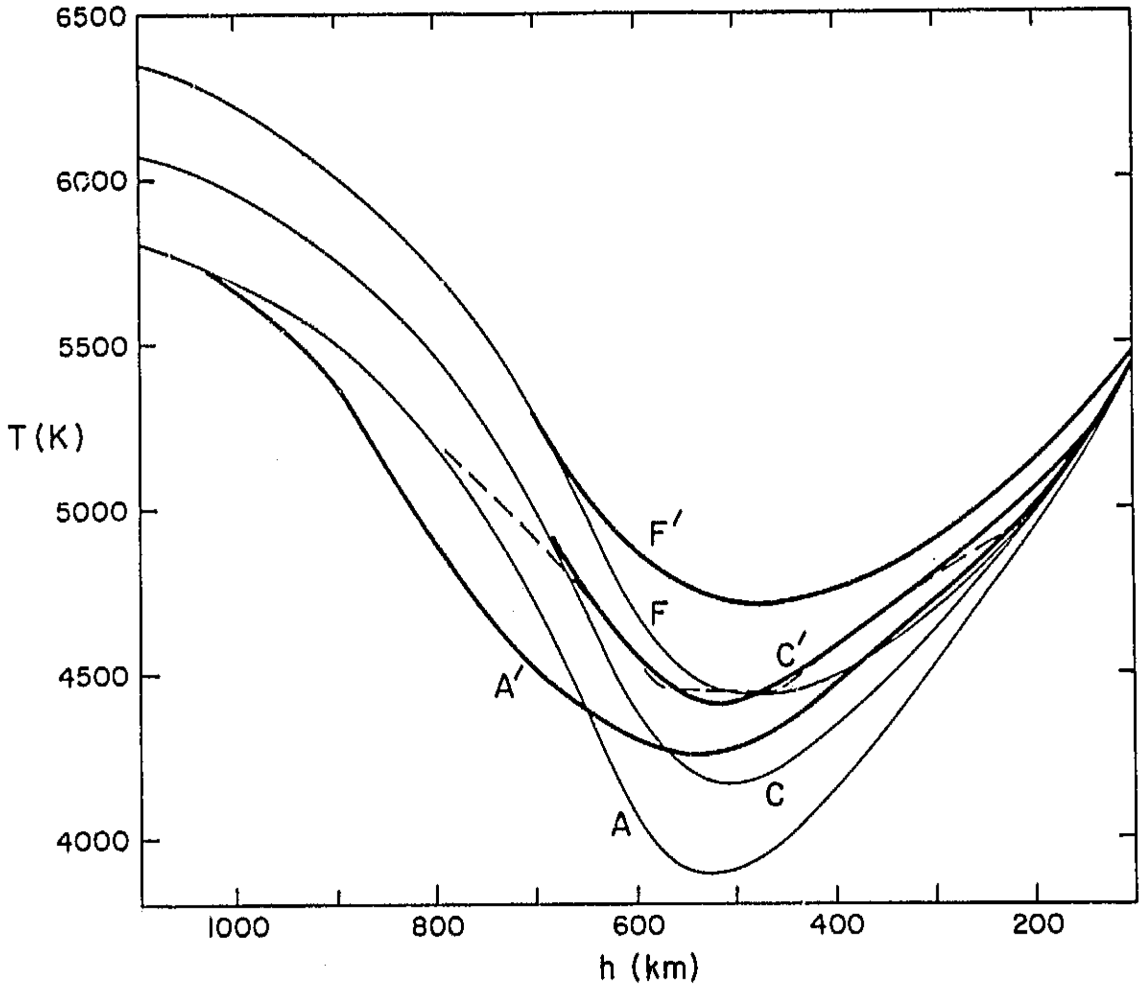

Fig. 17. — Temperature distributions in the minimum region for Models A′, C′, and F′ compared with Models A, C, and F from VAL-III, and with the Ayres and Linsky model (shown as a dashed line).

ence seems consistent with the quiet-Sun intensity variations with position observed by Cook, Brueckner, and Bartoe (1983), as shown in the upper part of Figure 20. The lower part of this figure shows the intensity variations with position across a plage region. Similar intensity scans at 160 nm by Foing and Bonnet (1984) are shown in Figure 21. Much could be learned from a study of the correlations between such high-resolution intensity variations in the ultraviolet minimum region and simultaneous high-resolution intensity variations in the Ca II K_1 or H_1 minima.

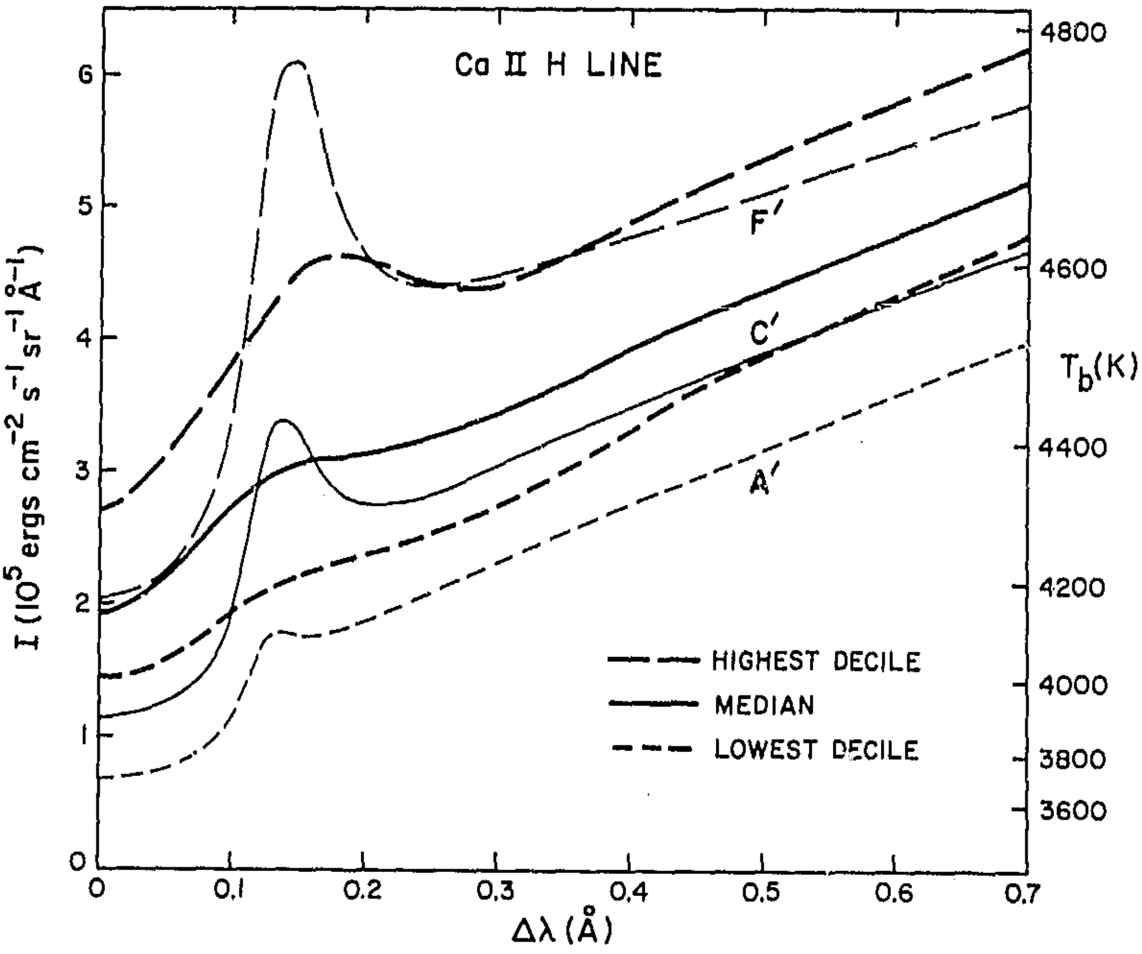

Fig. 18. — H-line profiles calculated from Models A′, C′, and F′ (lighter curves) compared with the Cram and Damé observed profiles (darker curves).

ORIGINAL PAGE IS
OF POOR QUALITY

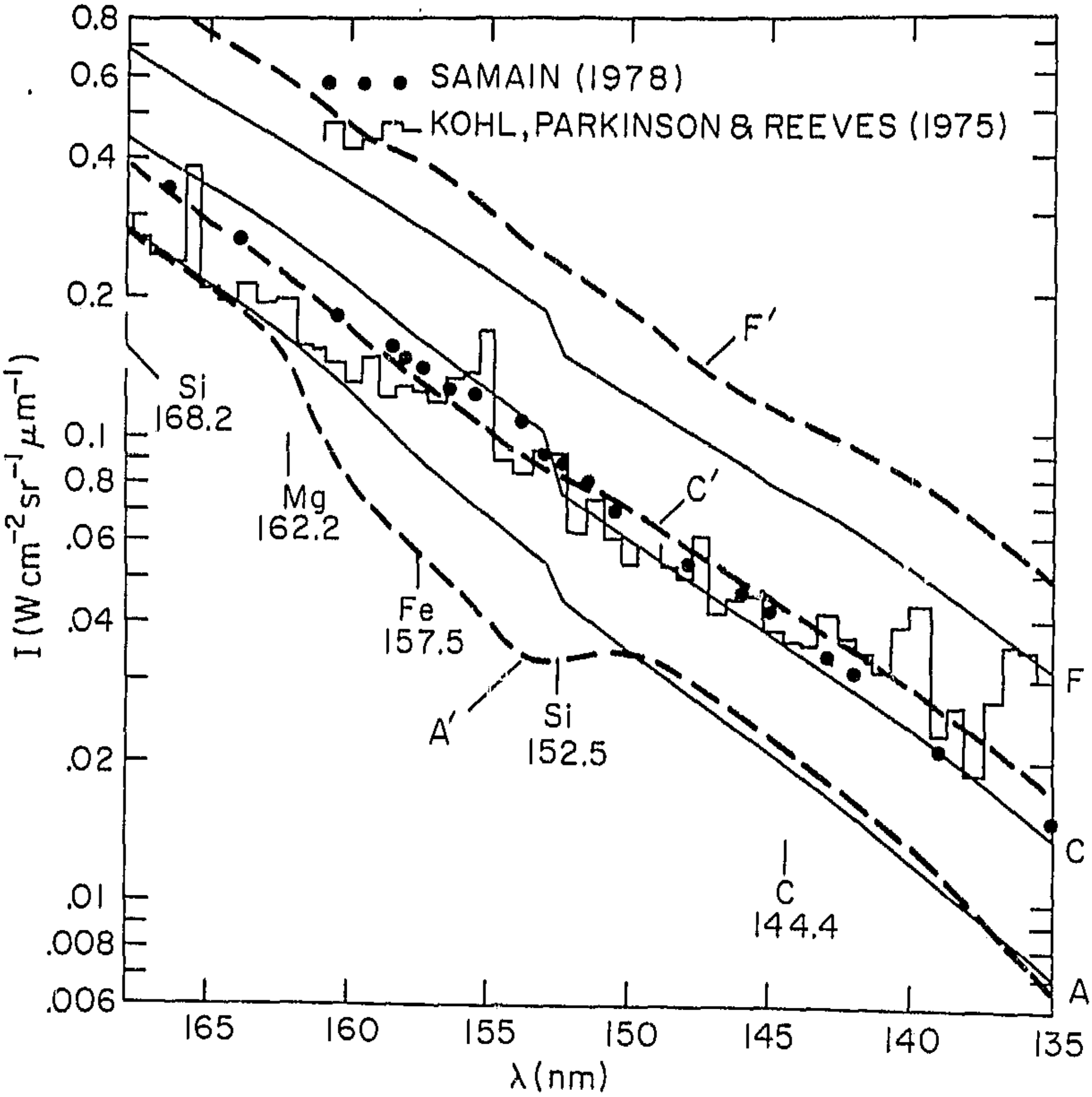

Fig. 19. — Ultraviolet intensities calculated from Models A′, C′, and F′ (with lines included throughout the spectrum as described in the text) compared with observations and earlier calculations.

Finally, the calculated and observed brightness temperatures in the far infrared are compared in Figure 22. This figure shows the observed minimum value 4530(+100, -150)K at 130 μm from Rast, Kneubühl, and Müller (1978) and recent observations at 50, 80, and 200 μm reported by Degiacomi (1984). (See also Degiacomi *et al.* 1984.) The open circles represent quiet-Sun observations, while the filled circles represent the higher values obtained when active regions were present within the area observed. Individual (small-scale) active regions cannot be resolved with the 60 cm telescope used for these submillimeter wavelength observations.

Model C′ appears to be in adequate agreement with the quiet-Sun observations in Figure 22. Thus, a minimum temperature of 4400 or 4500K for the average quiet Sun seems consistent with the Ca II, 160 nm, and 150 μm data.

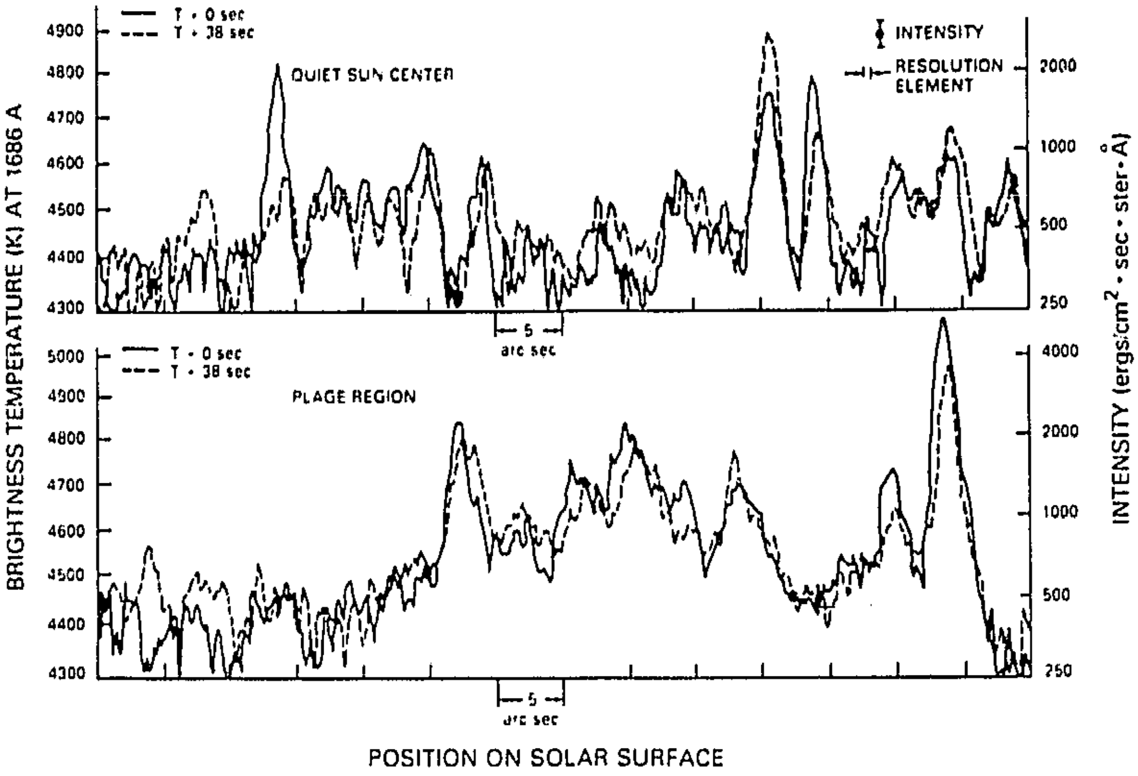

Fig. 20. — The absolute intensity and corresponding brightness temperature at 168.6 nm from quiet and plage regions at two times, 30 s apart, from slit spectra obtained during a rocket flight of the Naval Research Laboratory's High Resolution Telescope and Spectrograph (Cook, Brueckner, and Bartoe 1983).

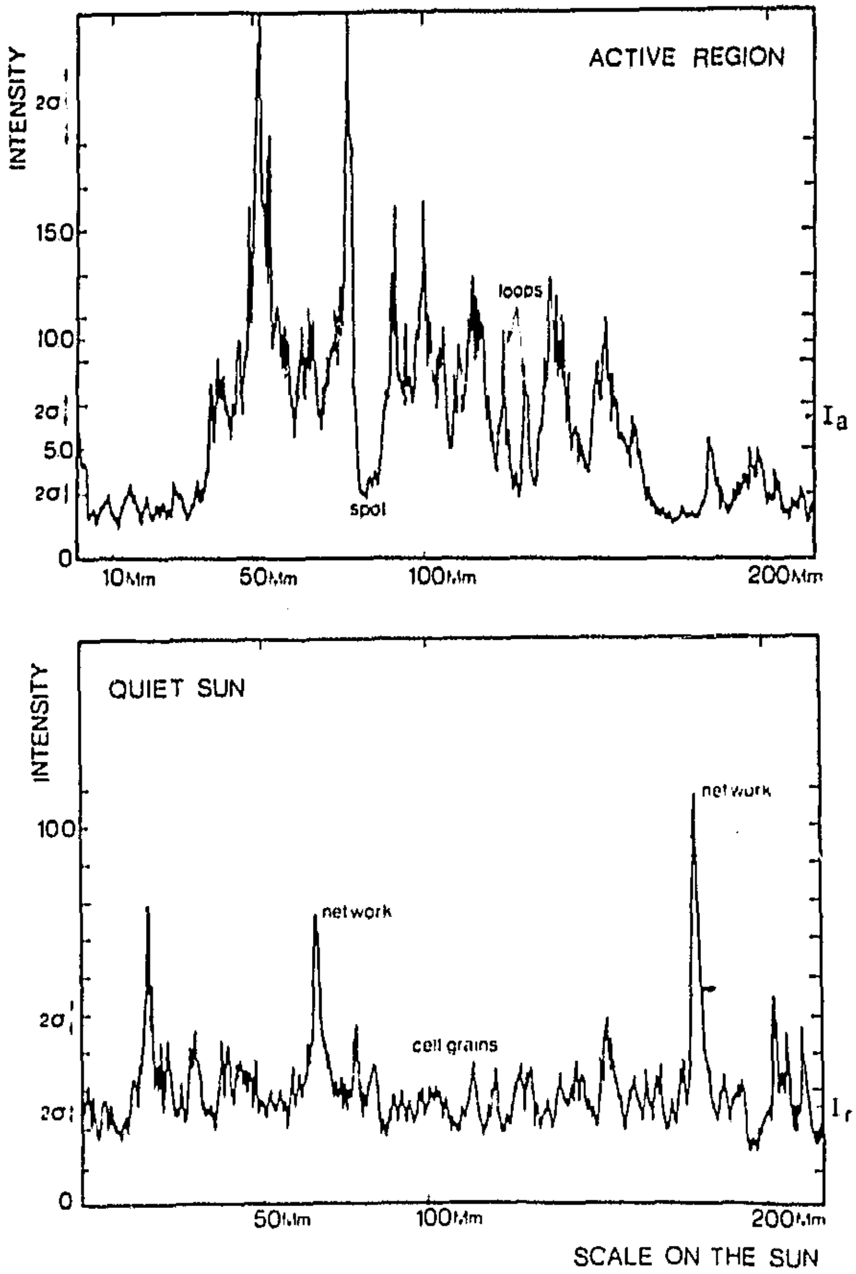

Fig. 21. — Intensity scans at 160 nm across an average quiet-Sun area and an active region. The intensity scale is in arbitrary units. The 2-sigma level due to photographic noise is indicated on the left. From Foing and Bonnet (1984).

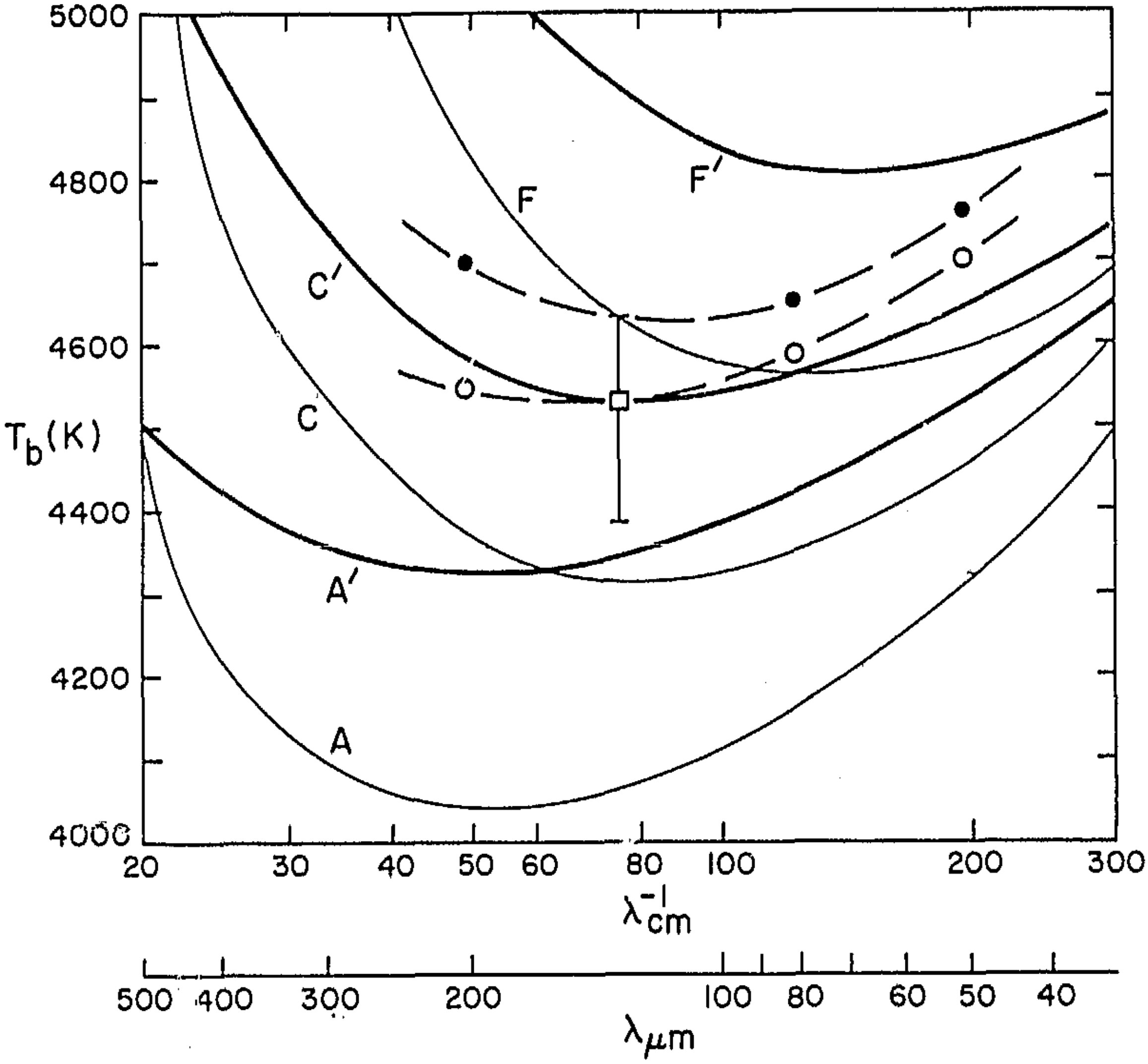

Fig. 22. — Far-infared brightness temperatures calculated from Models A′, C′, and F′ compared with the earlier model calculations, with the observed minimum value 4530(+100, -150) K at 130 μm from Rast, Kneubühl, Müller (1978), and with the observations of Degiacomi (1984) at 50, 80, and 200 μm. (Open circles represent quiet-Sun observations; filled circles represent observations with active regions included.)

V. Energy Balance

The two preceding sections have summarized how hydrostatic-equilibrium models of the chromosphere and temperature minimum region are determined from various observations. Such models should provide information about chromospheric heating.

Given the depth variation of both the number densities of the atomic and molecular energy states, and the radiation intensities in the important lines and continua, one can calculate the net radiative cooling rates Φ_{ul} and Φ_m in ergs cm^{-3} s^{-1} as functions of depth for lines between levels u and l, and for continua associated with levels m. The sum of all of these cooling rates must be the non-radiative energy input at each depth required to maintain the given temperature distribution, assuming a steady state. In radiative equilibrium without any non-radiative energy input, the sum of these cooling rates would have to be zero, but the chromosphere is clearly not in radiative equilibrium.

The net radiative cooling rate, or radiative flux divergence, for continua is given by

$$\Phi_m = 4\pi \int_m \kappa_\nu (S_\nu - J_\nu) d\nu \, , \tag{5}$$

where κ_ν is the continuous opacity (in cm^{-1}), S_ν is the source function, and J_ν is the mean intensity of radiation. For a line, equation (5) becomes

$$\Phi_{ul} = h\nu \left[n_u (A_{ul} + B_{ul} \bar{J}) - n_l B_{lu} \bar{J} \right] , \tag{6}$$

where n_u and n_l are the upper and lower level number densities, where A_{ul}, B_{ul}, and B_{lu} are the Einstein coefficients for spontaneous emission, stimulated emission, and absorption, and where $\bar{J}$ is the mean intensity weighted by the line opacity and integrated over the line according to

$$\bar{J} = \left(\int \kappa_\nu J_\nu d\nu \right) / \left(\int \kappa_\nu d\nu \right) . \tag{7}$$

Using the Model A′, C′, and F′ atmospheric parameters, the net radiative cooling rates have been calculated for 1) the lines and continua of atomic hydrogen, 2) the bound-free and free-free continua of H$^-$, 3) the resonance and subordinate lines of Ca II, 4) those lines of Mg II, and 5) the lines and continua of He, He II, Ca, Mg, Si, Si II, C, C II, Al, Fe, Na, K, and O. These five groups are called H, H$^-$, Ca II, Mg II, and "other contributions," respectively.

Figure 23, consisting of the plots shown on the following 18 pages, shows, first for Model C′ and then for Models A′ and F′, the following six plots: the

Fig. 23. (next 18 pages) — Net radiative cooling rates, first for Model C′ and then for Models A′ and F′, showing the total Φ with the five contributions to the total, followed by five plots showing the details of these contributions. (The symbol BC on the hydrogen plot refers to the Balmer continuum; the integer pairs in the Ca II and Mg II plots refer to upper and lower line indices.)

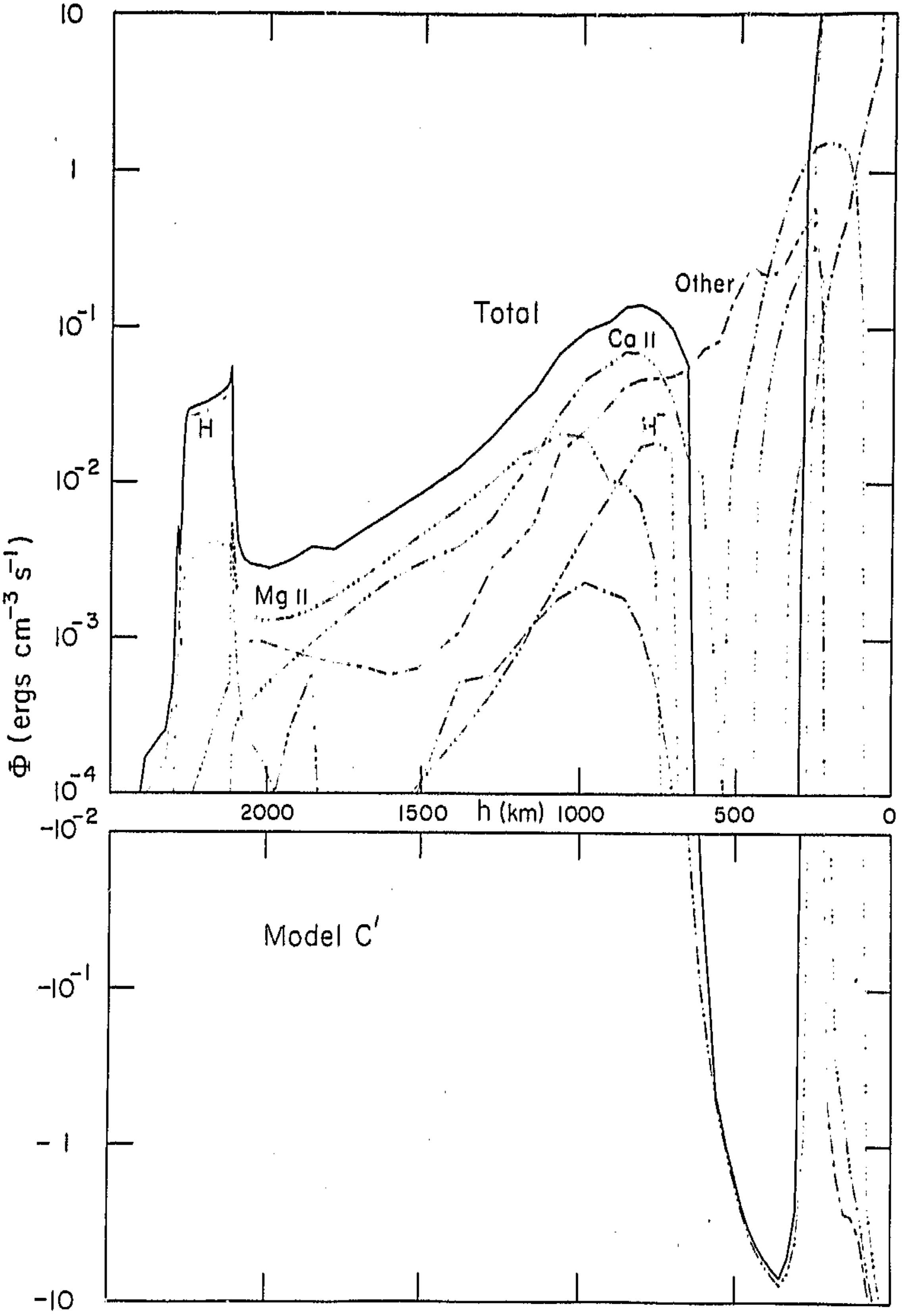10
1
10^{-1}
10^{-2}
10^{-3}
10^{-4}
-10^{-2}
-10^{-1}
-1
-10
Φ (ergs cm^{-3} s^{-1})
h (km)
2000
1500
1000
500
0
Total
Ca II
Other
H
Mg II
H^-
Model C′

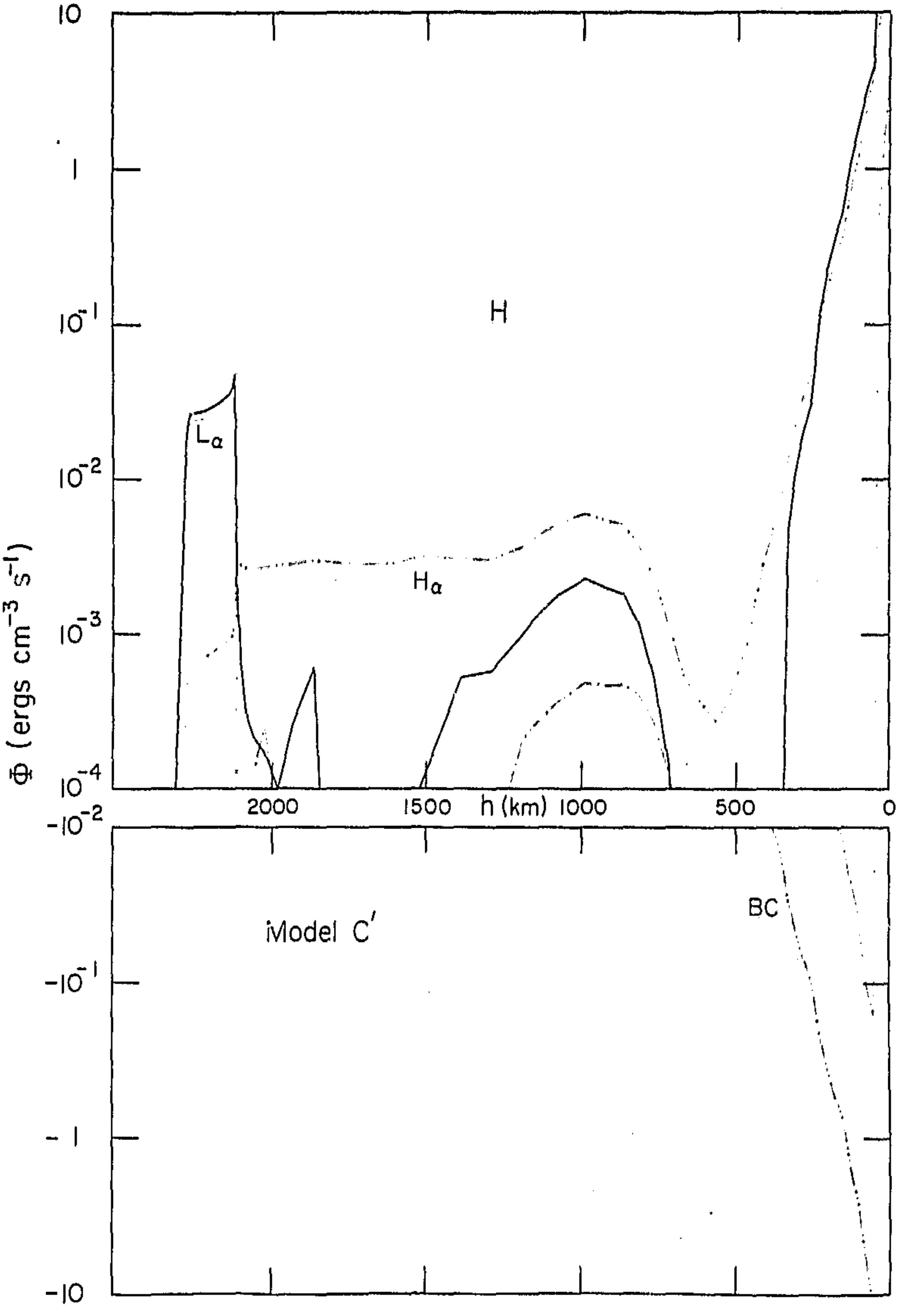
10
1
10^{-1}
10^{-2}
10^{-3}
10^{-4}
Φ (ergs cm^{-3} s^{-1})
H
L_α
H_α
2000
1500
h (km)
1000
500
0
-10^{-2}
-10^{-1}
- 1
-10
Model C'
BC

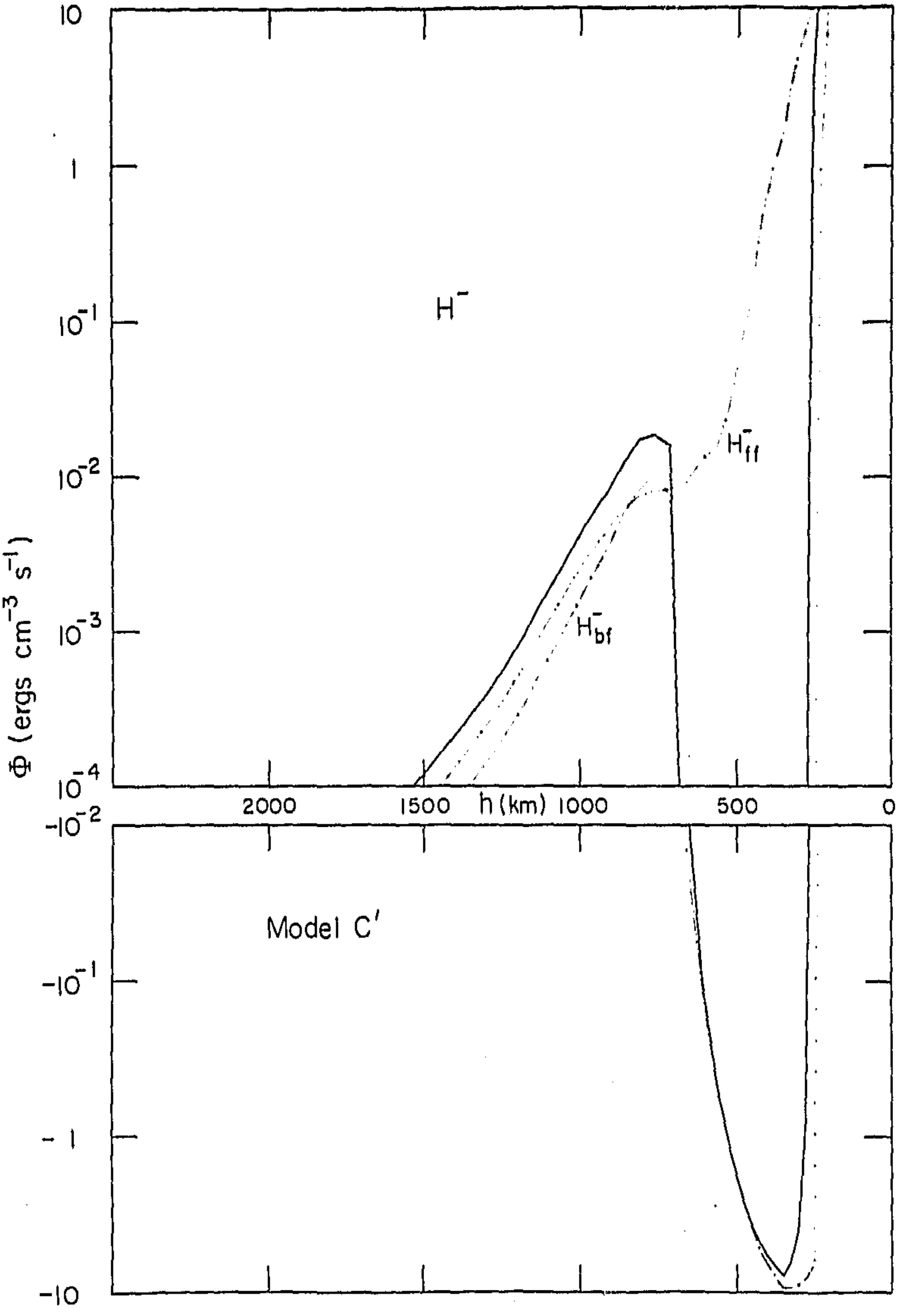

10
1
10^{-1}
10^{-2}
10^{-3}
10^{-4}
Φ (ergs cm^{-3} s^{-1})
H^-
H^-_{ff}
H^-_{bf}
2000
1500
h (km)
1000
500
0
-10^{-2}
Model C′
-10^{-1}
-1
-10

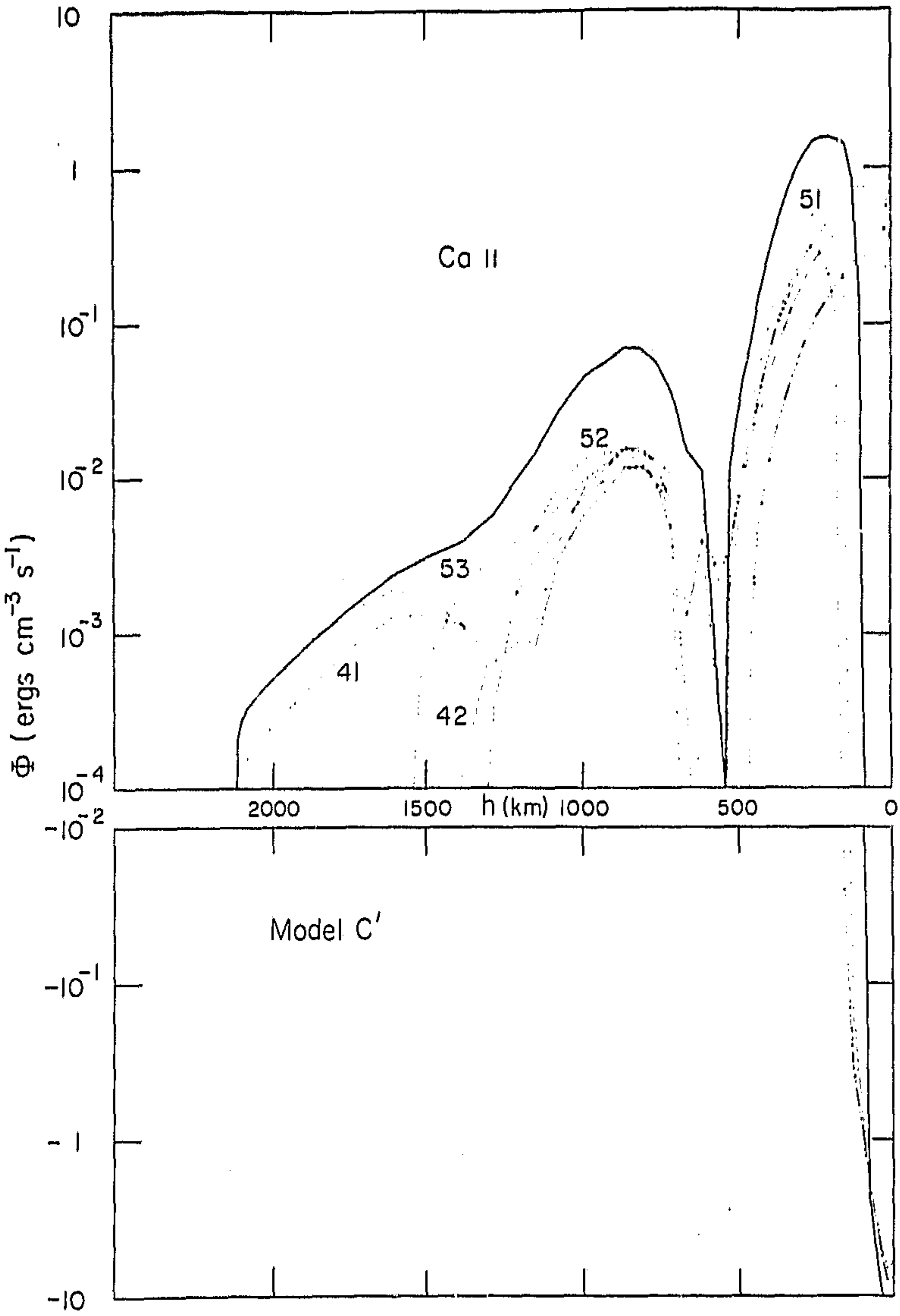
10
1
10^-1
10^-2
10^-3
10^-4
Φ (ergs cm^-3 s^-1)
Ca II
51
52
53
41
42
2000
1500
h (km)
1000
500
0
-10^-2
-10^-1
-1
-10
Model C′

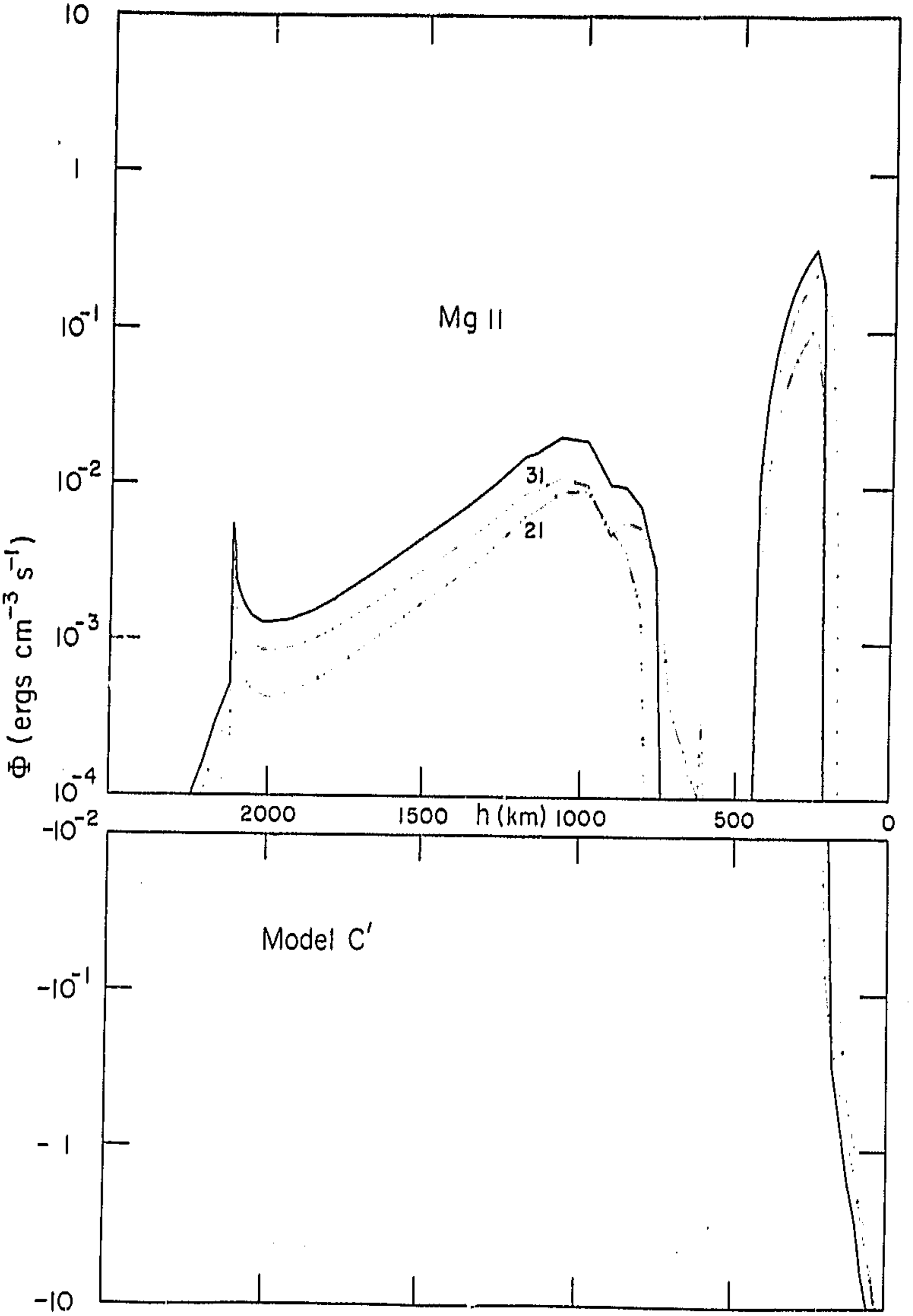
10
1
10^-1
10^-2
10^-3
10^-4
Φ (ergs cm^-3 s^-1)
Mg II
31
21
2000
1500
h (km)
1000
500
0
-10^-2
Model C′
-10^-1
- 1
-10

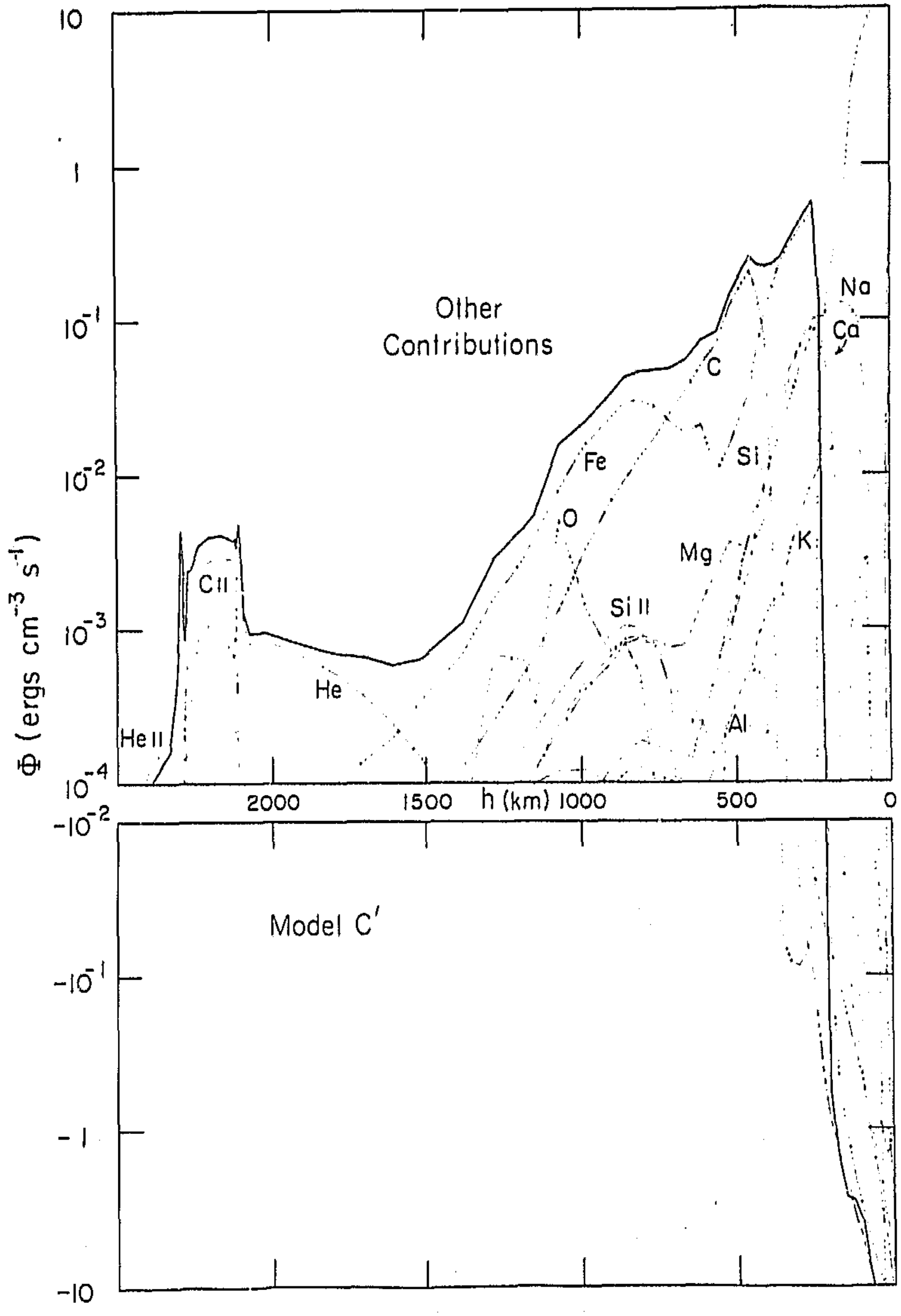
10
1
10^{-1}
10^{-2}
10^{-3}
10^{-4}
Φ (ergs cm^{-3} s^{-1})
Other Contributions
Na
Ca
C
Fe
Si
O
Mg
K
Si II
C II
He
He II
Al
2000
1500
h (km)
1000
500
0
-10^{-2}
Model C′
-10^{-1}
-1
-10

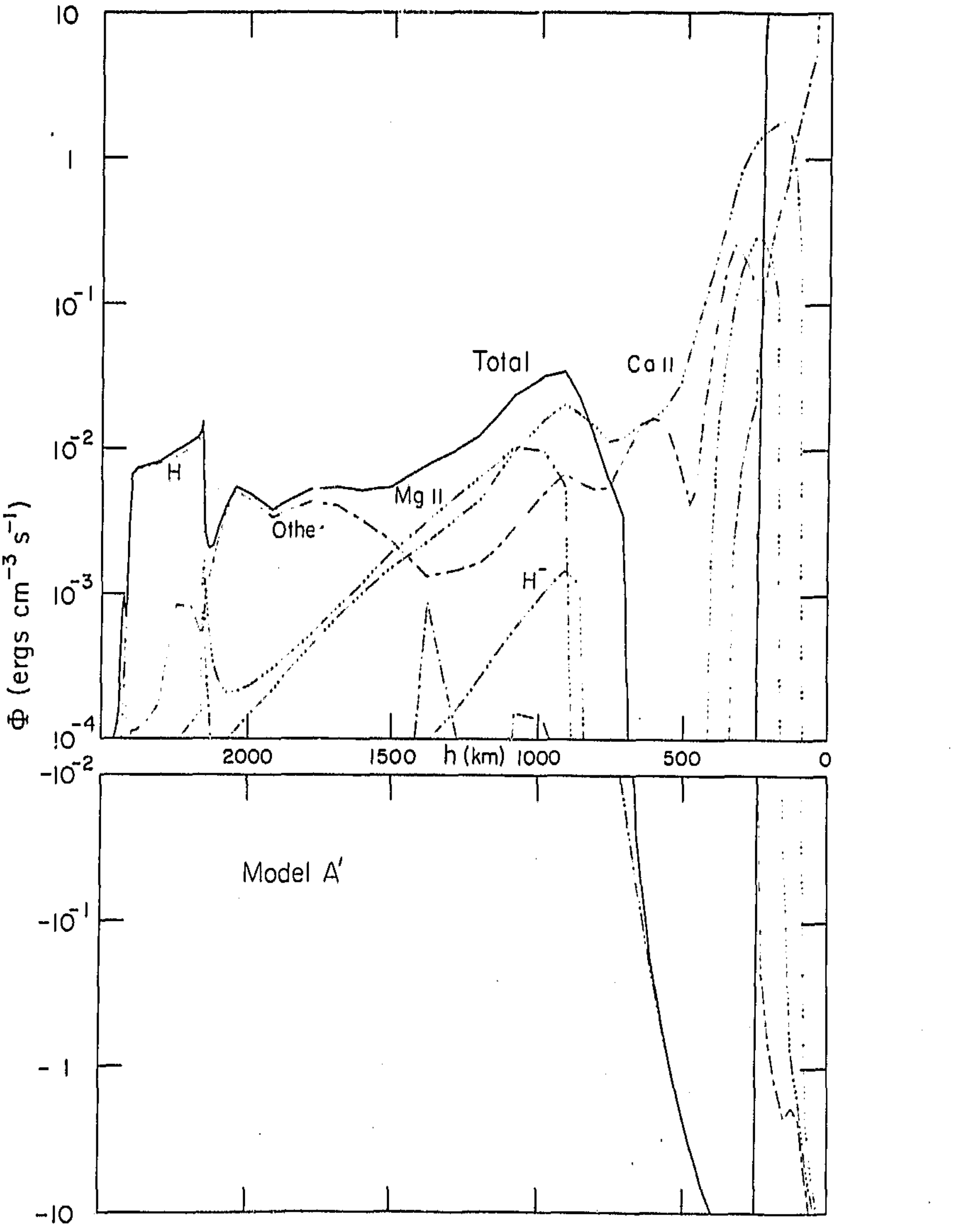

10
1
10^{-1}
10^{-2}
10^{-3}
10^{-4}
Φ (ergs cm^{-3} s^{-1})
Total
Ca II
H
Mg II
Othe·
H^{-}
2000
1500
h (km)
1000
500
0
-10^{-2}
-10^{-1}
-1
-10
Model A′

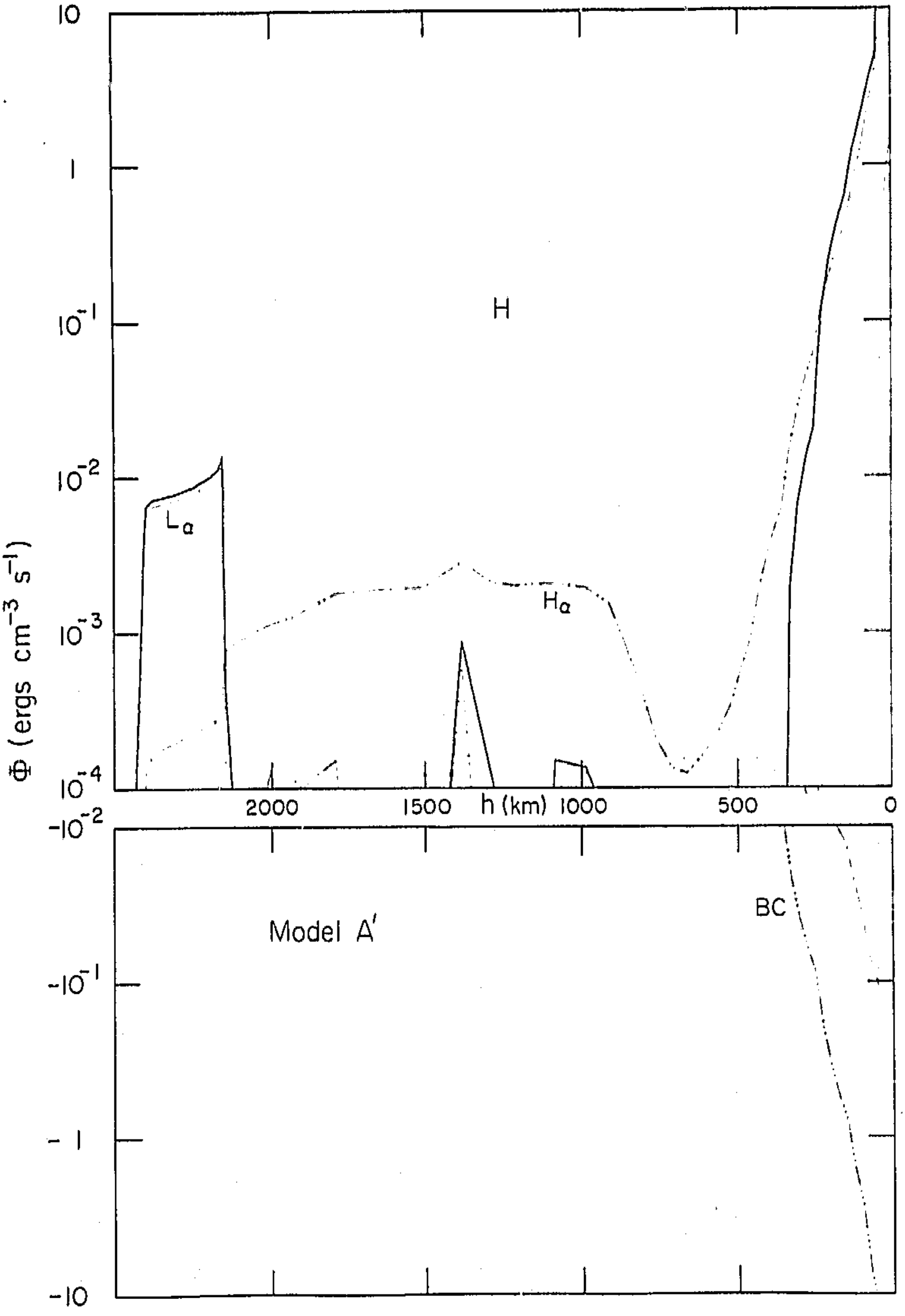
10
1
10⁻¹
10⁻²
10⁻³
10⁻⁴
Φ (ergs cm⁻³ s⁻¹)
H
Lα
Hα
2000
1500
h (km)
1000
500
0
-10⁻²
-10⁻¹
- 1
-10
BC
Model A′

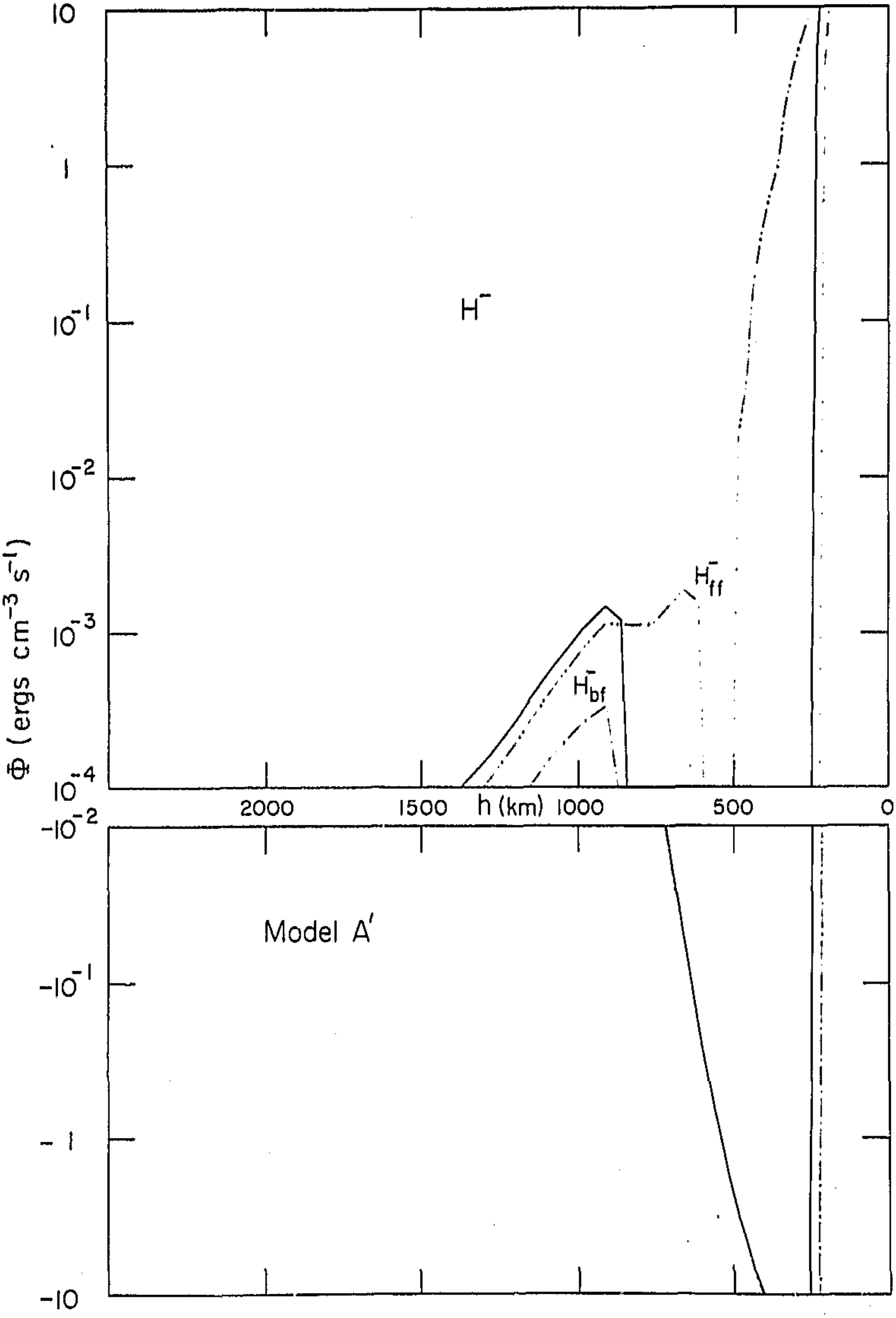

10
1
10^{-1}
10^{-2}
10^{-3}
10^{-4}
Φ (ergs cm^{-3} s^{-1})
H^-
H^-_{ff}
H^-_{bf}
2000
1500
h (km)
1000
500
0
-10^{-2}
Model A′
-10^{-1}
− 1
−10

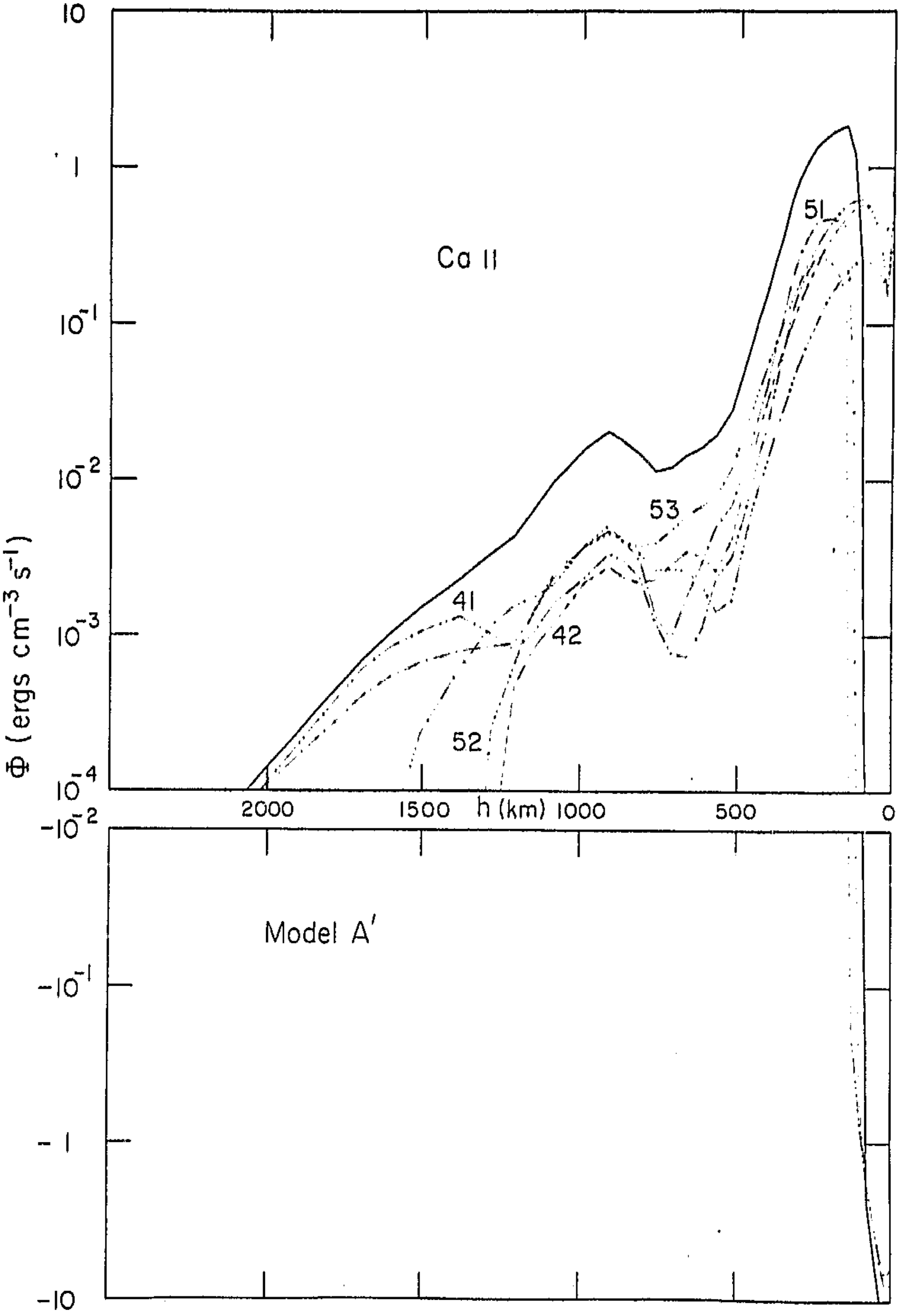
Ca II
Model A′
Φ (ergs cm^{-3} s^{-1})
h (km)
10
1
10^{-1}
10^{-2}
10^{-3}
10^{-4}
-10^{-2}
-10^{-1}
-1
-10
2000
1500
1000
500
0
41
42
51
52
53

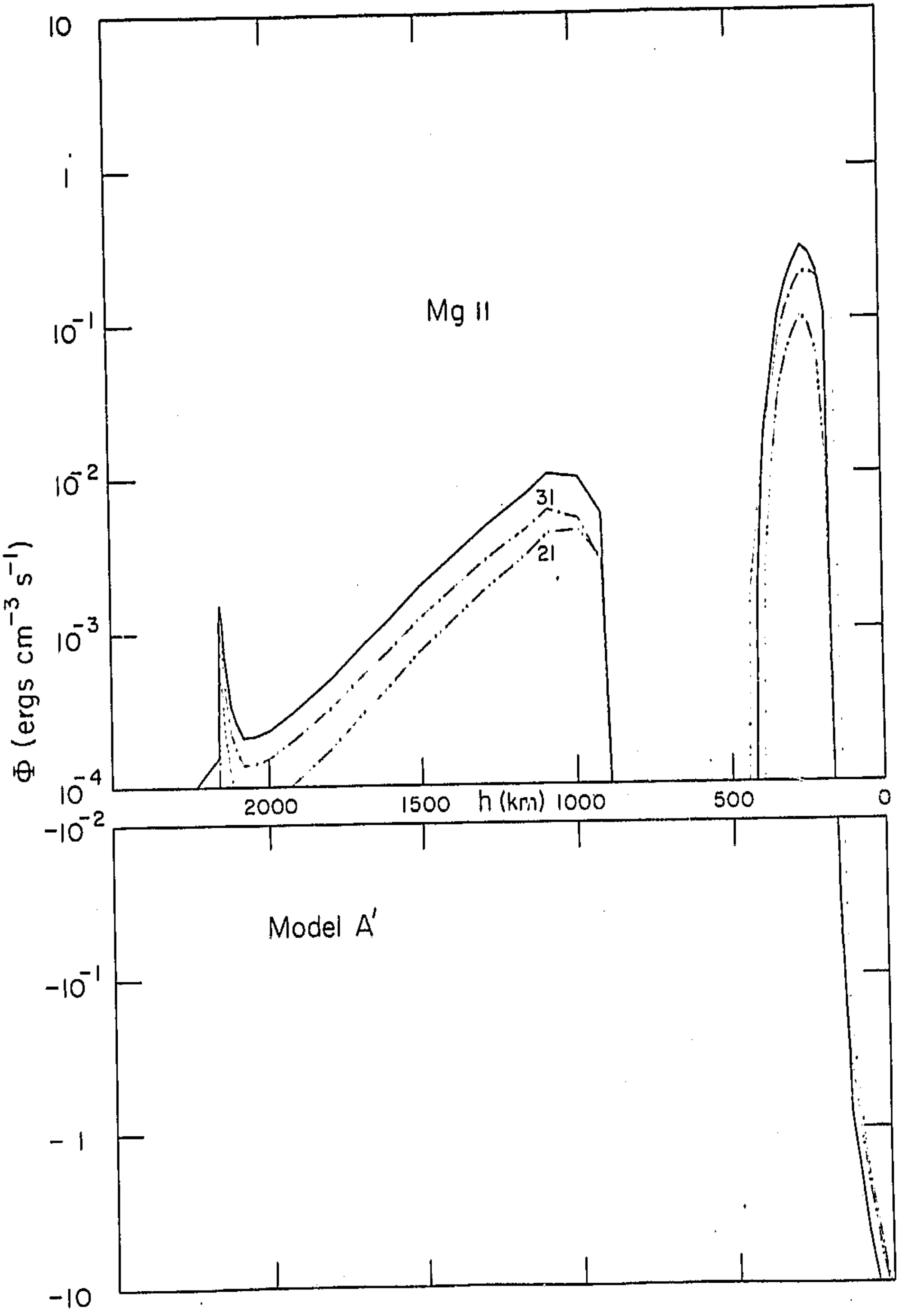
10
1
10^{-1}
10^{-2}
10^{-3}
10^{-4}
Mg II
31
21
Φ (ergs cm^{-3} s^{-1})
2000
1500
h (km)
1000
500
0
-10^{-2}
Model A′
-10^{-1}
-1
-10

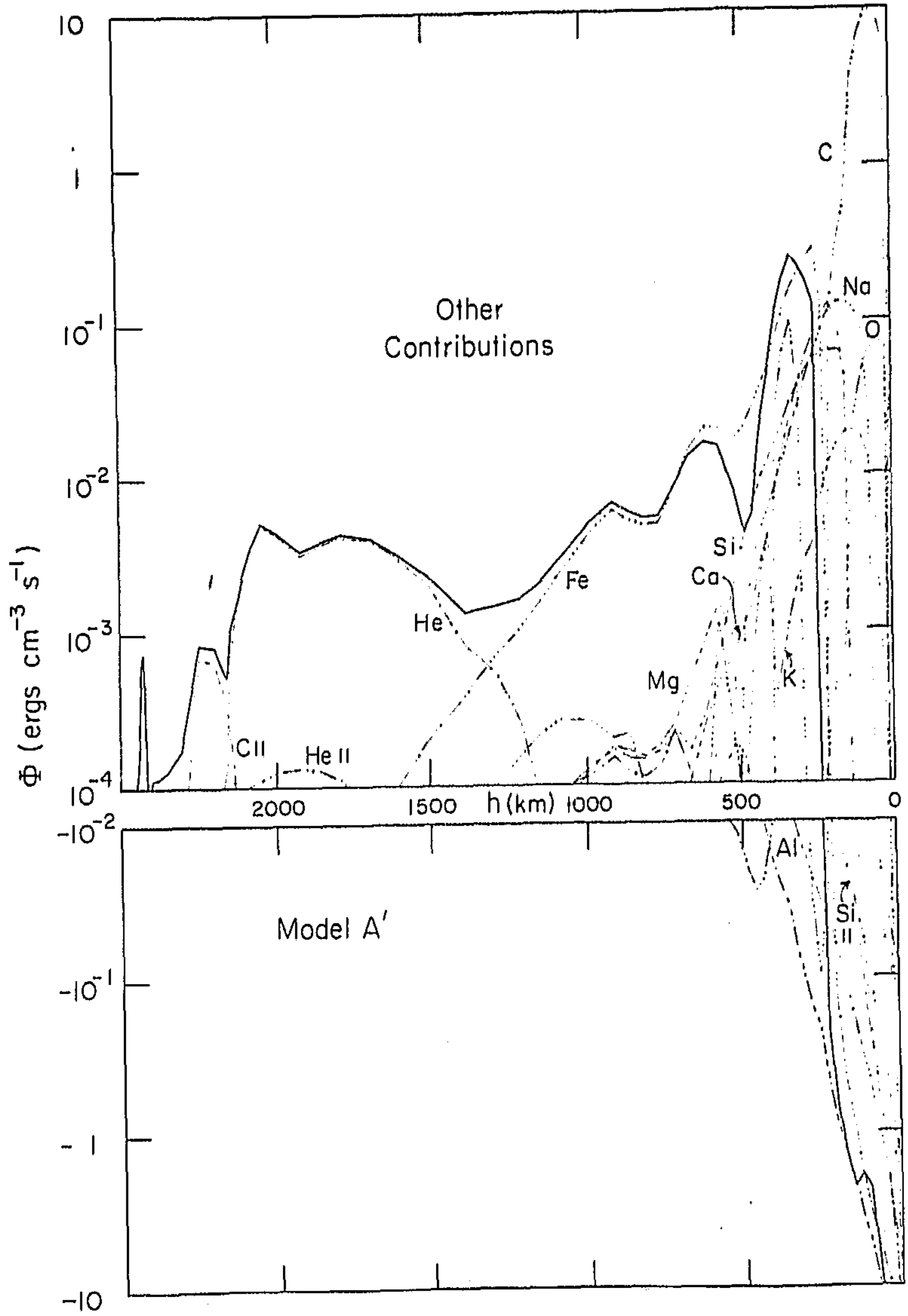
Other Contributions
Model A′
Φ (ergs cm^-3 s^-1)
h (km)
10
1
10^-1
10^-2
10^-3
10^-4
2000
1500
1000
500
0
-10^-2
-10^-1
- 1
-10
C
Na
O
Si
Ca
Fe
He
Mg
K
C II
He II
Al
Si II

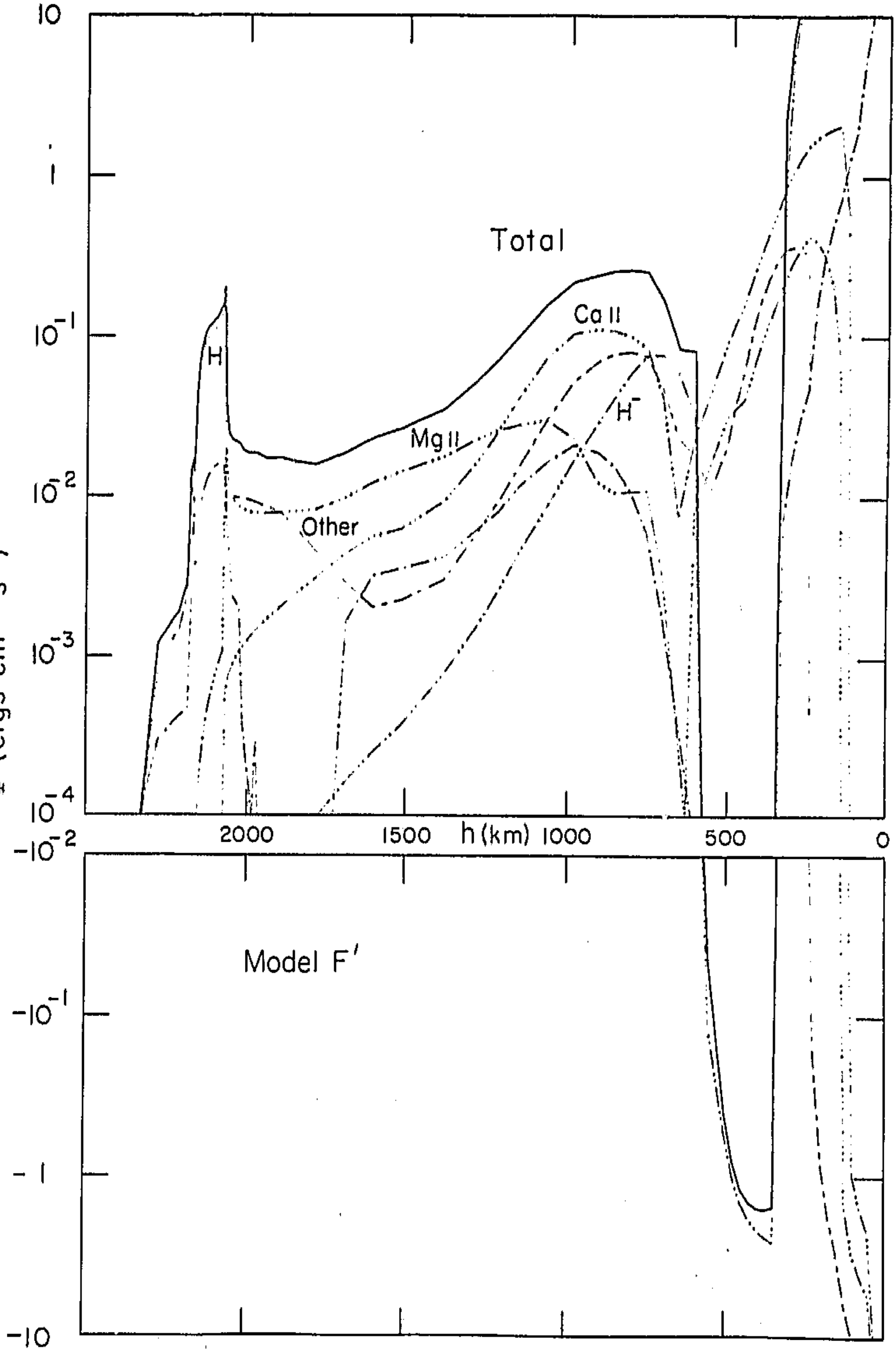
10
1
10^{-1}
10^{-2}
10^{-3}
10^{-4}
Φ (ergs cm^{-3} s^{-1})
Total
Ca II
H
H$^-$
Mg II
Other
2000
1500
h (km)
1000
500
0
-10^{-2}
Model F′
-10^{-1}
-1
-10

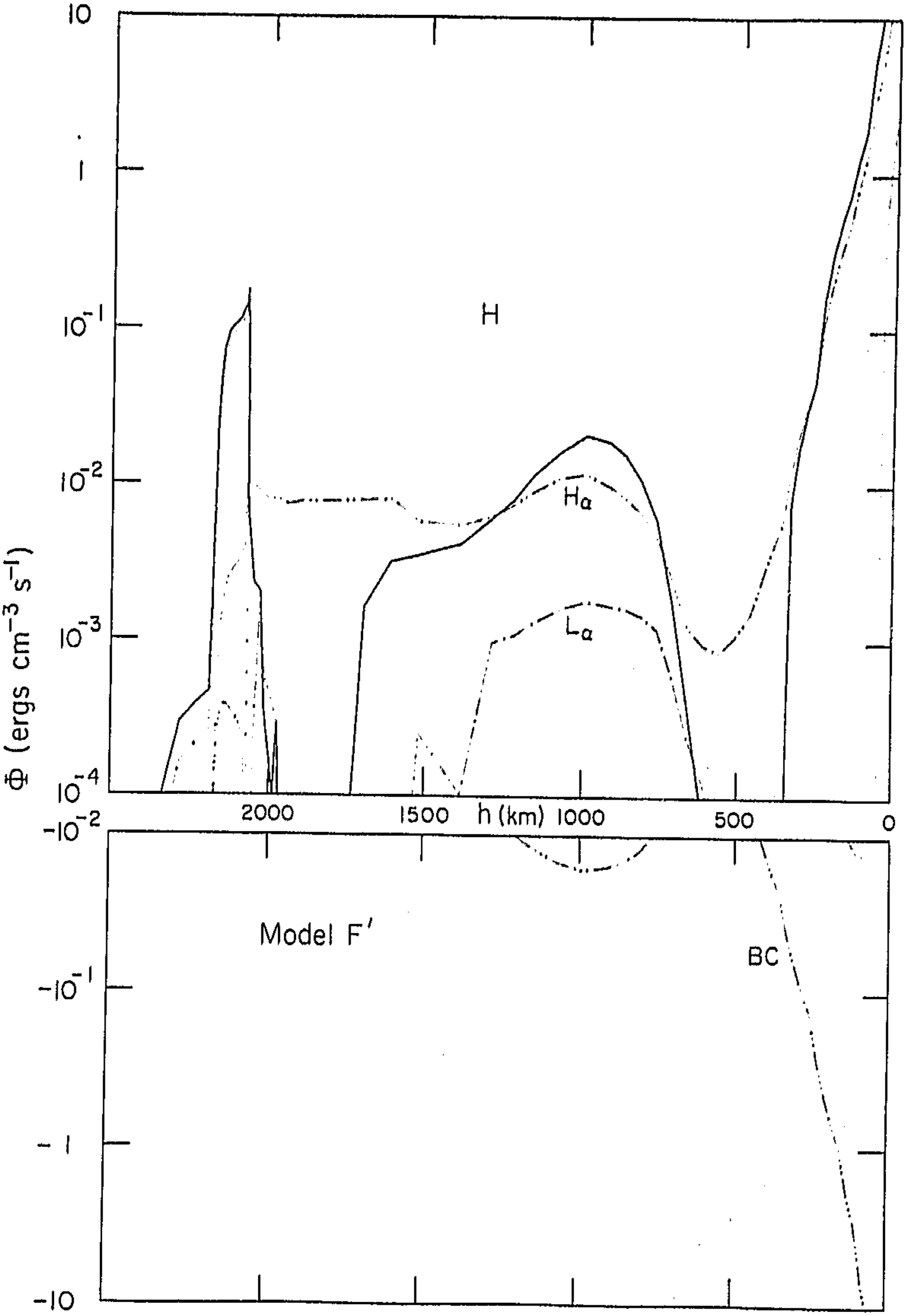
10
1
10⁻¹
10⁻²
10⁻³
10⁻⁴
H
Hα
Lα
Φ (ergs cm⁻³ s⁻¹)
2000
1500
h (km)
1000
500
0
-10⁻²
-10⁻¹
-1
-10
Model F′
BC

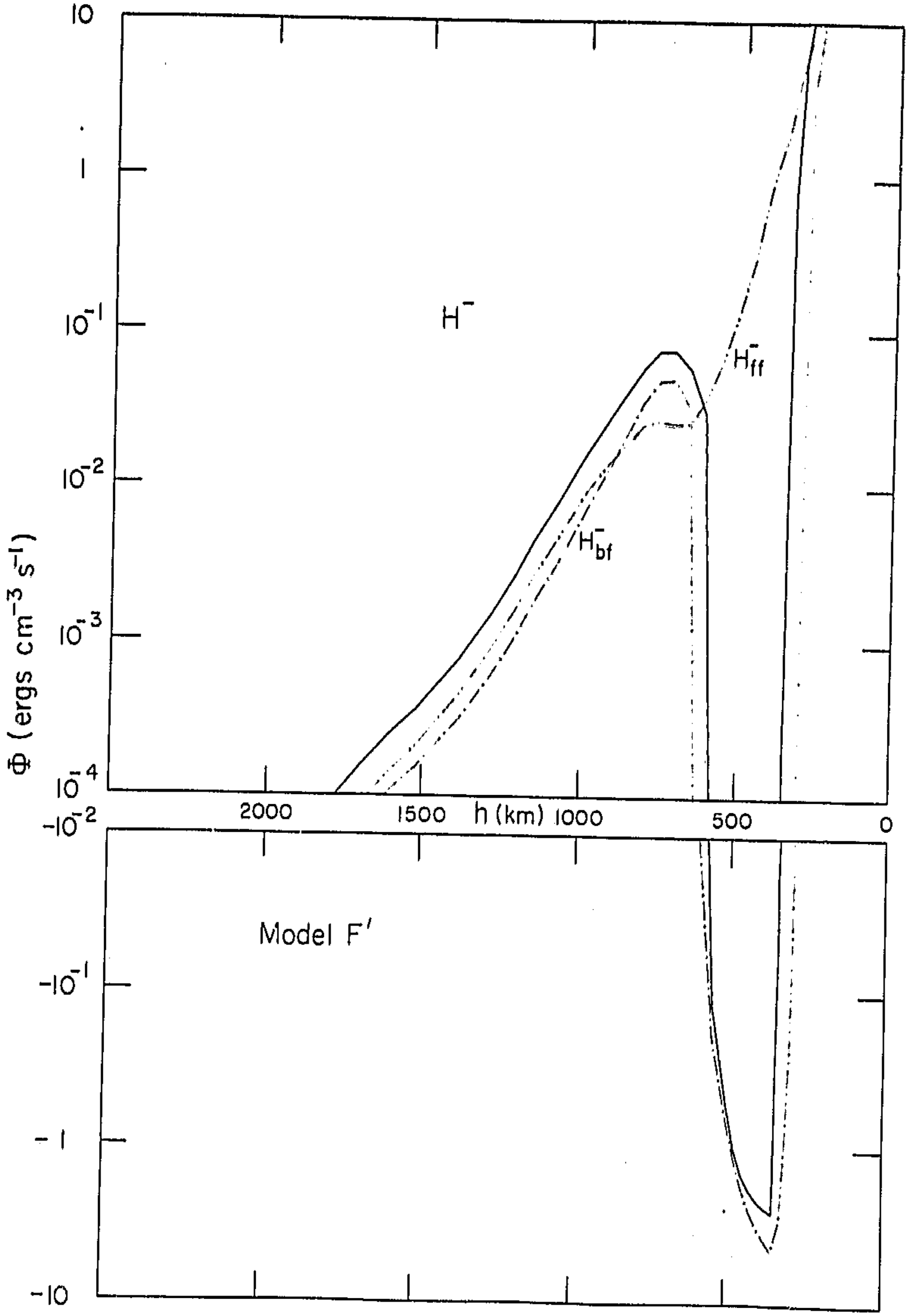10
1
10^{-1}
10^{-2}
10^{-3}
10^{-4}
Φ (ergs cm^{-3} s^{-1})
H^-
H^-_{ff}
H^-_{bf}
2000
1500
h (km)
1000
500
0
-10^{-2}
-10^{-1}
-1
-10
Model F'

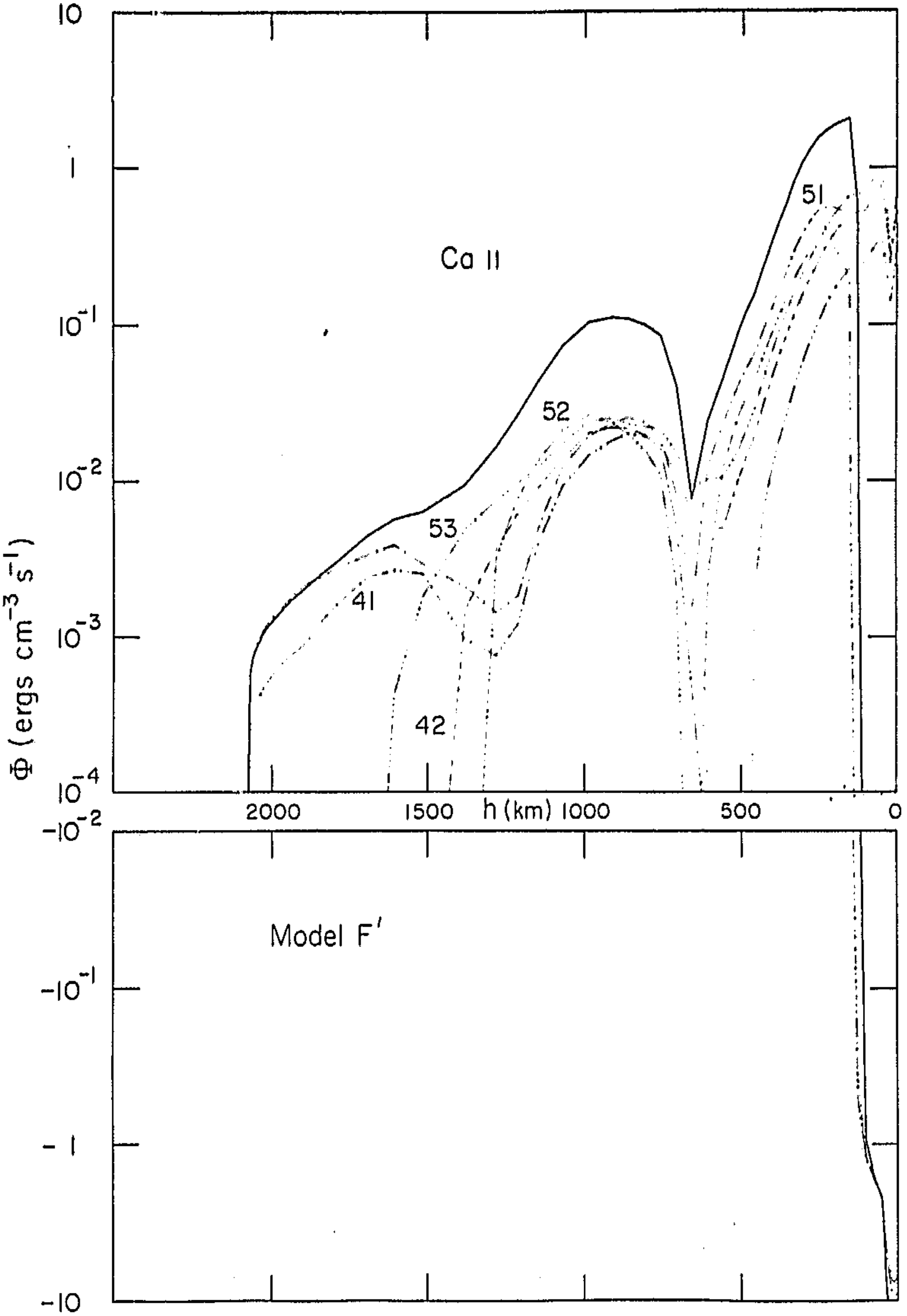
10
1
10^{-1}
10^{-2}
10^{-3}
10^{-4}
Φ (ergs cm^{-3} s^{-1})
Ca II
51
52
53
41
42
2000
1500
h (km)
1000
500
0
-10^{-2}
-10^{-1}
- 1
-10
Model F′

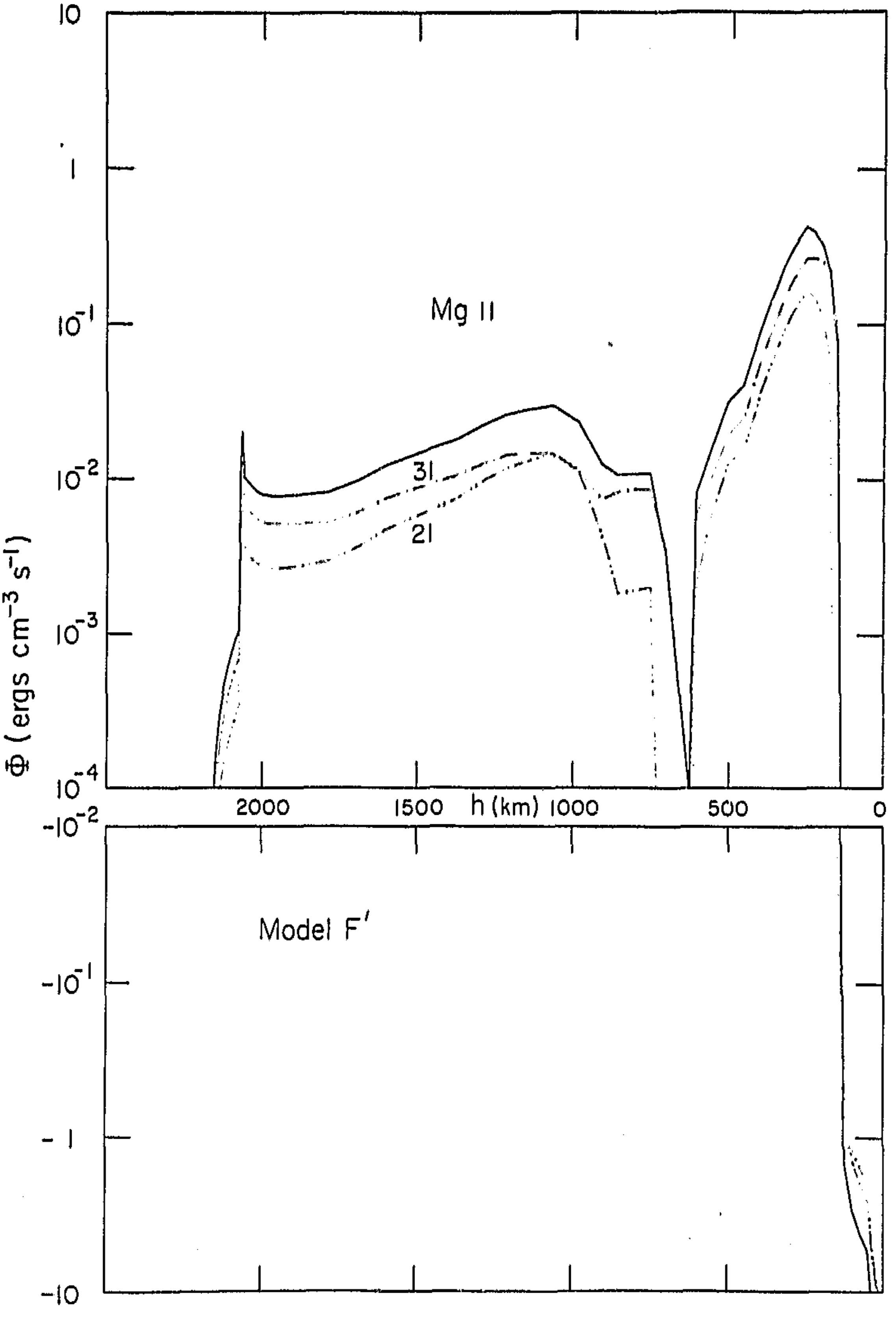
10
1
10⁻¹
10⁻²
10⁻³
10⁻⁴
Φ (ergs cm⁻³ s⁻¹)
Mg II
31
21
2000
1500
h (km)
1000
500
0
−10⁻²
−10⁻¹
− 1
−10
Model F′

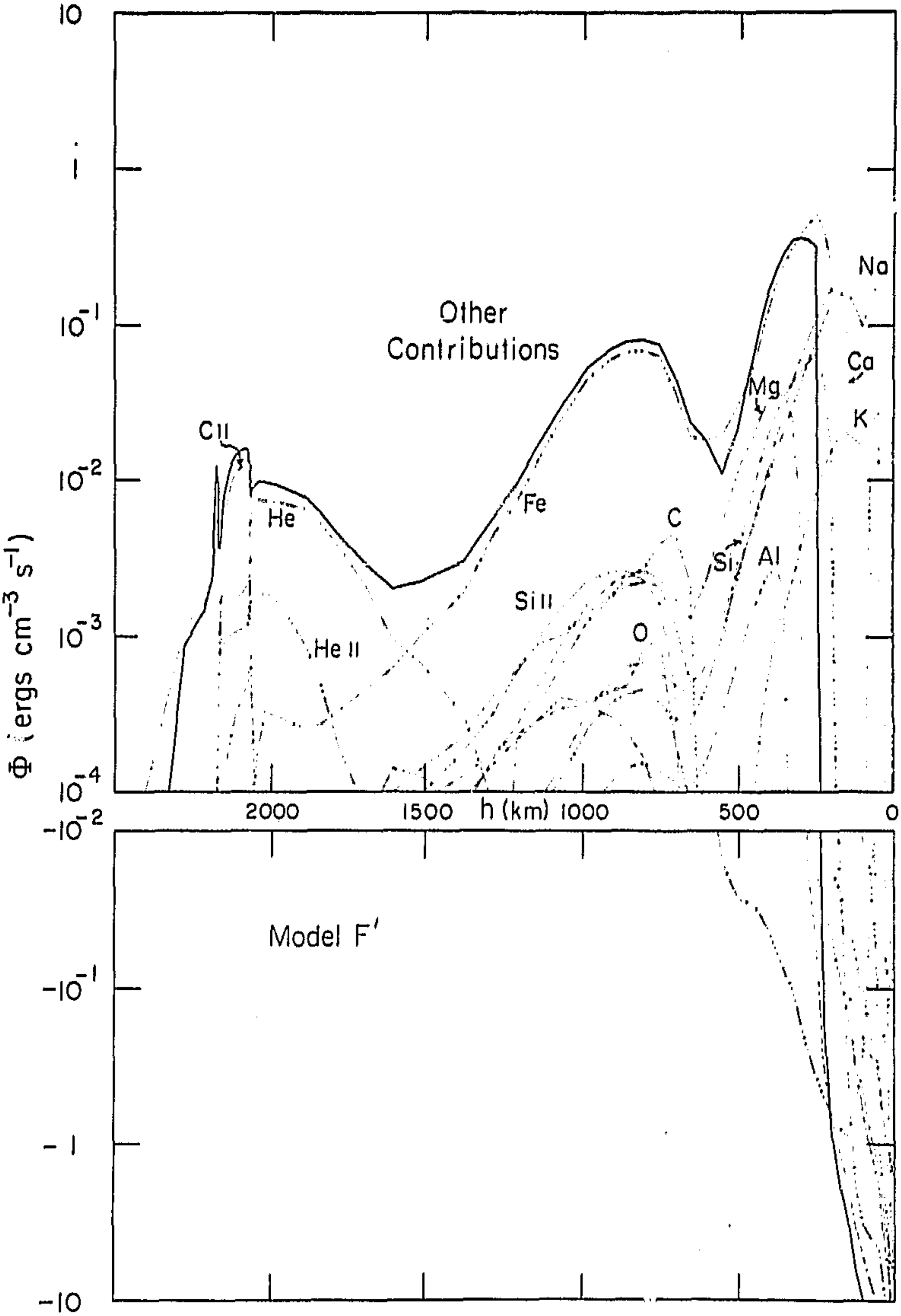
10
1
10^{-1}
10^{-2}
10^{-3}
10^{-4}
Φ (ergs cm^{-3} s^{-1})
Other Contributions
C II
He
He II
Fe
Si II
C
O
Si
Al
Mg
Na
Ca
K
2000
1500
h (km)
1000
500
0
-10^{-2}
-10^{-1}
-1
-10
Model F'

total Φ with the five contributions to the total, and then details of each of the five contributing groups. The upper and lower panels on each page show positive and negative values of Φ, on logarithmic scales, plotted against height in km above continuum optical depth unity at 500 nm.

The total rate shows three important characteristics: a) the maximum near 800 km in the low chromosphere and the gradual decrease of Φ_{Total} above this height, b) the maximum in the lower part of the chromosphere-corona transition region at temperatures between 20,000 and 30,000K, and c) the negative values of Φ_{Total} near 400 km in the temperature minimum region. (The large positive values below the temperature minimum region have less significance; they occur because Φ is proportional to the rapidly increasing number density in this region and because the photospheric temperature distribution has not been adjusted to obtain $\Phi_{Total} = 0$. In Model C′ the total hydrogen number density at 100 km is 2500 times larger than the value at 1000 km.)

The maximum of Φ_{Total} in the low chromosphere and its gradual decrease with height shows how mechanical energy is dissipated with height to maintain the chromospheric temperature rise. Theories of wave energy dissipation must be consistent with such calculated values, as discussed in the papers by Stein and others in this volume. The chromospheric mechanical energy input escapes primarily as Ca II and Mg II line emission.

The maximum of Φ_{Total} in the transition region corresponds primarily to emission in the hydrogen Lα line. The area under this maximum is $\sim 3 \times 10^5$ ergs cm^{-2} s^{-1} in the case of Model C′, which agrees with the observed integrated Lα intensity in quiet regions near the disk center. This Lα feature seems required whether there is a temperature plateau in the transition region or a more gradual temperature rise instead (or a succession of interfaces between chromospheric and coronal temperatures intersected by the line of sight). Rabin and Moore (1984) have recently proposed a localized heating mechanism to account for this required energy. Alternatively, one might suppose is that the energy 3×10^5 ergs cm^{-2} s^{-1} is dissipated in the corona and is then conducted downward to the lower transition region to be radiated away by Lα. A difficulty with such a mechanism is that the required conductive energy transport can take place only if the temperature gradient is very large (assuming classical conduction theory), while a much smaller gradient is needed in order to produce the observed emission. This difficulty may be resolved if non-Maxwellian effects are properly included, as discussed by Shoub (1982, 1983) and Owocki, Canfield, and McClymont (1985).

The negative values of Φ_{Total} in the temperature minimum region are perplexing because negatives imply non-radiative energy extraction, i.e., refrigeration. Possible explanations include 1) the effect of time-dependent wave motions that, on the average, indeed remove energy from the temperature minimum region, 2) the possible omission of positive contributions that would make the total rate positive, and 3) the need to introduce inhomogeneities that have a more extreme range of variation than components A′ through F′. These three possibilities are discussed below.

1) If waves travel through the atmosphere and the temperature at each position varies as a function of time, the time-averaged computed spectrum may have characteristics of high and low temperatures that cannot be matched by an average temperature, or by separate components such as A′ through F′. Recent calculations by Muchmore and Ulmschneider (1984) indicate that the negative values of Φ_{Total} in the temperature minimum region might be explained in this way.

2) There is a positive Φ at 400 km from the group of 13 "other contributors" He through O, but the negative Φ from H^-_{bf} at this height has an absolute value typically 10 times larger than the sum of all positive values. However, potentially important contributors not included in this group are a) prominent lines of molecules such as carbon monoxide, and b) large numbers of weak atomic and molecular lines.

To estimate these effects, Kurucz's line-opacity tables sampled at 1055 representative wavelengths between 144 nm and 10 μm have been used to compute the monochromatic flux divergence

$$\phi_\nu = 4\pi\kappa_\nu(S_\nu - J_\nu) \tag{8}$$

as a function of depth. The integral of ϕ_ν over all ν should give Φ_{Total}. This ϕ_ν is integrated from 144 nm to 10 μm, thus excluding contributions from $\lambda < 144$ nm (e.g., Lα) that affect Φ_{Total} in the middle and upper chromosphere. Also, the central features of the Ca II and Mg II resonance lines are not among the sampled wavelengths, so that Φ_{Total} computed in this way does not include the terms that are most important in the chromosphere. However, this procedure should give a valid result in the temperature minimum region. Figure 24 (for Model C′) shows Φ_{Total} obtained by integrating ϕ_ν from 144 nm to 10 μm. This figure also shows the five component integrals over the wavelengths 144-300 nm, 300 nm – 1 μm, 1 – 4.2 μm, 4.2 – 5.4 μm, and 5.4 – 10 μm. Note that Φ_{Total} is negative at 400 km, just as in Figure 23. These negative values are caused mainly by the integral from 300 nm to 1 μm, which is dominated by the H^- bound-free continuum. Positive values are found for all of the $\lambda > 1$ μm contributions, including the H^- free-free continuum. These positive and negative values can be understood from the temperature dependence of the Planck function in the two wavelength ranges. Figure 25 shows (for Model C′) the Planck function B, the continuum source function S, and the corresponding mean intensity J at 5 μm and at 500 nm plotted against height and monochromatic optical depth. At both wavelengths, J at 400 km is about 0.3 times S at $h = 0$, but $S > J$ at 5 μm while $S < J$ at 500 nm, because of the greater change of B with temperature at 500 nm. Thus ϕ_ν from equation (8) is positive at 5 μm and negative at 500 nm. The 5 μm

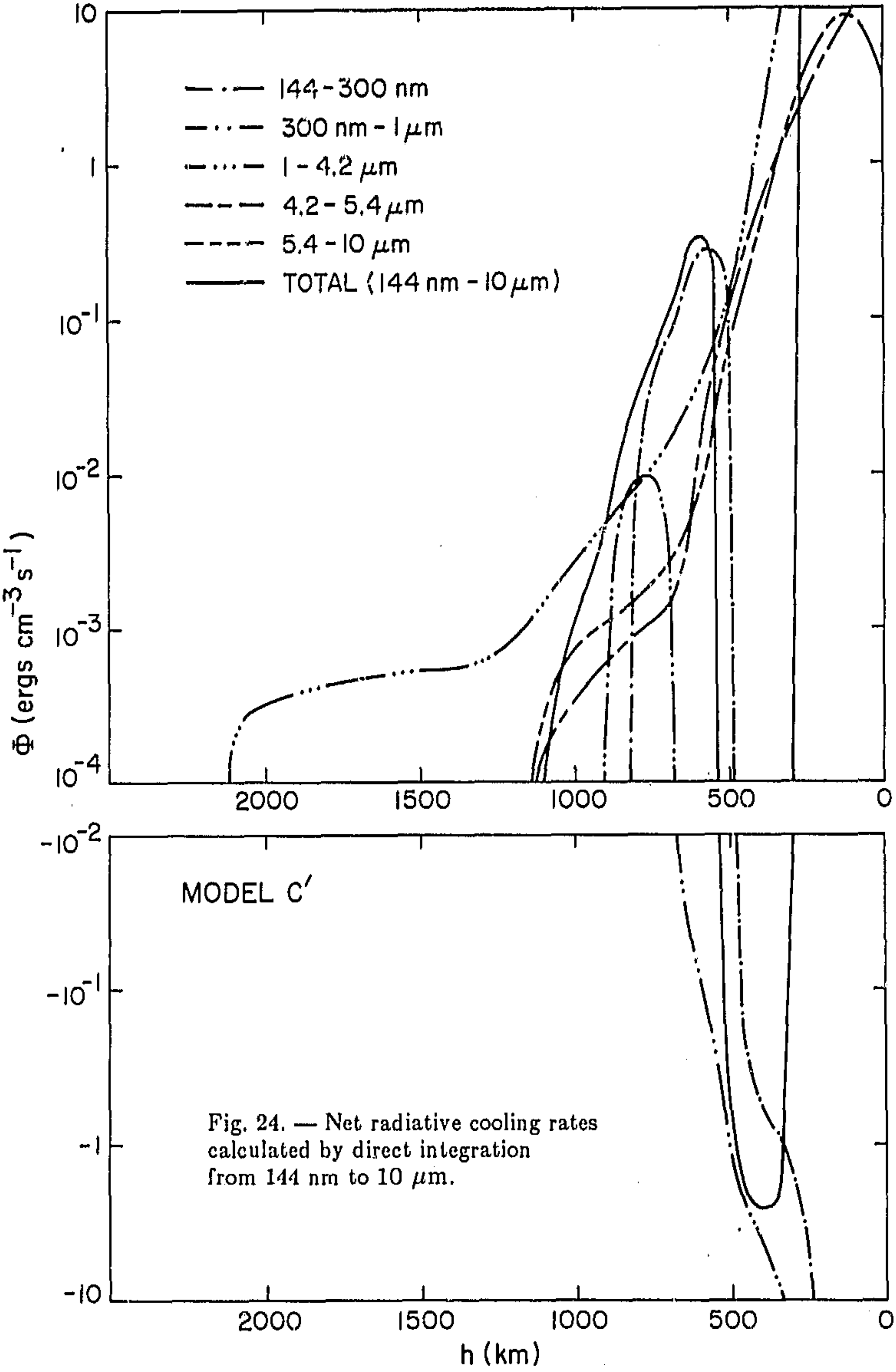

Fig. 24. — Net radiative cooling rates calculated by direct integration from 144 nm to 10 μm.

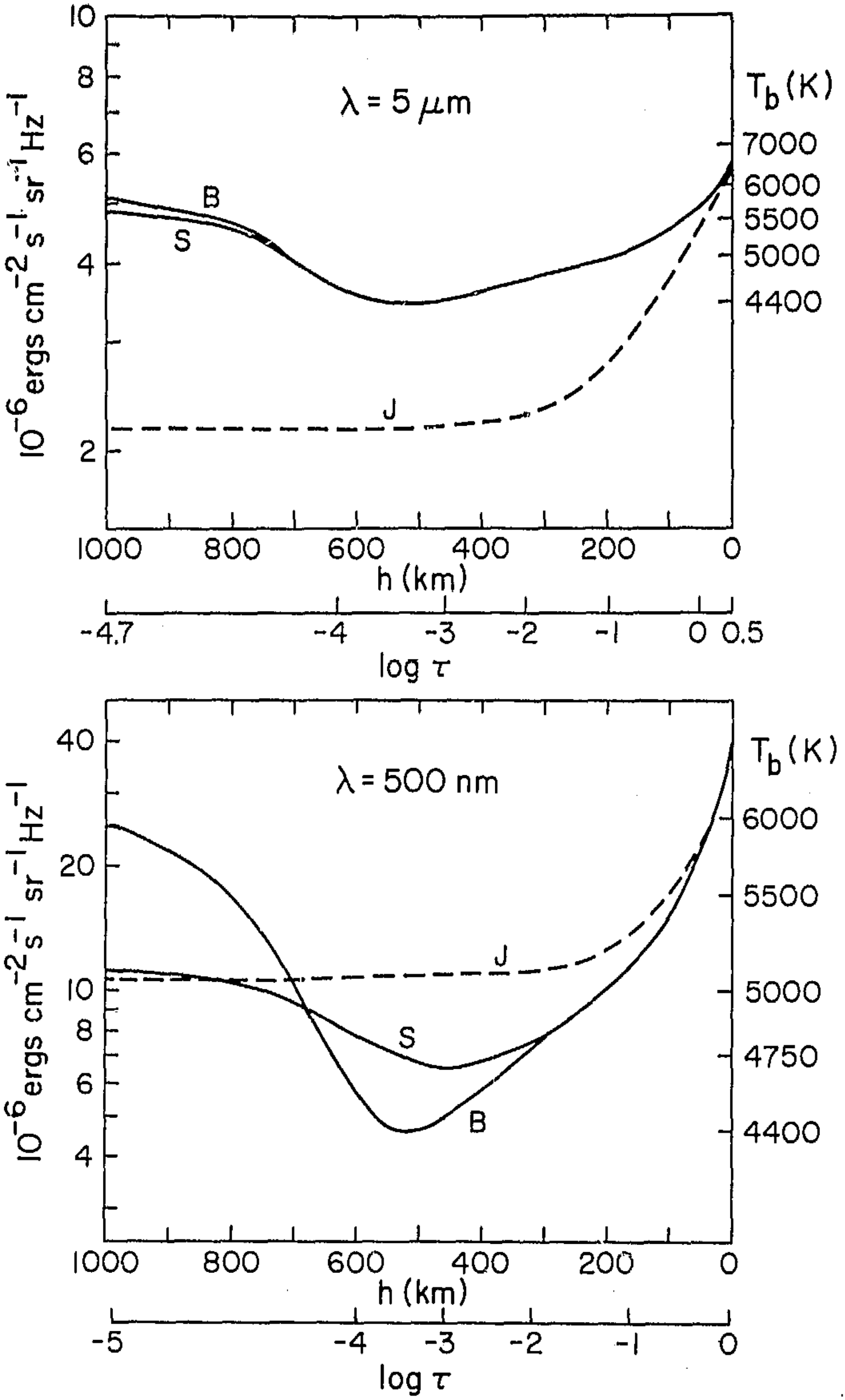

Fig. 25. — Planck function, source function, mean intensity, and optical depth at continuum wavelengths 5 μm and 500 nm.

graph shows continuum data, but the corresponding results for a strong carbon monoxide line near 5 μm are similar, except that κ in equation (8) is larger, unit optical depth occurs higher, and J is closer to S. The computed emergent intensity values in the 4.2 – 5.4 μm band are shown in Figure 26, in order to indicate that the sampled wavelengths include strong carbon monoxide lines. These calculations are intended to show that even when the CO lines and many other lines are included, the net radiative cooling rate for Model C′ remains negative in the temperature minimum region. Calculations with Models A′ and F′ lead to the same result.

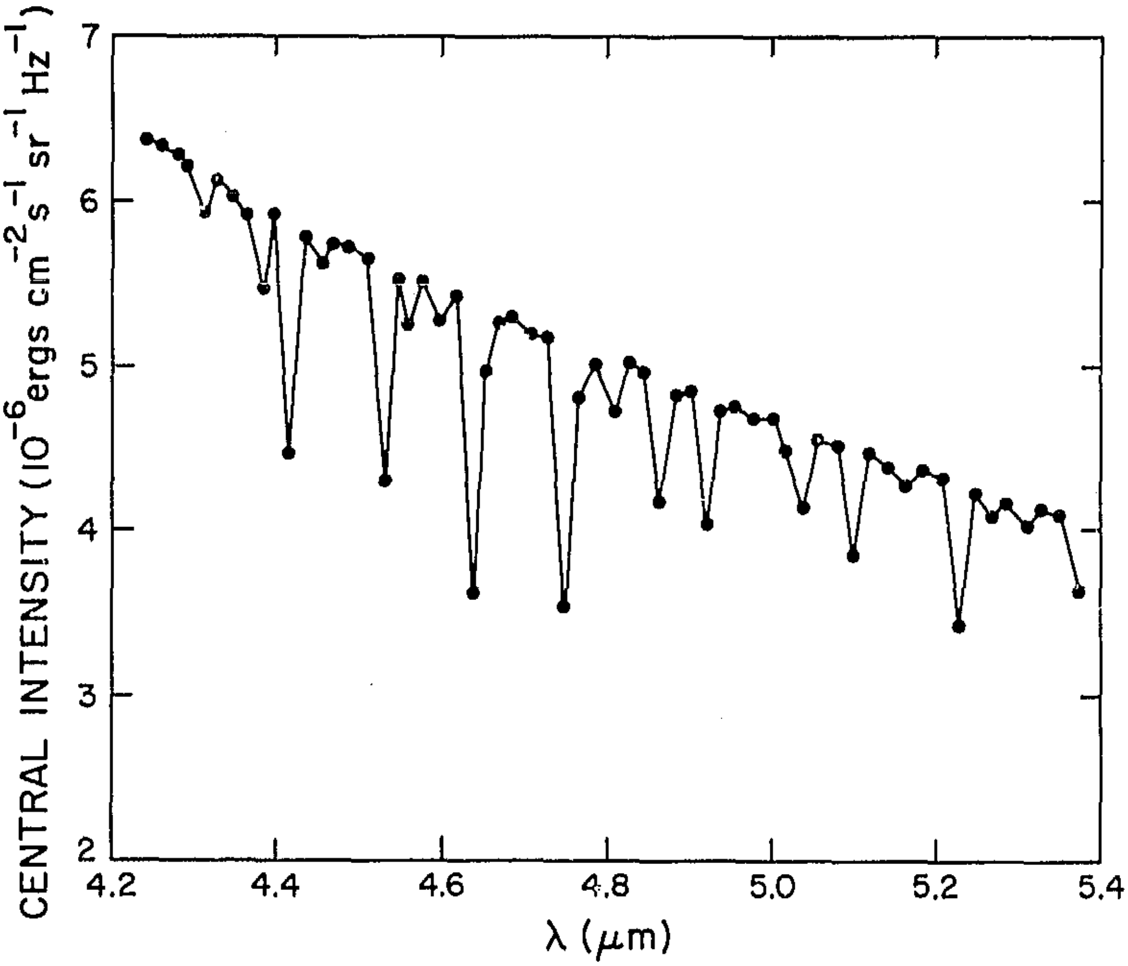

Fig. 26. — Computed intensity values in the 4.2 – 5.4 μm band, indicating the lines of

3) It may be possible to avoid the negative values of Φ_{Total} if the atmosphere consists of inhomogeneous regions having a greater temperature range than components A′ through F′. Consider a bifurcated model consisting of a) background regions having minimum temperatures well below those of Model A′, and b) bright points with minimum temperatures much higher than in Model F′. For temperatures much less than 4000K the CO lines can become strong enough to balance the negative cooling rate due to H^-_{bf}, and a radiative-equilibrium solution can be obtained with $\Phi_{Total} = 0$. For temperatures near 5000K the negatives due to H^-_{bf} are reduced in the minimum region as S approaches J, and a second radiative-equilibrium solution can be obtained. These solutions are discussed by Ayres (1981), Kneer (1983), and Muchmore and Ulmschneider (1985). Negative values of Φ_{Total} would be avoided if the atmosphere consists of these two components, each having $\Phi_{Total} = 0$. Such an explanation is supported by the observations of Ayres and Testerman (1981) who measured the fundamental vibration-rotation band of CO near 4.6 μm. They found strong CO lines with central brightness temperatures as low as 3700K near the limb. The substantial limb darkening of these lines was noted earlier by Noyes and Hall (1972). Recent observations by Deming *et al.* (1985) also provide support for a bifurcated model. They find horizontal thermal fluctuations of order ±800K in the upper photosphere.

While a bifurcated model may explain the CO and OH line observations and the values of Φ_{Total}, such a model seems inconsistent with the Ca II, far-infrared, and ultraviolet observations. The H line profiles in Figures 3 and 4 indicate that the faintest decile of the observed quiet Sun has an average minimum temperature of about 4200K, and that the brightest decile has an average minimum temperature of about 4600K. The 160 nm observations in Figure 20 show similar results. In the far infrared near 150 μm, the observed quiet-Sun minimum brightness of ~4400K means that the sum of the brightness temperatures of each fractional component weighted by its fractional area has to be ~4400K, since LTE prevails and since the intensity is proportional to temperature in this wavelength region. The 4400K average could be the result of half the area at a temperature of 5000K and half at 3800K, for example, or the result of 70% at 5000K and 30% at 3000K. On the other hand, high-resolution Ca II and 160 nm observations suggest that most of the observed quiet areas have minimum temperatures within the intermediate range 4200-4600K. Thus it seems difficult to reconcile a simple combination of high-temperature bright points and a low-temperature background with the 4400K spatial average, the observed brightness distribution of the Ca II minimum features, and the observed brightness distribution at 160 nm.

Of the three possible explanations of the negative values of Φ_{Total} discussed above, the first one also involves hot and cool fractions, which change with time and with vertical as well as horizontal position. As discussed by Muchmore and

Ulmschneider (1985), wave rarefaction can produce localized cooler regions which can be cooled further by CO radiation, while compression can produce localized hot regions. Their time-dependent solutions of the mass-, momentum-, and energy conservation equations confirm that the temperature minimum region has a bi-stable character, as discussed by Ayres (1981) and Kneer (1983).

While Ca II and 160 nm observations with sufficient spatial resolution may rule out a simple bifurcated model with temperature extremes sufficient to give $\Phi_{\mathrm{Total}} = 0$ in both components, such observations may be consistent with a dynamical interpretation, for which the temperature varies with time and with vertical position, and for which hot and cool elements can occur alternately along the line of sight.

VI. Questions and Problems

I conclude this paper with a list of unanswered questions, unsolved problems, and unfinished work, related to the particular topics discussed here.

1) Detailed chromospheric models, based on observations (and the assumption of hydrostatic equilibrium), have been given for various components of the quiet Sun. Similar detailed calculations are needed to improve the available models of active regions (Basri *et al.* 1979, Orrall 1981), coronal holes, sunspots (Avrett 1981, Lites and Skumanich 1982, Maltby *et al.* 1984), and flares (Machado *et al.* 1980, Ricchiazzi and Canfield 1983, Canfield, Gunkler, and Ricchiazzi 1984).

2) Cook, Brueckner, and Bartoe (1983) have demonstrated that the chromosphere is extended to greater heights than hydrostatic equilibrium implies, and that the active-region chromosphere extends much higher than the quiet chromosphere. What causes the scale height to be greater in active regions? How do magnetic fields affect the structure of quiet and active regions? (See Spruit 1981; Stenflo 1983.)

3) Only small portions of the available ultraviolet spectral data (such as in Figure 6) have been used to determine detailed atmospheric models. Further systematic work is needed to study the observed optically thick lines that are formed in the chromosphere and lower transition region (Lites, Shine, and Chipman 1978; Tripp, Athay, and Peterson 1978; Lemaire and Gouttebroze 1983; Roussel-Dupré 1983b). Further work also is needed to improve the theory of line formation with partial frequency redistribution. See Roussel-Dupré (1983a) and Linsky (1985).

4) The source of energy that results in Lα emission has not yet been identified. Is this energy first deposited in the corona, and then brought to the base of the transition region by non-Maxwellian effects (Shoub 1982, 1983; Owocki, Canfield, and McClymont 1985), or does some mechanism deposit the energy directly in the Lα region (Rabin and Moore 1985)?

5) Ultraviolet temperature-minimum observations made with high spatial resolution, as in Figures 20 and 21, show a brightness distribution similar to that obtained from high-resolution observations of the Ca II minimum features. Simultaneous observations of these spectra would provide useful constraints on the spatial distribution of hot and cool components of quiet and active regions.

6) In addition to disk observations in the far infrared, observations at the limb, and particularly eclipse occultations at wavelengths $\geq 150\ \mu m$, provide valuable information about the structure of the temperature minimum region and low chromosphere. See Lindsey *et al.* (1983, 1984), and Cram (1984). These far-infrared observations also show that the chromosphere is more extended than the hydrostatic equilibrium solutions indicate.

7) Regarding the negative values of the net radiative cooling rate Φ_{Total} in the temperature minimum region for Models A′ through F′, it has been suggested that higher temperatures would give a radiative equilibrium solution with $\Phi_{\mathrm{Total}} = 0$ (due to reduced $\mathrm{H}^-_{\mathrm{bf}}$ heating), and that lower temperatures would give a second $\Phi_{\mathrm{Total}} = 0$ solution (due to enhanced CO cooling). These two radiative equilibrium solutions need to be calculated accurately, including the effects of line blanketing. See Kalkofen (1985).

8) The Ca II, 160 nm, and 150 μm observations may rule out a simple bifurcated model composed of high-temperature bright points and a low-temperature background, with $\Phi_{\mathrm{Total}} = 0$ for both components. On the other hand, these observations may not rule out a dynamical model having similar properties. These ideas need further study.

I am grateful to Robert Kurucz and Rudolf Loeser for their contributions reported here, and to Bruce Lites and Robert Noyes for their comments on the manuscript. This research was supported by NASA Grant NSG-7054.

References

Avrett, E.H. 1981, Reference model atmosphere calculation: The Sunspot sunspot model, in *The Physics of Sunspots*, ed. L.E. Cram and J.H. Thomas, Sacramento Peak Obs., Sunspot, NM, 235-255.

Avrett, E.H., and Kurucz, R.L. 1983, Photospheric and sunspot models from high-resolution spectrum synthesis, Inst. Theor. Astrophys. Oslo, Report No. 59, 43-58.

Avrett, E.H., Kurucz, R.L., and Loeser, R. 1984, New models of the solar temperature minimum region and low chromosphere, *Bull. Amer. Astron. Soc.*, **16**, 450.

Ayres, T.R. 1981, Thermal bifurcation in the solar outer atmosphere, *Astrophys. J.*, **244**, 1064-1071.

Ayres, T.R., and Linsky, J.L. 1976, The Mg II *h* and *k* lines. II. Comparison with synthesized profiles and Ca II K, *Astrophys. J.*, **205**, 874-894.

Ayres, T.R., and Testerman, L. 1981, Fourier transform spectrometer observations of solar carbon monoxide. I. The fundamental and first overtone bands in the quiet Sun, *Astrophys. J.*, **245**, 1124-1140.

Basri, G.S., Linsky, J.L., Bartoe, J.-D.F., Brueckner, G., and Van Hoosier, M.E. 1979, Lyman-alpha rocket spectra and models of the quiet and active solar chromosphere based on partial redistribution diagnostics, *Astrophys. J.*, **230**, 924-949.

Brault, J., and Testerman, L. 1972, *Preliminary Kitt Peak Photoelectric Atlas*, Kitt Peak National Obs., Tucson, 623 pp.

Canfield, R.C., and Beckers, J.M. 1976, Observational evidence for unresolved motions in the solar atmosphere, in *Physique des Mouvements dans les Atmosphères Stellaires*, ed. R. Cayrel and M. Steinberg (Colloques Internationaux du CNRS No. 250), 291-330.

Canfield, R.C., Gunkler, T.A., and Ricchiazzi, P.J. 1984, The Hα spectral signatures of solar flares, nonthermal electrons, conductive flux, and coronal pressure, *Astrophys. J.*, **282**, 296-307.

Cook, J.W., Brueckner, G.E., and Bartoe, J.-D.F. 1983, High resolution telescope and spectrograph observations of solar fine structure in the 1600Å region, *Astrophys. J.*, **270**, L89-L93.

Cram, L.E. 1985, Interpretation of millimetre and sub-millimetre observations of the solar chromosphere, *Internat. J. Infrared Millimeter Waves*, in press.

Cram, L.E., and Damé, L. 1983, High spatial and temporal resolution observations of the solar Ca II H line, *Astrophys. J.*, **272**, 355-361.

Cuny, Y. 1971, Interpretation of the solar continuum from 1680 to 600Å. Model of the transition region photosphere-chromosphere and of the chromosphere, *Solar Phys.*, **16**, 293-313.

Degiacomi, C.G. 1984, *Far-Infrared Solar Imaging from a Balloon-Borne Platform*, Ph.D. Thesis, Swiss Federal Institute of Technology, Zurich (ETH Diss. No. 7665).

Degiacomi, K., Kneubühl, F.K. Huguenin, D., and Müller, E.A. 1984, Far-infrared solar imaging from a balloon-borne platform, *Internat. J. Infrared Millimeter Waves*, **5**, 643-653.

Deming, D., Hillman, J.J., Kostiuk, T., Mumma, M.J., and Zipoy, D.M. 1985, Thermal bifurcation in the upper solar photosphere inferred from heterodyne spectroscopy of OH rotational lines, *Solar Phys.*, in press.

Foing, B., and Bonnet, R.M. 1984, On the origin of the discrete character of the solar disk brightness in the 160 nanometer continuum, *Astrophys. J.*, **279**, 848-856.

Gingerich, O., Noyes, R.W., Kalkofen, W., and Cuny, Y. 1971, The

Harvard-Smithsonian reference atmosphere, *Solar Phys.*, **18**, 347-365.

Holweger, H., and Müller, E.A. 1974, The photospheric barium spectrum: Solar abundance and collision broadening of Ba II lines by hydrogen, *Solar Phys.*, **39**, 19-30.

Kalkofen, W. 1985, Ayres' bifurcated solar model, this volume.

Kneer, F. 1983, A possible explanation of the Wilson-Bappu relation and the chromospheric temperature rise in late-type stars, *Astron. Astrophys.*, **128**, 311-317.

Kohl, J.L., Parkinson, W.H., and Reeves, E.M. 1975, private communication (observed data listed in VAL-III).

Kurucz, R.L., and Avrett, E.H. 1981, *Solar Spectrum Synthesis. I. A Sample Atlas from 224 to 300 nm*, Smithsonian Astrophys. Obs. Special Rept. 391, 139 pp.

Kurucz, R.L., Furenlid, I., Brault, J., and Testerman, L. 1984, *Solar Flux Atlas from 296 to 1300 nm*, National Solar Observatory, Sunspot, NM, 240 pp.

Lemaire, P., and Gouttebroze, P. 1983, Magnesium II line formation: The contribution of high atomic levels to the resonance lines, *Astron. Astrophys.*, **125**, 241-245.

Lindsey, C., Becklin, E.E., Jefferies, J.T., Orrall, F.Q., Werner, M.W., and Gatley, I. 1983, Submillimeter extensions of the solar limb determined from observations of the total eclipse of 1982 July 31, *Astrophys. J.*, **264**, L25-L30.

Lindsey, C., Becklin, E.E., Jefferies, J.T., Orrall, F.Q., Werner, M.W., and Gatley, I. 1984, Observations of the brightness profile of the Sun in the 30-200 micron continuum, *Astrophys. J.*, **281**, 862-869.

Linsky, J.L. 1985, Observed and computed stellar line profiles: The roles played by partial redistribution, geometrical extent, and expansion, in *Progress in Stellar Spectral Line Formation Theory*, ed. J. Beckman and L. Crivellari, Trieste, in press.

Lites, B.W., Shine, R.A., and Chipman, E.G. 1978, Line formation in the solar chromosphere. I. The C II resonance lines observed with OSO 8, *Astrophys. J.*, **222**, 333-341.

Lites, B.W., and Skumanich, A. 1982, A model of a sunspot chromosphere based on OSO 8 observations, *Astrophys. J. Suppl.*, **49**, 293-316.

Machado, M.E., Avrett, E.H., Vernazza, J.E., and Noyes, R.W. 1980, Semiempirical models of chromospheric flare regions, *Astrophys. J.*, **242**, 336-351.

Maltby, P., Albregtsen, F, Kjeldseth-Moe, O., Kurucz, R., and Avrett, E. 1984, Solar cycle temperature variations in sunspots, in *Cool Stars, Stellar Systems, and the Sun*, ed. S.L. Baliunas and L. Hartmann (New York: Springer-Verlag), 176-179.

Muchmore, D., and Ulmschneider, P. 1985, Effects of CO molecules on the outer solar atmosphere: A time-dependent approach, *Astron. Astrophys.*, in press.

Noyes, R.W., and Hall, D.N.B. 1972, Thermal oscillations in the high solar photosphere, *Astrophys. J.*, **176**, L89-L92.

Orrall, F.Q. ed. 1981, *Solar Active Regions. A Monograph from Skylab Workshop III*, (Boulder: Colorado Associated Univ. Press), 350 pp.

Owocki, S.P., Canfield, R.C., and McClymont, A.N. 1985, The role of non-classical transport in the formation of the Lyα temperature plateau, *Bull. Amer. Astron. Soc.*, in press.

Pasachoff, J.M. 1971, Absolute intensity calibration of solar K-line profiles, *Solar Phys.*, **19**, 323-329.

Rabin, D., and Moore, R.L. 1984, Heating the Sun's lower transition region with fine-scale electric currents, *Astrophys. J.*, **285**, 359-367.

Rast, J., Kneubühl, F.K., and Müller, E.A. 1978, Measurement of the solar brightness temperature near its minimum with a balloon-borne lamellar-grating interferometer, *Astron. Astrophys.*, 68, 229-238.

Ricchiazzi, P.J., and Canfield, R.C. 1983, A static model of chromospheric heating in solar flares, *Astrophys. J.*, 272, 739-755.

Roussel-Dupré, D. 1983a, H I Lyman-alpha in the Sun: The effects of partial redistribution in the line wings, *Astrophys. J.*, 272, 723-738.

Roussel-Dupré, D. 1983b, Skylab observations of the solar C I multiplets at λ1560 and λ1657, *Astrophys. J.*, 275, 892-900.

Rutten, R.J., and Milkey, R.W. 1979, Partial redistribution in the solar photospheric Ba II spectrum, *Astrophys. J.*, 231, 277-283.

Samain, D. 1978, *Recherches sur l'émission continue de la photosphère et de la zone de transition photosphère-chromosphère du soleil entre 1400Å et 2100Å*, Ph.D. Thesis, University of Paris, 198 pp.

Samain, D. 1980, Solar ultraviolet continuum radiation: The photosphere, the low chromosphere, and the temperature-minimum region *Astrophys. J. Suppl*, 44, 273-294.

Shoub, E.C. 1982, Invalidity of local thermodynamic equilibrium for electrons in the solar transition region. II. Analysis of a linear BGK model, Stanford Univ. Inst. Plasma Res. Rept. No. 946.

Shoub, E.C. 1983, Invalidity of local thermodynamic equilibrium for electrons in the solar transition region. I. Fokker-Planck results, *Astrophys. J.*, 266, 339-369.

Spruit, H.C. 1981, Magnetic flux tubes, in *The Sun as a Star*, ed. S. Jordan, NASA SP-450, 385-412.

Stenflo, J.O. ed. 1983, *Solar and Stellar Magnetic Fields: Origins and Coronal Effects*, (Boston: Reidel), 564 pp.

Tripp, D.A., Athay, R.G., and Peterson, V.L. 1978, Spectrum synthesis of chromospheric lines of Si II and Si III, *Astrophys. J.*, 220, 314-324.

Vernazza, J.E., Avrett, E.H., and Loeser, R. 1976, Structure of the solar chromosphere II. The underlying photosphere and temperature-minimum region, *Astrophys. J. Suppl.*, 30, 1-60 (VAL-II).

Vernazza, J.E., Avrett, E.H., and Loeser, R. 1981, Structure of the solar chromosphere. III. Models of the EUV brightness components of the quiet Sun, *Astrophys. J. Suppl.*, 45, 635-725. (VAL-III).

Vernazza, J.E., and Reeves, E.M. 1978, Extreme ultraviolet composite spectra of representative solar features, *Astrophys. J. Suppl.*, 37, 485-513.

White, O.R., and Livingston, W.C. 1981, Solar luminosity variation. III. Calcium K variation from solar minimum to maximum in cycle 21, *Astrophys. J.*, 249, 798-816.

White, O.R., and Suemoto, Z. 1968, A measurement of the solar H and K line profiles, *Solar Phys.*, 3, 523-530.

Further General References

Athay, R.G. 1976, *The Solar Chromosphere and Corona: Quiet Sun* (Boston: Reidel), 504 pp.

Jordan, S.D., ed. 1981, *The Sun as a Star*, NASA SP-450, NASA Information Branch, Washington, D.C. 574 pp.

Linsky, J.L., and Avrett, E.H. 1970, The solar H and K lines, *Pub. Astron. Soc. Pacific*, 82, 169-248.

Neckel, H., and Labs, D. 1984, The solar radiation between 3300 and 12500Å, *Solar*

Phys., 90, 202-258.

Skumanich, A., Lean, J.L., White, O.R., and Livingston, W.C. 1984, The Sun as a star: Three-component analysis of chromospheric variability in the calcium line, *Astrophys. J.*, **282**, 776-783.

Stein, R.F. 1981, Stellar chromospheric and coronal heating by magnetohydrodynamic waves, *Astrophys. J.*, **246**, 966-971.

Thomás, R.N. 1983, *Stellar Atmospheric Structural Patterns*, NASA SP-471, NASA Information Branch, Washington, D.C., 369 pp.

Ulmschneider, P. 1981, Theories of heating of solar and stellar chromospheres, in *Solar Phenomena in Stars and Stellar Systems*, ed. R.M. Bonnet and A.K. Dupree (Boston: Reidel), 239-263.

Ulmschneider, P., and Stein, R.F. 1982, Heating of stellar chromospheres when magnetic fields are present, *Astron. Astrophys.*, **106**, 9-13.

White, O.R., ed. 1977, *The Solar Output and Its Variation* (Boulder: Colorado Associated Univ. Press), 526 pp.

Withbroe, G.L., and Noyes, R.W. 1977, Mass and energy flow in the solar chromosphere and corona, *Ann. Rev. Astron. Astrophys.*, 15, 363-387.

NATIONAL SOLAR OBSERVATORY
ATLAS NO. 1

SOLAR FLUX ATLAS FROM 296 TO 130

ROBERT L. KURUCZ[1]   INGEMAR FURENLID   JAMES BRAULT   LARRY TES

Smithsonian Institution
Astrophysical Observatory
Cambridge, Massachusetts

Georgia State University
Atlanta, Georgia

National Solar Observa
National Optical Astronomy Ob
Tucson, Arizona

June 1984

---

[1] This work was supported in part by NASA grant NSG-7054.

[2] Now at E.G. & G., Los Alamos, New Mexico 87544, U.S.A.

[3] Operated by the Association of Universities for Research in Astronomy, Inc. under contract wit

Printed by the Office of the University Publisher, Harvard University.
Copies available at $13.00 from the National Solar Observatory, Sunspot, New Mexico 88349, U.S

ORY

2 FOLDOUT FRAME

TO 1300 nm

T LARRY TESTERMAN[2]

Solar Observatory
l Astronomy Observatories[3]
cson, Arizona

er contract with the National Science Foundation

ico 88349, U.S.A.

SOLAR FLUX ATLAS FROM 296 TO 1300 NM

I. INTRODUCTION

This atlas presents the solar flux spectrum observed with high resolution and high signal-to-noise using the Fourier transform spectrometer (FTS) on the McMath Solar Telescope at Kitt Peak National Observatory. The FTS allowed us to greatly improve the signal-to-noise and wavelength coverage compared to the earlier high resolution atlas produced by Beckers, Bridges, and Gilliam (1976) using a grating spectrograph at Sacramento Peak. Information about the observations is summarized in Table 1. Eight scans, odd-numbered 1 to 15, were made of the integrated solar disk with overlapping bandpasses that cover the spectrum from 296 to 1300 nm. High points from these scans are plotted in Figures 1 and 2 for frequency and wavelength. At the same time scans, even-numbered 2 to 16, were made for a standard lamp. The ultraviolet scans have resolving power of approximately 348000 and the infrared scans approximately 522000. Peak signal-to-noise for each scan ranges from 2600 to 9000 as listed in Table 1. At a particular wavelength the noise can be best estimated from the spectrum itself.

II. WAVELENGTH REDUCTION

The frequency scale for each scan must be normalized by a multiplicative factor near unity that depends on the setup and alignment of the FTS. Ideally this factor would be determined by observing through a gas absorption cell for a gas with well-known lines in the bandpass. We determined this factor from the spectrum itself by using the O_2 line at 688.38335 nm and defining its air wavelength to be that given by Pierce and Breckenridge (1973). The spectra were converted from frequency to air wavelengths using Edlen's (1966) expression. As this line appears only in scans 11 and 13, it could not be used for the other scans. Scan 15 was set by aligning terrestrial lines common to scan 13. Since the other scans did not have suitable terrestrial lines, they were corrected in the solar rest frame by aligning relatively clean solar lines in overlapping scans. The solar rest frame was determined from radial velocities computed with a program that we obtained from Mark Reid of the Center for Astrophysics. It has errors on the order of 4 m/s because it does not include planetary perturbations. The radial velocities for the beginning, end, and middle of each scan are listed in Table 1. The change in radial velocity while a scan was being made resulted in about 0.2 km/s broadening of the solar lines. We used the middle value in shifting the spectra. Operationally, the frequency correction factor was also treated as a Doppler shift and specified in km/s. These values are listed in Table 1. Considering all the fitting and shifting, our final wavelengths in scan 1 may have errors as large as 0.1 km/s. If the wavelength of any one line in each scan can be determined more accurately, the whole scan can be rescaled to that accuracy.

III. REDUCTION TO RESIDUAL FLUX

To produce a residual flux spectrum we made a zero-point correction, divided out the standard lamp, fitted a pseudo-continuum to each scan, and then we combined the scans together into a continuous whole.

Non-linearities in the detector introduce systematic errors in the strong, low-frequency components of the Fourier transform that produce a varying zero-point error in the spectrum. This error can be avoided by using a narrow bandpass to reduce the signal. We corrected the spectrum by fitting linear segments to opaque terrestrial line centers that were wide enough that ringing was not a problem. Ringing is clearly visible in the expanded scale plots in Figure 7 for terrestrial lines that are not resolved. Only scans 11, 13, and 15 had terrestrial lines that allowed this correction, and for those scans the maximum corrections were 0.45%, 0.25%, and 0.90%, respectively. We estimate the residual error to be about 0.10% . Scans 1 to 9 were not corrected and we cannot rule out the possibility of 0.25% zero-point errors. In particular, the cores of the Ca II H and K lines are uncertain by this amount.

In conjunction with each solar scan, a standard lamp was scanned with the spectrometer in the same configuration. We divided the solar scans by the lamp scans to remove the effects of any small features in the bandpass limiting filters that were used with each scan.

Figure 3 illustrates our method for subjectively fitting a pseudo-continuum to each scan. For each scan the highest point out of every 100 points was plotted and a curving pseudo-continuum was subjectively fitted to the highest high points. Each scan was normalized to its pseudo-continuum so that it became residual flux with the continuum level at 1.0. Note in Figure 3 that the pseudo-continuum is obviously far from being the real continuum for scans 1 to 7.

Figure 4 illustrates the subjective fitting together of the scans into a continuous whole. We made plots of the overlapping scans and chose a high region where the scans coincided as the crossover point. The wavelengths where the cuts were made are 329.897, 378.2914, 401.965, 473.8, 576.5, 753.9, 999.7 nm. These plots also give an indication of reproducibility and noise level but these are regions near half-maxima of the bandpasses where the bandpasses have steep slopes of opposite sign. The quality of the data at the centers of the bandpasses is much higher. Ideally measurements like these should be taken with rectangular bandpasses that overlap in order to avoid these problems.

There are systematic differences between scans. First, zero-point corrections could be made only on scans that had completely opaque terrestrial lines that are supposed to produce zero signal. No zero-point correction could be made for the blue and ultraviolet scans and we cannot rule out errors as large as 0.25% . If neighboring scans have different, non-negligible errors the residual fluxes are inconsistent across the join. Second, these data are of such high quality that very weak terrestrial features can be significant. Neighboring scans were taken through different atmospheric conditions with different amounts of water vapor and ozone. For example, at 402.07, 402.14, and 999.9 nm the spectra are actually different for this reason. Finally, the merged spectrum has solar wavelengths so terrestrial lines are Doppler shifted from each other in neighboring scans by the amounts listed in Table 1.

The final residual flux spectrum is plotted twice, in Figure 5 at 40 nm per page, and in Figure 6 at 4 nm per page in the visible and at 8 nm per page in the infrared. In Figure 6 the top 10% is also plotted at an expanded scale that shows weak features.

IV. IRRADIANCE CALIBRATION

The calibration is based on the irradiance derived by Neckel and Labs (1984). Their data are listed in Table 2 and shown in Figure 7. Their bandpasses provide continuous coverage from 329 to 666 nm and sporadic points out to 1247 nm. From the atlas we computed the mean value of residual flux R for each bandpass assuming that the bandpasses were exactly rectangular. The width and R for each bandpass are listed in Table 2. The actual bandpasses were slightly rounded and have some wavelength error, but errors from these effects are inconsequential. We divided the observed irradiance by the mean R to find the irradiance pseudo-continuum level listed in Table 2.

Our value of R includes the terrestrial lines. Neckel and Labs' corrections for terrestrial line absorption in their observations are also listed in Table 2. As they chose their bandpasses in the red and infrared to have few or no terrestrial absorption lines, the corrections vary from 0 to 2% and are typically on the order of 0.1% . We plan to determine this for our scans by synthesizing both the solar and the terrestrial spectrum, but we have not yet done so. We have assumed that our terrestrial absorption is approximately the same as that of Neckel and Labs' and that ours is negligible when theirs is negligible. Figure 7 includes a plot of the pseudo-continuum values corrected for this absorption. Ideally this should be a smooth curve, but, in fact, it has structure at the several per cent level.

The dip at 600 nm is probably caused by our poor treatment of the ozone absorption there, which, by accident, falls between scans 9 and 11. The ozone feature is the Chappuis bands which run from 450 to 750 nm. The cross-section is tabulated by Vigroux (1953) and is roughly plotted in a figure in Goody (1964). The maximum absorption coefficient is 5.E-21 cm^2 which should produce about 5% absorption at 600 nm in our atlas. Our signal-to-noise is high enough that we should be able to see the structure. Vigroux also gives data between 407 and 447 nm. Apparently there are no measurements of ozone cross-sections between 350 and 400 nm and longword of 750 nm. At our signal-to-noise, ozone may be significant at all wavelengths. We would very much like to see a thorough, high-resolution laboratory study.

In the infrared we subjectively fitted an expression for the pseudo-continuum to the measured points for the range 746.5 to 1300 nm,

```
IRRADIANCE=0.80933E18/W**5/
          (EXP(1.4384E7/W/(6892.094-2.691159*W+.001669325*W**2))-1.)
```

for wavelength W in nm and irradiance in $\mu W/cm^2/nm$.

Below 330 nm we pieced together a calibration using Broadfoot (1972) whose long wavelength limit is 319.9 nm and Arvesen et al. (1969) who start at 300 nm and go up. We plotted Broadfoot, Arvesen, and Neckel including overlaps and concluded that the Arvesen wavelength scale was shifted by +0.4 nm and that their irradiance should be reduced by about 10 per cent to be in agreement with Neckel and Labs and with Broadfoot. We made Neckel-like 2.1 nm bands for Broadfoot and 2 nm bands for Arvesen et al. These are listed in Table 2 and plotted in Figure 7. We used Broadfoot for 296 to 310 nm and Arvesen et al. multiplied by 0.9 from 312 to 328 nm. We do not trust this ultraviolet calibration to better than 25 per cent, both from the observations and from the very poor pseudo-continuum fit in this region as shown in Figure 3.

To convert the atlas from pseudo-residual flux to irradiance, we computed a pseudo-continuum value, either from the fit in the infrared longward of 746.5 nm, or from linearly interpolated bandpass values, and then multiplied by the pseudo-residual flux. Table 3 lists the calibration of the pseudo-continuum level of the atlas in $\mu W/cm^2/nm$ for every 0.05 nm in the visible and every 0.10 nm in the infrared. One μW is 10 ergs/s. For flux in $ergs/cm^2/s/nm$ at the surface of the sun multiply the irradiance by 10.*(1.495985E13/6.9598E10)**2 = 462020. For astrophysical flux F divide the flux by π. For flux moment H divide the flux by 4π.

V. MAGNETIC TAPE LISTING

A magnetic tape listing of the atlas may be obtained by sending a 2400 foot tape to Dr. Robert Kurucz, Center for Astrophysics, 60 Garden Street, Cambridge, Massachusetts 02138. The tape will be written 9 track, 1600 bpi blocked ASCII with 80 characters per record and 50 records per block. The first file will contain wavelength, residual flux pairs. The second file will be a program that can read the tape and convert it to irradiance if desired. The third file will be the residual flux interpolated to uniform point spacing in wavelength.

VI. REFERENCES

Arvesen, J.C., Griffin, R.N., and Pearson, B.D. Appl. Opt., 8,2215-2232,1969.

Beckers, J.M., Bridges, C.A., and Gilliam, L.B. 'A high resolution spectral atlas of the solar irradiance from 380 to 700 nm', AFGL-TR-76-0126, 340pp., 1976.

Broadfoot, A.L., Ap.J., 173, 681-689, 1972.

Edlen, B. Metrologia 2, 71-80, 1966.

Goody, R.M. Atmospheric Radiation, Oxford Univ. Press, London, 436pp, 1964.

Neckel, H. and Labs, D. Solar Physics, 90, 205-258, 1984.

Pierce, A.K. and Breckenridge, J.B., 'The Kitt Peak Table of Solar Spectrum Wavelengths', Contribution No. 559, 1973.

Vigroux, E. Annales de Physique, 8, 709-762, 1953.

Table 1. Record of the Observations

296. – 329.897 – 378.2914 – 401.965 – 473.8 – 576.5 – 753.9 – 99

scan 1	scan 3	scan 5	scan 7	scan 9	scan 11	scan 13
29113.63238	25147.01194	24649.74115	17171.55918	12485.51810	8624.80162	7103.72630
.03645036	.03528395	.02979210	.05516111	.02381424	.01815228	.01421564
695994	696954	696362	680994	1042714	1045794	1045974
348000	348480	348184	340500	521360	522900	522990
5000	9000	3000	3000	3000	3000	2600
06/22/81	06/21/81	06/22/81	11/23/80	03/24/81	03/25/81	03/25/81
42205.78 49637.39	43752.23 54066.75	34183.89 41652.48	38243.02 44168.07	45035.48 52805.08	38297.73 45284.97	47186.79 54248.59
.01039	.01439	.01039	.00798	.00719	.00639	.00639
26	36	26	20	18	16	16
UV Si diodes Cor2985+ CuSO4(10)	UV Si diodes CuSO4+ CS7-54	UV Si diodes CS7-51+CS4-97 WG345	silver Si diodes CS7-59+CS4-97+ GG375	silver Si diodes GG435+ CS4-96	silver Si diodes VP700(15)+ OG570	silver Si diodes RGN9
−2365.44 4737.39	−806.28 9179.02	−10386.13 −2918.65	−5406.42 189.79	208.00 7651.57	−6512.91 148.14	2050.36 9113.65
.409003	.409102	.409018	−.324822	.028530	.034821	.035529
.228211 .338631	.165580 .606078	.700693 .256191	.998589 .915586	.529622 .744536	.702180 .522780	.541084 .812982
1.02 1.05	1.01 1.21	1.30 1.03	1.84 1.63	1.15 1.35	1.30 1.15	1.16 1.45
601.3	601.5	601.3	599.7	601.3	602.2	602.2
0.029 0.222 0.125	0.076 0.330 0.203	−0.154 0.015 −0.070	−0.476 −0.320 −0.398	0.492 0.704 0.598	0.309 0.502 0.406	0.557 0.741 0.649
−0.75	−0.75	−0.75	0.25	0.15	0.30	0.30

of the Observations

	scan 11	scan 13	scan 15	
576.5	- 753.9	- 999.7	- 1300.	adopted wavelength limits (nm air)
10	8624.80162	7103.72630	5247.91886	wavenumber of first point
4	.01815228	.01421564	.01154261	dispersion (cm-1)
	1045794	1045974	1044994	number of points in scan
	522900	522990	522500	spectral resolving power
	3000	2600	3000	max signal-to-noise
1	03/25/81	03/25/81	05/11/81	date
3	38297.73	47186.79	37338.11	starting time (seconds)
3	45284.97	54248.59	45506.13	stopping time (seconds)
	.00639	.00639	.00719	time/point (seconds)
	16	16	18	number of scans
	silver	silver	silver	beamsplitter
s	Si diodes	Si diodes	InSb	detector
	VP700(15)+ OG570	RGN9	GaAs+ CS5-57	optical filters
	-6512.91	2050.36	-6895.55	hour angle at start (seconds)
	148.14	9113.65	944.94	hour angle at end (seconds)
	.034821	.035529	.314112	mean declination (rad)
	.702180	.541084	.532358	zenith distance at start (rad)
	.522780	.812982	.251236	zenith distance at end (rad)
	1.30	1.16	1.16	airmass at start
	1.15	1.45	1.03	airmass at end
	602.2	602.2	599.4	atmospheric pressure (torr)
	0.309	0.557	0.184	radial velocity at start (km/s)
	0.502	0.741	0.397	radial velocity at end (km/s)
	0.406	0.649	0.291	radial velocity mean (km/s)
	0.30	0.30	0.00	frequency correction (km/s)

2 FOLDOUT FRAME